Probing Nanomaterial Properties in a High-resolution Transmission Electron Microscope

Zhang Chao

February 2017

Probing Nanomaterial Properties in a High-resolution Transmission Electron Microscope

Zhang Chao
Doctoral Program in Materials Science and Engineering

Submitted to the Graduate School of
Pure and Applied Sciences
in Partial Fulfillment of the Requirements
for the Degree of Doctor of Philosophy in
Engineering

at the
University of Tsukuba

This Dissertation is dedicated to my wife, Qi.

We got married on July.20, 2016.

Abstract

Probing Nanomaterial Properties in a High-resolution Transmission Electron Microscope

Fast development of Transmission Electron Microscopy (TEM) is pushing boundaries for nanomaterial observations at the unprecedented high spatial resolution, down to 60 pm, these days. The advances of sampling techniques, lens aberration corrections and spectroscopic analysis allow for entire understanding of various materials atomic structures and spatially-resolved chemical compositions. However, common TEM techniques have had no access to nanomaterial electrical, mechanical, optical and thermal properties, which may be advantageous for future applications, such as flexible electronics, optoelectronics, green energy storage etc. Thus it is crucial to find a way to manipulate, contact, and *in situ* probe a nanomaterial in order to reveal its peculiar functionality. For example, in order to understand light-matter interactions, electrical and optoelectronic properties of semiconducting nanomaterials and their heterostructures, it is essential to perform challenging optoelectronic tests under various manipulations inside a high-resolution TEM. The beauty and power of the state-of-the-art *in situ* TEM experiments stem from a fact that any functional property may be measured under a full control of the nanomaterial atomic structure, its defects and chemistry. This allows for the unambiguous establishment of the clear structure-property relationship. And this is the "Holy Grail" of the whole Materials Science field. However, this task is never as simple as handling and assembling toy bricks, especially

inside a TEM. Throughout my PhD term I was able to successfully perform diverse *in situ* TEM probing experiments on a rich bunch of nanomaterials which will be used in the future lithium/sodium ion batteries, flexible electronic and optoelectronic devices, and, overall, for any desired *nanoarchitectonics* concept.

This Thesis comprises of 7 Chapters. Chapter 1 is an outline of the background of the probing inside TEM, which presents the development of *in situ* TEM techniques. The content shows a novelty of *in situ* TEM, its advantages and a scope of nanomaterials which are under study. In Chapter 2, methods and engineering details of my research are presented, including *in situ* TEM setups and its applications. Chapter 3 is the first experimental Chapter introducing manipulation possibilities in the frame of the general *nanoarchitechtonics* concept and its applications for nanoengineering. The experiments have been performed on the *in situ* TEM constructed axial nanowire junctions of CdS and p-Si. Then, detailed electrical probing for energy storage research is discussed in Chapter 4. We fabricated an ultrastable sodium ion battery and analyzed the mechanism of its cycling performance under *in situ* TEM probing. Through coupling with *in situ* TEM applied forces, two examples of force-driven optoelectronic phenomena are detailed in Chapters 5 and 6. Finally, in Chapter 7, the whole research carried out through the Thesis is reviewed and general conclusions are drawn. Also in this final Chapter, suggestions are made for the future work in this booming field.

Acknowledgments

I would like to express my special appreciation to my adviser Prof. Dmitri Golberg. I thank him for encouraging my studies and for guiding me to grow as a junior researcher. His advices on research have been priceless. Prof. Golberg is always warm and encouraging. He never criticized nor complained on me, he never forced me to do anything; instead, he provided me freedom, trust and appreciations. I am very much rised by him to accomplish all research projects.

I would like to thank the Committee, Prof. Takayoshi Sasaki, Prof. Masahiro Sasaki, Prof. Naoki Fukata for precious wise advices. They were very kind to me but keen and strict with respect to science.

I am grateful to the collaborations with Prof. Naoki Fukata, Prof. Xi Wang and Prof. Wei Tian. They provided excellent samples, comprehensive performance tests and professional advices. Especially the credits go to Dr. Zhi Xu and Dr. Ovidiu Cretu for their instructions for microscopy and engineering, as well as writing, data processing and programming. They are incredibly smart, insightful persons with charming personalities. I would like to thank my *senppai* Dr. Qunhong Weng, not only for his experimental assistance and chemistry-related advices, but also for his scientific-wise characteristics: wisdom, diligence and integrity.

I thank many other colleagues and research friends in NIMS and other Institutes for every advice and assistance, namely (in family name order) Prof. Y. Bando, Prof. P. Dai, Dr. K. Hasegawa, Ms. Y. Hirai, Mr. K. Iiyama, Dr. X. Jiang, Ms. S. Kasaya, Dr. N. Kawamoto, Prof. D. Liu, Prof. X. Liu, Dr. M. Mitome, Dr. K. Moore, Mr. M. Nakatsu, Dr. A. Nukui, Dr. A. Ohi, Mr. H. Sugaya, Prof. D-M. Tang, Prof. J.

Tang, Dr. Y. Xue, Dr. I. Yamada, Prof. X. Wang, Dr. M. Yamaguchi, Prof. T. Zhai, Prof. C. Zhi, Dr. M. Zhou, Mr. X. Zhou. Thank you all.

My research was conducted at the National Institute for Materials Science (NIMS), Tsukuba. I would like to acknowledge the financial support from NIMS.

I am grateful to University of Tsukuba, Tsukuba City and Japan, where I live and study for more than 4 years.

Last but not least, I would like to thank my family for their deep and endless love. I love you.

Feb 2017

C. Zhang

Tsukuba, Japan

Contents

List of figures

List of Tables

1 Introduction

The advancement of materials science and technology has led to the discovery and utilization of nanoscale materials. Many of these new materials possess extraordinary chemical, electrical, optical or mechanical properties. However, as human beings, who are millions or billions times larger than nanomaterials, we are not perfectly scaled to reach them directly. As Feynman said, *there is plenty of room at the bottom*, but it also means that plenty of efforts are expected toward researching.

1.1 Probing of nanomaterials

Generally, nanomaterials are materials in which a single unit is sized from one nanometer to a few hundred nanometers. The scale difference between these materials and human body is more than a million. Besides scale difference, nanostructures usually possess special properties, as compared with bulk materials, due to chemical composition difference, surface to volume ratio and quantum confinements. The confined structures of the same chemical type and composition might present very different properties. An easy way to understand a value of the nanomaterial is to consider carbon materials. We know that diamond and graphite are allotropes of carbon which possess different bonding and thereby amazingly distinct physical and chemical characteristics. This is also true for a fullerene, a carbon nanotube and graphene. Even the number of walls in a carbon nanotube would significantly affect its properties. [76]

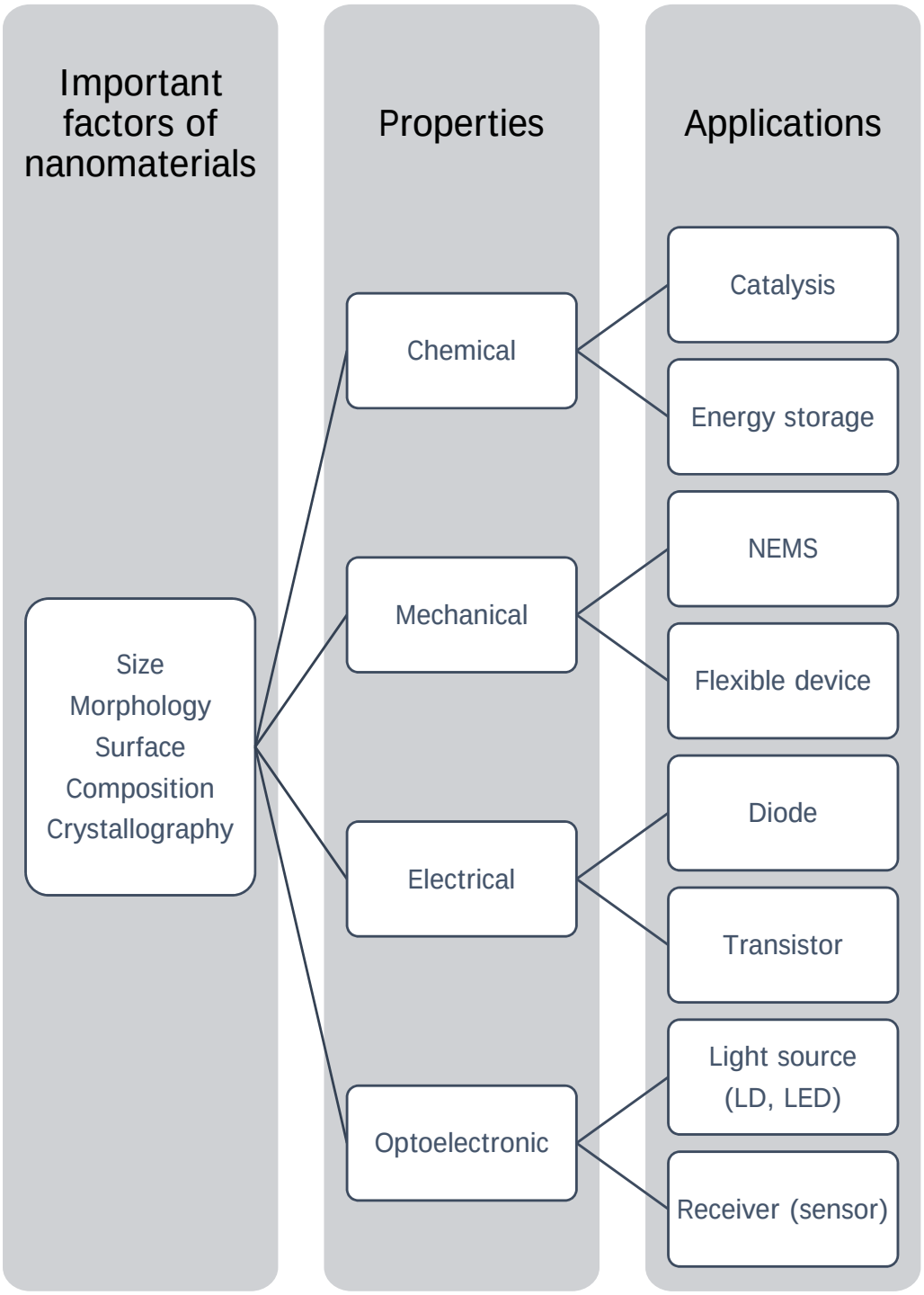

Figure 1.1: Special factors of nanomaterials contributing to various applications.

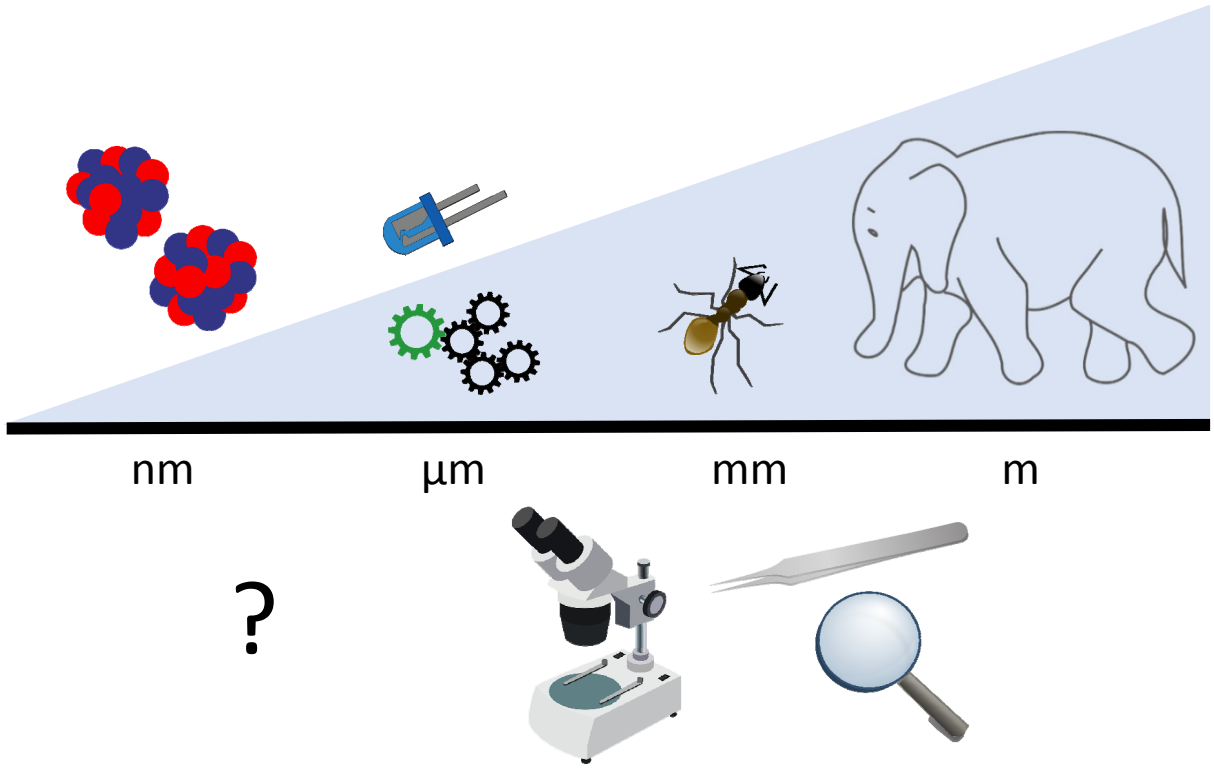

Figure 1.2: How human beings gain access to lower scales, how to see and to manipulate.*

Therefore, what makes nanostuctures distinctive is not only their size, but also their unique compositions, surfaces and quantum confinement effects.

As shown in Figure 1.1, many effects contribute to the particular functionality of a nanomaterial, such as superior mechanical strength and rigidity, ultrahigh electrical mobility, abundant chemical active sites, *ect.* Mechanical superiority is important for applications, *e.g.* for flexible electronics and devices in Nano Electro-Mechanical Systems (NEMS). Electrical superiority of nanomaterials with various electronic band structures could be applied in electrical diodes, transistors, laser diodes (LDs), light-emitting diodes (LEDs), and in transparent or flexible electronics and optoelectronics. Chemical superiority of nanomaterials make them desirable for highly efficient catalysis and portable energy storage devices with high energy density.

However, it is not straightforward to access the properties of these nanomaterials and prepare them for real applications. Unfortunately, this is due to the above-mentioned issue - a small scale. We understand that the observation, reach and built of an object which is 10^6 to 10^9 (in one dimension) smaller then any real world macro-object, for example the *Great Wall of China* ($21,196km$), is challenging. Similarly, as compared with human beings' hands, of a size is about 20 cm, nanoscaled objects are usually million times smaller. Hence, even though the nanoscale building blocks are superior in many respects

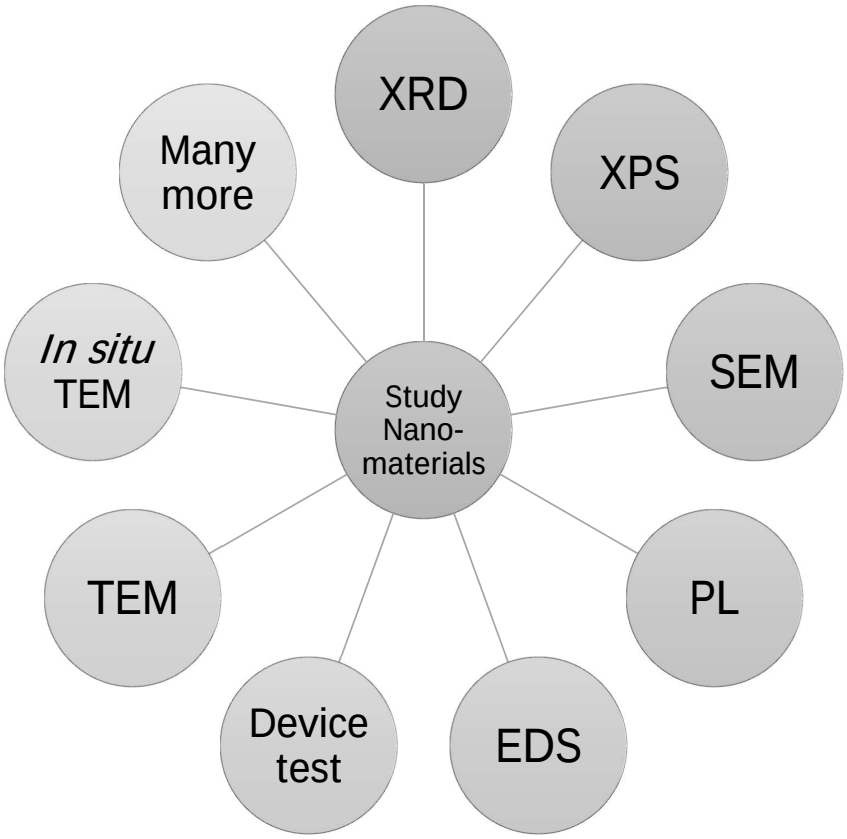

Figure 1.3: *In situ* TEM serves as a way to study nanomaterials.

in theory, we are not able to utilize them easily. As shown in Figure 1.2 *, we are able to reach smaller scales using tweezers and optical microscopes, but it is very challenging to reach nanoscale objects.

The way human beings make use of fire, tools, light and electrons is perhaps what sets our modern live standards above of other species. By understanding and utilizing photons, electrons and atomic forces, microscopy allows us to view sub-millimeter objects that cannot be observed with a naked eye. Thanks to the advancement of tools - microscopy and piezoelectric materials - we can now access to nanomaterials by high precision probing technique under direct high-resolution observations. By applying electrical field to a piece of piezoelectric material, the latter precisely changes its shape in function of the applied electric field. Therefore, we may control the mechanical movements by electrical biases and confirm the location of an object and the probe using microscopy.

*Without specification, all clip art materials (elephant, ant, microscope, tweezers, etc.) in figures of the Dissertation are adapted from Internet which are *free to use without permission*.

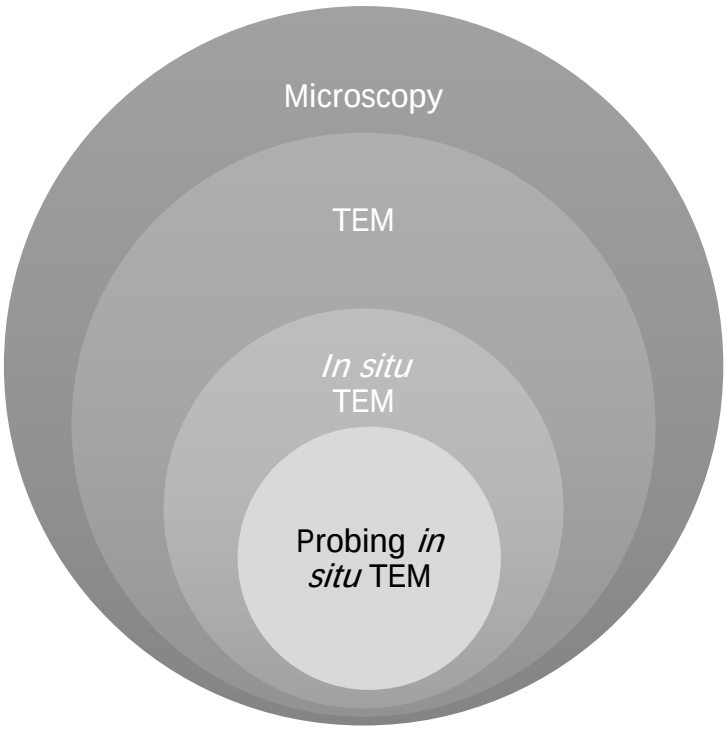

Figure 1.4: Relationships between *in situ* probing TEM and other microscopies.

1.2 Seeing is believing: Transmission Electron Microscopy

In the past century, development of particle physics made a way for new microscopies, such as Scanning Probe Microscopy (SPM, including Atomic Force Microscopy and Scanning Tunneling Microscopy), Scanning Electron Microscopy (SEM), and Transmission Electron Microscopy (TEM). Among all microscopies, TEM, has the best ultimate spatial resolution; this allows one to reach atomic resolution and to simultaneously get full crystallography information. TEM provides deep and direct information from a thin sample through the transmission and diffraction of electrons.

When researchers are not satisfied with only seeing of a material in statics, dynamics may be introduced to the sample. *In situ* TEM is the newest advanced technique which gives access to the sample dynamics *via* observation, manipulation and various tests.

Particularly, by adapting the microscope or using a special specimen holder, it is possible to make deliberate attempts to modify materials during high-resolution characterizations. It allows for the observation of dynamic properties within a material under special circumstances.[3]

For instance, a heating holder would provide the desired high temperature to trace (by a fast CCD video camera) and, thereby, reveal chemical transformations within a sample. By contrast, without *in situ* heating, one is only able to see the initial and final states of the reaction; in this way the regarded mechanism is usually inferred based on a few indirect clues, such as X-ray Diffraction (XRD), X-ray

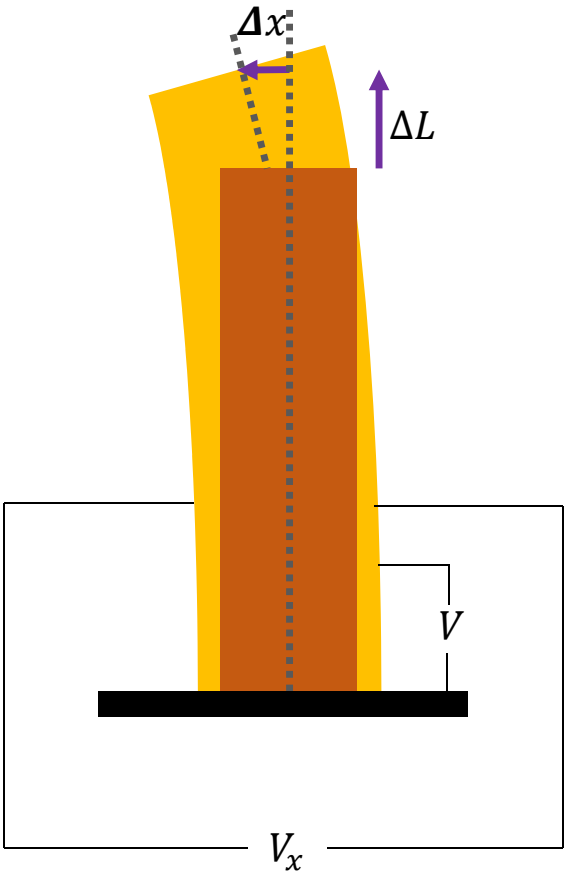

Figure 1.5: Schematic illustration of how piezoelectric works for precise nanomanipulations.

photoelectron spectroscopy (XPS), Energy Dispersive X-ray Spectrometry (EDS), Photoluminescence (PL) and indirect TEM characterizations before and after the dynamic tests. As illustrated in Figure 1.3, *in situ* TEM is very important and irreplaceable approach to study nanomaterials.

Various specimen holders make it possible to introduce heating, cooling, electrical bias, mechanical force, gas, liquid, magnetic field, light etc. to the sample under various conditions. As illustrated in Figure 1.4, probing *in situ* TEM is one small domain of microscopy as a whole. And this dissertation is mainly focused on probing of nanomaterials *via in situ* TEM.

1.3 Untouchable scale: Probing techniques for nanomaterials

The experiments performed by *in situ* probing microscopy are carried out based on piezoelectric effect and microscopy.

Piezoelectricity is a phenomenon where electricity is directly related to the pressure applied to the material. In a piezoelectric actuator, special driving signals are applied to a piezoelectric tube in certain directions, and, thereby, the piezoelectric tube would respond while changing shape accordingly.[65,

90] As shown in Figure 1.5, when the base of the tube is fixed, transverse and axial movements of the tube tip would be expressed approximately by the following equations:

$$\begin{bmatrix} \Delta x \\ \Delta y \end{bmatrix} = \frac{2\sqrt{2}d_{31}}{\pi D h} L^2 \begin{bmatrix} U_{+x} - U_{-x} \\ U_{+y} - U_{-y} \end{bmatrix},$$

$$\Delta L = \frac{d_{31} L}{h} V$$

, where Δx, Δy and ΔL are deflections in x, y and axial directions, $U_{+x} - U_{-x}$, $U_{+y} - U_{-y}$ are driving voltages applied to the opposite sides of the tube (therefore in total four electrodes exist, in addition to the base ground electrode).V is a voltage applied to all four quadrants. L, D and h is the length, diameter and thickness of the tube. The transverse piezoelectric coefficient d_{31} is very small (about -10^{-10}m/V), and, hence, the movement can be controlled precisely by biasing.

With a help of a piezoelectric actuator, we can handle an ultrasharp probe to touch the nanoscale sample with the nanometer precision.

Now we have two effective ways to see and touch a nanostructure – *in situ* TEM and piezo-motor-driven probing.

1.4 Optoelectronic and flexible electronic applications of nanomaterials

We are currently fully enjoying the benefits of well developed microelectronics and nanoelectronics. However, people are trying to improve the speed of information transmission by means of light. As compared with electrons in the metalic conductors (copper or even gold), photons in the optical system possess much higher capacity of information. The Society benefits a lot from the optical fiber information technology. For instance, it was quite difficult and expensive to perform high-definition video streaming *via* Internet 20 years ago, when we were using copper wires to transmit electrical information. The silicon-based electronics is efficient and is mainly based on the two materials: silicon and copper (or other conductors, such as gold). The manufacturing is sophisticated and requires etching silicon chips and applying a mask for electrode coating. Silicon is absolutely perfect semiconducting material. By doping techniques and smart designs, billions of transistors could work at a high speed within a nail-sized chip. The problem is (for optoelectronic applications) that the band-gap diversity is required. Therefore silicon, as a perfect semiconductor for electronics, could not realize fully functioning optoelectronics.

Besides, flexible electronics attracts a great deal of attention. In the last few years, we experienced an explosion of flexible optoelectronic applications in flat-panel displays, lighting, sensing, and energy cells. For instance, organic light-emitting diodes (OLED) and flexible lithium-ion batteries are developed as

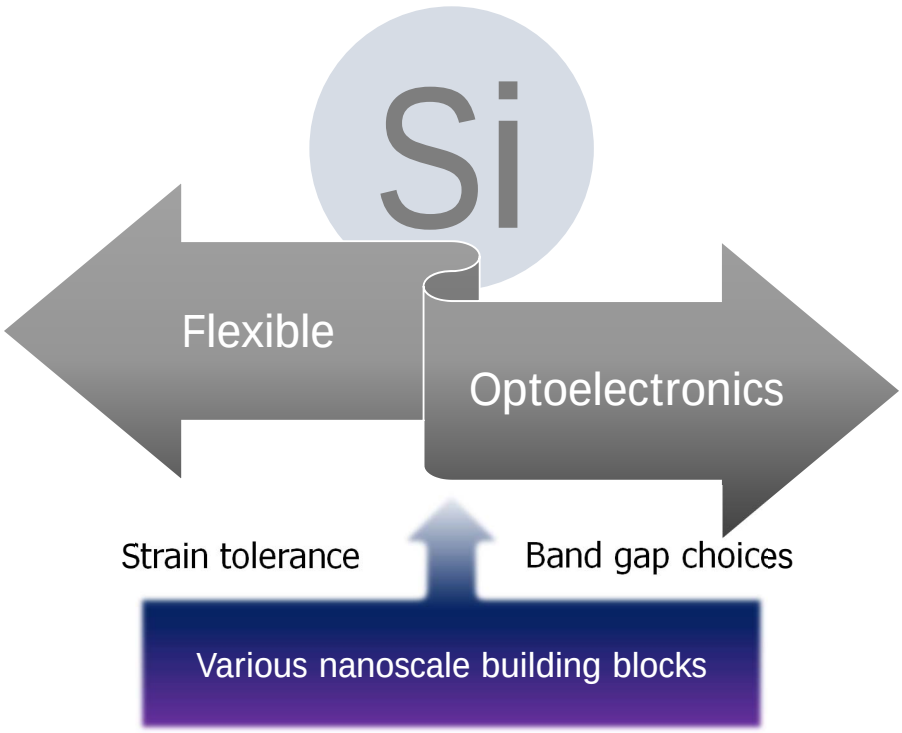

Figure 1.6: Silicon's two short-comings for flexible devices and optoelectronics could be backed-up by bottom-up approach using nanomaterials in future integrations.

the next-generation technology for wearable electronics, bendable smart-phones, foldable displays, *etc.* However, to make silicon wafers flexible is never an easy task. Therefore, people believe that the bottom-up technology would be able to architect nanoscale building blocks on a flexible substrate for future flexible electronics and optoelectroncs.

Therefore, for optoelectronic and flexible electronic applications, the usage of conventional silicon industries is challenging, as shown in Figure 1.6. Silicon is an ideal material to meet all requirements within a field effect transistor. The silicon based devices rely on controlling carriers realized *via* structural design and doping. In recent years, silicon-based optoelectronics is growing steadily but not exponentially, as expected by Moore's Law. [91] The semiconductor industries produce devices mainly by the top-down strategy. A top-down approach is a smart way to apply desired patterns to the device engineering, which came in effect since 1970s, when human beings were not so experienced to manipulate nanostructures. However, these days a bottom-up approach is emerging and shows a high promise in constructing systems by piecing building blocks together. It is true that some nanomaterials show superior properties for electronics, but it appears that during the last decade, many efforts from various research groups have been unable to establish the bottom-up technology as a real market value.

It is expected that in the future high quality nanomaterial building blocks could be well handled for device integrated *via* the automated mass production. The integrated LDs, LEDs and photodetectors

could be manufactured using nanowires, nanosheets, and even quantum dots, to realize fully functioning optoelectronic chips. The current obstacle is to get more knowledge on the building block materials. How does the electrical signal from nanowires or nanosheets behaves under strain and light illumination, what is the photocurrent spectroscopy of the material - such questions are not well studied. Consequently, it is strongly desired that we find the answers to these questions in order to provide clues for future flexible electronics and optoelectronics.

1.5 Energy storage applications of nanomaterials

Electrical energy storage will be far more important nowadays than it was when we had abundant petroleum resources. From powering portable electrical devices (cell phones, tablets, laptops), implantable medical applications (pacemaker), to machines (hybrid electric vehicles), the humans' desire for clean, safe, fast and efficient energy storage is becoming more and more significant.

Among all energy storage applications, lithium ion-batteries (LIBs) are the most needed devices due to their high energy density, which is the key factor for portable electronics and automobiles. In LIBs, lithium ions move from the anode to cathode during discharge, and back during charging. The materials for the anodes and cathodes can dramatically affect the few key aspects of the battery's performance, including its stability and capacity. High capacity materials are eagerly demanded in order to address the needs for better energy density, cycle life and charge lifespan, among other issues faced by Li-ion batteries. However, conventional materials, although being well developed, still cannot catch up with the growing demands of battery capacity. Li-ion batteries have struggled with numerous issues, such as poor cycle life, rising internal resistance with cycling and aging, safety concerns (especially when overheated), charging speed, and limited capacity.

A lot of researches have confirmed that nanomaterials are particularly promising to solve these problems. The advantages are as follows[7, 17]:

a The reduced size significantly increases the rate of energy transformation between electrical and chemical energy (such as lithiation and delithiation process) due to the short diffusion lengths;

b Many nanomaterials enable electrode reactions to become reversible while they are not reversible for bulk materials;

c High surface to volume ratio provides large contact area between electrodes and electrolyte;

d Electron conductivity can also be improved in nanomaterials;

e Chemical potentials of ions and electrons can be different at the nanometer scale, and, therefore, electrode potential can be modified.

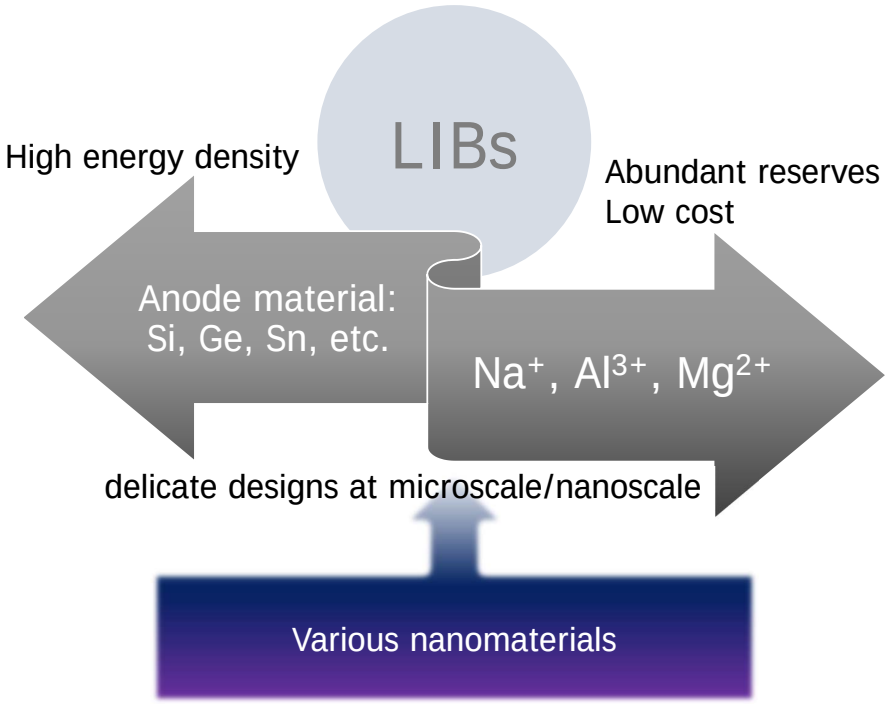

Figure 1.7: A scheme showing that secondary batteries are mostly based on Lithium and graphite. However, to gain a higher energy density while using cheaper/abundant elements, nanomaterials might be the key.

Graphite has widely been used as an anode of choice for commercial products, since the first generation of Li-ion chemistry studies appears. Due to strong needs of high capacity, in recent years, researchers have been interested in developing silicon anode materials for high capacity lithium-ion batteries. Among all investigated anode materials, silicon has one of the best theoretical capacities of 3590 mAh/g (about 10 times higher than carbon) based on the fully alloyed form of $Li_{15}Si_4$ at room temperature (at high temperature $Li_{15}Si_4$ can be obtained, giving a capacity of 4200 mAh/g, placing it on top of all other anode materials. In addition, Si anodes show moderate working potential at 0.5 V, which is higher than for graphite anodes at 0.05 V. This means that silicon is suitable to solve the safety problem of lithium deposition upon cell overcharge, as well as avert the energy penalty of battery cells assembled with the $Li_4Ti_5O_{12}$ anodes.

However, the insertion/extraction of lithium ions result in significant volume change - about 370% - which leads to structural pulverization and electrical disconnection between anode materials and current collector, and finally the battery loses most of its functions. Some recent designs of LIBs using silicon materials as anodes allow the battery to maintain its initial anode structure and, hence, to reach high capacity and, at the same time, good stability.

Cui et al. a designed high performance anode structure using Si nanowires, which were able to accommodate large strains caused by lithium ion insertion and extraction.[13] Deng et al. reported a tubular configuration made from rolled-up C/Si/C layered nanomembranes which had performed with

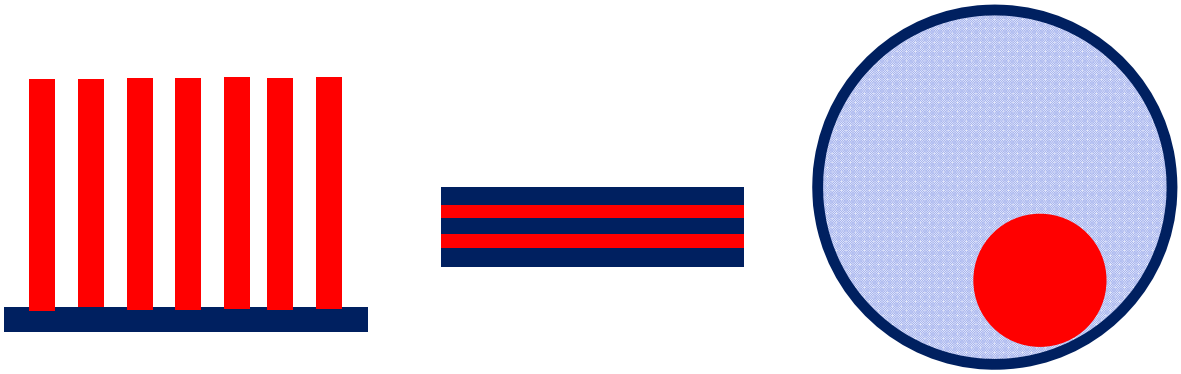

Figure 1.8: Designs for large volume expansion anode materials in batteries. Red color corresponds to the material with large volume expansion/shrinking during cycling, while material in blue color is the confinement material with low volume expansion rate and high mechanical strength.

a highly reversible capacity at approximately 2000 mAh /g (50 mA/g), and has approximately 100% capacity retention (500 mA/g) after 300 cycles.[15] Cui et al. also designed core-shell structures for Si-based LIBs. They proposed a hierarchically structured Si anode which was inspired by the structure of a pomegranate. Si nanoparticles became encapsulated by conductive carbon coatings. This leaves just enough space for the expansion and contraction during lithiation and delithiation cycles. [50]

Therefore, by designing the microscopic structures, one is able to utilize a high capacity material under structural and mechanical restrictions, as illustrated in Figure 1.8. Also, many other attempts of combining silicon with carbon materials, polymers, metals, were summarized by Liang et al.[46]

It is predicted that lithium would be the next energy resource which substitutes for petroleum, which will die out. According to the distribution of lithium on Earth[30], Chile could be the next Saudi Arabia it terms of richness of resources. This problem is more severe for many countries with very limited lithium reserves, such as Japan.

In order to explore the next generation of secondary batteries, which are called post-lithium ion secondary batteries, many investigations show that the most promising candidate is the sodium-ion battery (SIB). SIBs use sodium instead of lithium as the charge carrier, and use iron, manganese and other transition metals to replace cobalt for redox reactions. SIBs are expected to be mass produced in the nearest future due to their minor environmental impacts and a relatively low cost.

As shown in Table 1.1, although sodium possesses a higher normal electrode potential of 0.3 V, larger effective radius than lithium (in volume ratio 2.05), and smaller theoretical capacity, its cost and environmental benefits are still very attractive for applications which do not require very high capacity. Actually, it is hard for graphite, which is commercially used as an anode material for LIBs, to store and release sodium ions both theoretically and in practice because the sodium ion size is large.

However, it was discovered in 2000 that hard carbon having disordered structures could electrochem-

	LIB	SIB
Theoretical capacity	3,829 mAh/g	1,165 mAh/g
Cost (carbonate)	5,000 USD/t	150 USD/t
Reserves	23,000 ppm	20 ppm
Potential	−3.045 V	−2.714 V
Ionic radii	79.3 pm	100.9 pm

Table 1.1: Comparison of LIB with SIB.

ically store and release sodium ions.[84] Several years ago, a work was done on developing and making practical sodium ion batteries, and since recently researchers have been investigating on many anode active materials for sodium ions. It is worth noting that well-established guidelines and experiences acquired for LIBs electrode active materials are not applicable for SIBs.[2, 39, 40]

Consequently, the two currently important research areas for secondary batteries are: finding better anode active materials with higher capacities, and looking for other elements for ion batteries, as illustrated in Figure 1.7. To apply these elements in secondary batteries, nanomaterials, or nanoscaled designs play very important roles. They enable reactions which may overcome huge volume expansion and decrease diffusion lengths; while bulk materials are not capable to reach the highest capacity either for LIBs or for other special ion-batteries at the moment.

1.6 Motivation of my PhD research

As stated above, *in situ* studies on nanomaterials toward optoelectronics, electronics and ion batteries are required by the Society. My motivation is to take the challenge and to analyze the dynamics of the building blocks, as well as heterostructures, and to provide decent knowledge for advanced applications. Therefore, I explored some experimental methods and engineering details, including *in situ* TEM setups and the working mechanisms.

Then, I present manipulation possibilities in the frame of the general *nanoarchitectonics* concept and its applications for nanoengineering. The experiments have been performed on the *in situ* TEM-constructed axial nanowire junctions of CdS and p-Si. In addition, detailed electrical probing for energy storage research is discussed. I fabricated an ultra-stable sodium ion battery and analyzed the mechanism of its cycling performance under *in situ* TEM probing. Through coupling with *in situ* TEM applied mechanical forces, two examples of force-driven optoelectronic phenomena are detailed taking the examples of ZnO and CdS.

2

Engineering of Probing Techniques inside TEM

We are not satisfied with the limited possibilities provided by TEM, and we are eager to introduce more variables to the system because that is how we see dynamics in the real applications. In the following subsections, I will firstly introduce how we cooperate chemicals, light, mechanical manipulations and electrical interactions within a microscopic experiment. Especially, for the new optical fiber compatible TEM, where all the four factors could be merged, the inside and outside parts of the *in situ* microscopic setup are described in detail. Finally I will take a look at what the system can do and its short-comings.

2.1 Introducing chemicals, electricity, strain into the microsocpe

As I discussed in Chapter 1, *in situ* microscopy does introduce parameters such as heat, cooling, gas, liquid, etc. to the system, but now I focus on how we delicately introduce these variables into the microscope. In most cases, *in situ* microscopic experiments are performed by means of specially designed TEM holders, such as, heating holder equipped with the heating electrical wire or MEMS microheater. At the same time, some researchers made adaptions to the microscope, to introduce other variables. In my Ph.D. research, in addition to the electron beam, four more variables are introduced: chemicals (solid), mechanical probing, electrical contacting and optical access.

For electrical biasing, many TEM specimen holders are commercially available. Such holders provide a combination of TEM and Scanning Tunneling Microscopy(STM) techniques, which are employed simultaneously within one instrument. TEM characterization, STM imaging, introducing chemicals and electrical measurements- all become possible. A STM probe scanner has a very wide range of motions, from picometers to millimeters, which are employed either for a coarse adjustment of the sample orientation, or for the precise probe positioning.

Electrical contacts with nanoscaled interfaces can be realized under precise positioning of the movable probe to the desired spot, enabling simultaneous investigation of the specimens' structural and electronic properties under the optional strain or chemical transitions.

If the electrical biasing is realized through piezo probing, we can also utilize the probe for introducing chemicals (solid on probe) and a mechanical strain (without force value measurement*).

I briefly discussed the ways to input chemical, electrical biasing and mechanical factors in TEM. However, introducing the other variable - light - to the system is most challenging. Therefore, I will discuss this part separately, which would be a very good reference for future research, in the next section.

2.2 Introducing light into the microscope

2.2.1 Previously

Introducing the other factor - light - to the system, while at the same time maintaining the impact from other factors, is very tricky. Some researchers and companies tried to introduce light without probing. This means that no introduction of chemical changes, electricity and mechanics was achieved. We may first investigate how they introduce/collect light to/from the microscope. Table 2.1 compares the two possible ways to implement light into the system.

by adaption to the microscope	by using special holder
light plane different from specimen	on same plane with specimen
require take off detector/aperture	a specially designed holder
optics can be realized by lens on bench	only optical fiber†
complicated, high power, high cost	no adaption to TEM

Table 2.1: Two main ways to shine light into a TEM.

As shown in the Table, by replacing an aperture or making a window for optical path the light path becomes tilted. The light goes through the microscope body at the different level from the specimen

*Introducing atomic force microscopy into TEM holder for mechanical measurements is another important *in situ* method without electrical biasing functions.

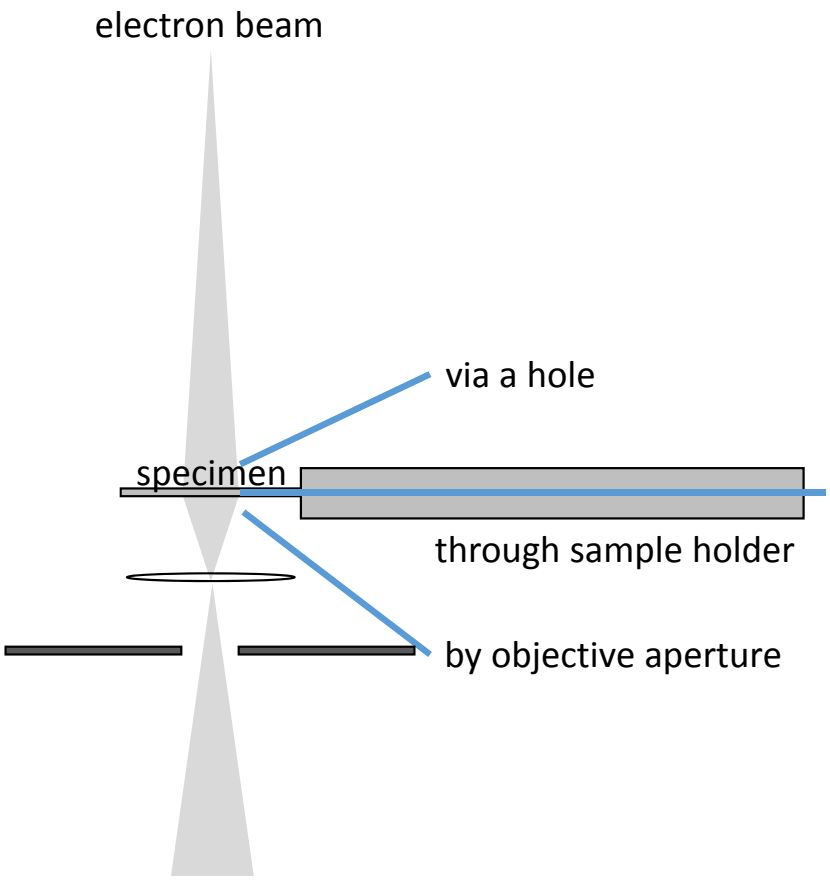

Figure 2.1: How light is compatible to TEM.

plane. In some cases, it is possible to replace a detector or an aperture by desired modules to provide more variables. As shown in Figure 2.1 under a certain angle, the light can reach the specimen. The system could be very complicated if the optics is realized through the lens system on optical bench including light sources, lens system and options such as CCD camera, chopper and monochromator. The system can be very powerful if the optical system on table is well designed and precisely assembled. However, the pressure of time and high cost are expected to be very significant.

For a special optical holder, one way is to protrude an optical fiber through the holder, as shown in Figure 2.1, the light will be shinning on the specimen at about 90 degrees to the direction of the electron beam. In most cases, the microscope is owned by many users for various applications, and, therefore, the approach of using special optical holder is more practical - it's quite unpractical to drill a hole in the microscope column and to install an optical bench on the microscope (given the fact that not every user will be happy with such operations).

A few groups have tried to deliver light into TEM.

Muto et al. (Kyushu University) managed to install an optical fiber through a 2 mm hole at an angle of 45 degrees.[24, 87] They manufactured the prototype of TEM-CL system with the light collecting

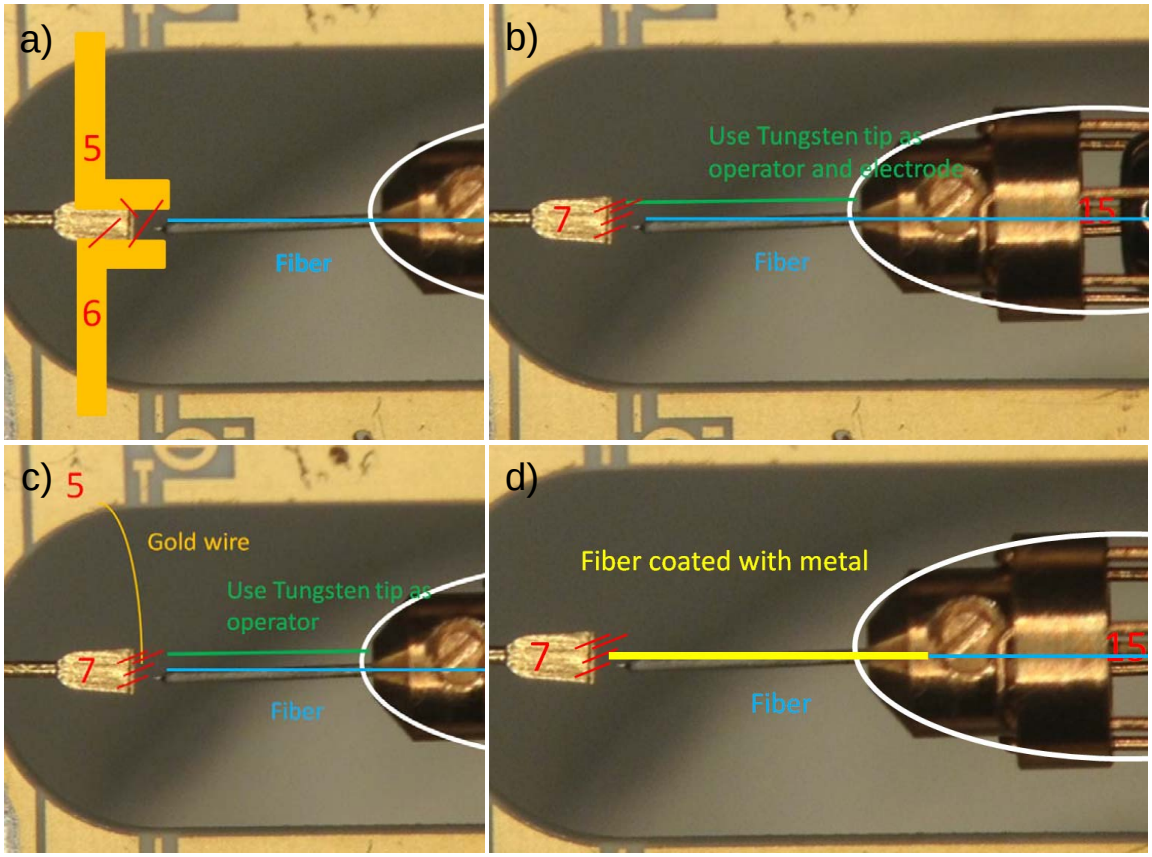

Figure 2.2: Four schemes I proposed for introducing probing functions into the optical holder.

parts integrated on the holder, but no parabolic reflector was needed within the pole piece. The system is able to take cathodoluminescence(CL), X-ray emission spectroscopy and Electron Energy Loss Spectroscopy (EELS) at the same time, even under large angle sample tilts. The main disadvantage of the holder was a significant background level from the thermal glow of the electron gun and the CL signal from the optical fiber. Later, the same group and the staff from *Nanofactory Instruments* developed a prototype optical holder implemented with an optical fiber inserted through the holder, on the side of a specimen. The reflectors and optical fiber are placed away from the TEM optical axis. The light-collecting solid angle is approximately 1.3 strad, approximately 100 times larger than that of their first generation prototype. The sample is mounted at the end of the metal wire, which position can be controlled to the focal point of the mirror by a piezo-driven manipulator. In years of 2012-2013, a few groups, including us, secured the optical holder (beta version) from *Nanofactory Instruments*.

One of the groups is in Brookhaven National Laboratory. Yimei Zhu et al. obtained the prototype optical holder from *Nanofactory* which allows for two optical fibers and several delicate mirrors to direct the light beam to a specimen.

A multimodal optical nanoprobe allows scientists to perform standard experiments natural for TEM in addition to those involving optical excitation and measurements on the sample, including electrical

measurements, STM and combinations of those. They emphasized the ability to simultaneously measure optical and electrical properties of the sample at the nanoscale.[129] The operations introduced were very similar to our case, but their serious problems were related to the calibration of light spot location, which had been realized by the adjustment of the tiny mirror screws; also, they were not able to confirm the location of light spot. Therefore the system was not that practical.

Minor et al. have implemented an *in situ* TEM monitoring technique to observe the crystallization of a-Si during high power pulsed laser irradiation by directly coupling laser into a TEM through a fiber-optics probe. By realizing a near-field scanning optical microscopy (NSOM) fiber probe scheme, this technique opens up a wide variety of new characterization possibilities.[108]

Kociak et al. of the Université Paris-Sud [121] developed a STEM-CL system on a *Nion* microscope which also uses an optical fiber as a light guide from the microscope column to the CCD camera outside the microscope. The light is collected by the specially designed mirror system of which the focus point is on the specimen. This CL-STEM imaging can be applied to obtaining luminescence spectra and observing the structures simultaneously.[59]

Organization	Fiber	Through	Probing contact	Practical for
Nagoya U.	Yes	hole, holder direct	No	CL
BNL	Yes	holder by sides	Yes	N/A
LBNL	Yes	holder direct	No	NSOM heating
U. Paris-Sud	Yes	holder direct	No	CL-Map, NSOM
ASU	Yes	detector/aperture	No	Photochem.
NIMS	Yes	holder direct	Yes	all above

Table 2.2: Comparison of the groups which introduced light to TEM.

In another group, Miller in Prof. Crozier's group in Arizona State University replaced the EDS detector (first version) or objective aperture (second version on a FEI Titan microscope) with an optical fiber to shine a light onto chemicals to observe dynamics of photochemical reactions.[56] But the problem was that they had not been sure about the location of the light spot, because they just could not observe it.

To conclude, by introducing light into TEM, these days, the researchers are capable of observing dynamics of photochemical processes or thermo-effects, and to simultaneously obtain high resolution CL with EELS and Dark field imaging. As summarized in Table 2.2, almost all groups used optical fibers for introducing light rather than lens system on bench, whereas most groups do not offer probing contact capabilities. In my case (NIMS in Table), I would like to realize all these functions based on the redesigned optical holder.

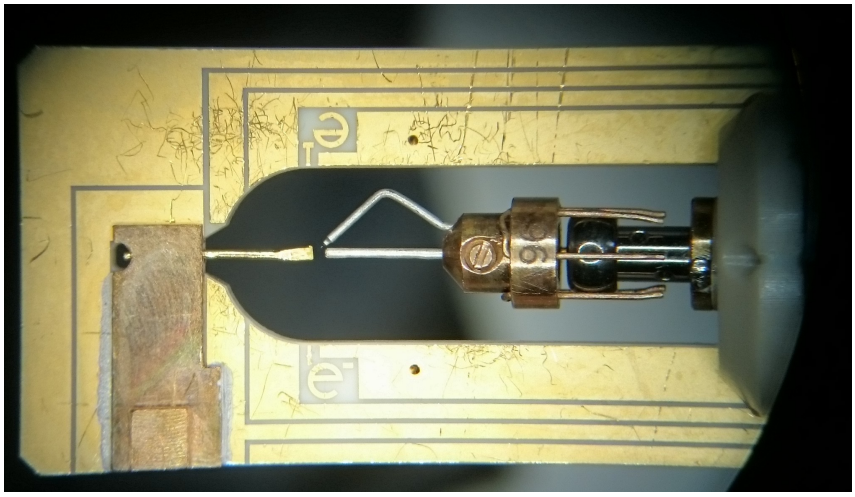

Figure 2.3: The part of a holder inside the pole-piece of TEM to illustrate geometrical relationship between sample stage, probe, fiber and electron beam.

2.2.2 Our holder adaption

To choose between the fiber technology and the breadboard, it is necessary to define the objectives and a budget. A honeycomb core breadboard is a complex and powerful layout to customize optical input/output parameters with high precision.

However, building of an optical system on a honeycomb core breadboard could be costly. At least one optical window should be opened on the body of a microscope, so as to transmit an aligned laser beam into the chamber, and to collect optical signal from it. In contrast, by using an optical fiber, a laser light could be easily introduced into the microscope without breaking the TEM column. The solution is to make a continuous hole through a special TEM holder, so as to insert an optical fiber in it. The former *Nanofactory Instruments AB* developed a holder for our Laboratory with a 250 micrometer pipeline.

In our system, the microscope is not modified at all, and we integrate all the experimental dynamics through the specimen holder.

The front frame of the special holder was placed into the 4 mm gap of the TEM pole piece. And with the optical fiber inserted, the light connection between the TEM chamber and the outer space was realized.

To develop the whole system based on the regarded general idea, the two issues for the setup should be of our prime concern. One issue is the inner TEM side – how to place the samples, how to design the fiber tip, how to operate and apply/test electrical signals on the samples. The other side is the outer TEM side – board development, space for light source and signal processing.

I proposed 4 ways to add electrical capabilities to the piezo-driven optical holder based on the *Nanofactory* optical holder, as shown in Figure 2.2. The are namely:

a) To build the separated arms on the frame and to place a sample across the arms (this can be very

Figure 2.4: The holder has several I/O ports for *in situ* mechanical, electrical and optical access.

difficult) where it can be illuminated;

b) To drill a hole on the original cap, or to make a new hat with two holes and to install an additional probe;

c) Based on design b), one end of a gold wire can be placed on the electrical pad using a wire bonding machine, the other end of wire can be manipulated to make contact with the specimen, therefore, in total three electrodes become available;

d) To coat a conductive metal onto the surface (cross section is not affected) of the optical fiber (which is marked in yellow), the coating electrically joins the end (edge) of the fiber and the cap (an electrode);

The possible ideas are not limited by these four ways. Combinations of a) and b), or a) and d) are also possible. By building arm(s), installing probe(s), bonding wire(s) and coating conducting layers, electrical probing can enrich the functionality of the optical holder.

Considering the fact that attaching a probe onto the piezotube driven hat would enable more dynamic options available for our microscopy, I finally decided to drill a hole on side of the hat and to attach an additional metallic probe to it, while at the same time to coat a gold layer onto the fiber tip to reduce fiber charging during its exposure to an electron beam.

For nanostructures, sampling is rather easy, the samples can be attached to the gold wire tip by touching, pressing, dipping or dropping, so that they could finally be exposed to an electron beam. However,

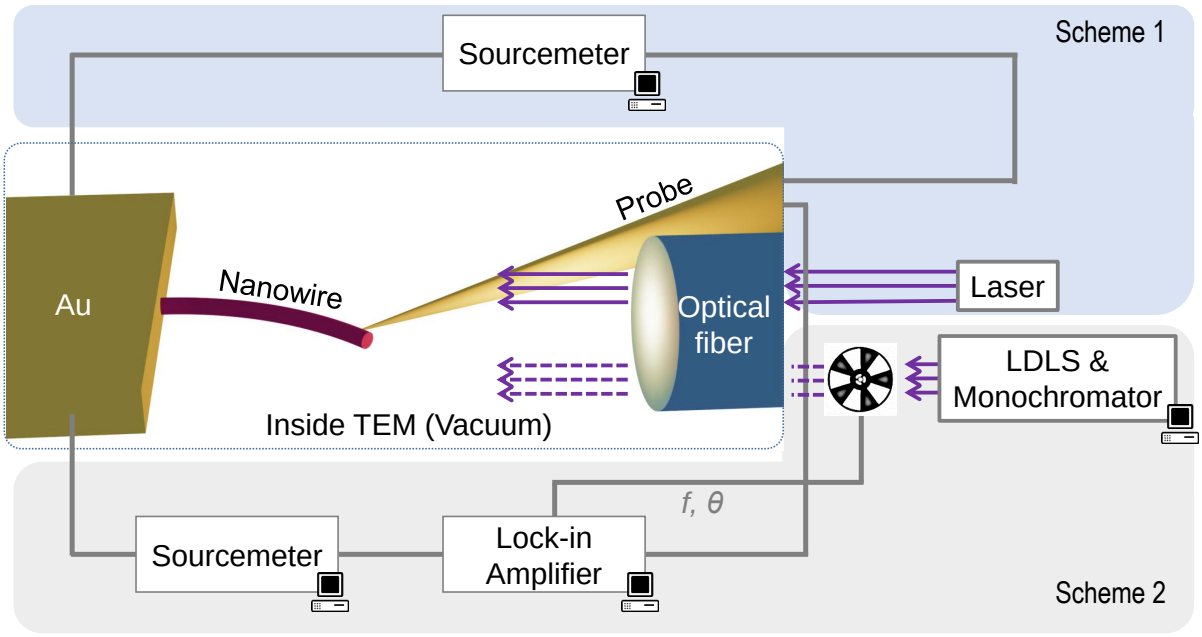

Figure 2.5: Optoelectronic *in situ* TEM scheme with two different light sources.

the optoelectronic *in situ* system could be more complex. The fiber tip inside TEM is clamped by a specialized cap which is driven by a XYZ-piezo controller. A tungsten probe for manipulation and electrical contacting is attached on the specialized cap manually.

Therefore, the sample is exposed to the electron beam and light, while, at the same time, it is controlled and connected by the stage (gold wire) and the tungsten probe.

For thicker samples, the specimens can be made by using a focused-ion beam (FIB) technique, or a half TEM grid may be used. The alignments of a sample, a fiber tip and the probe are quite important whereas rather difficult. If the fiber tip is far away from the sample, then the light will be divergent; this means that the power intensity of light could be reduced in progression. Since the tungsten probe will approach and connect the sample, the fiber tip should be as close as possible to the probe also.

In Figure 2.3, an image shows the geometrical relationship between the sample stage, probe, the fiber tip and electron beam.

2.2.3 Outer part of the microscope

The individual coaxial electrical wiring through the holder for each contact gives pA level noises during the electrical measurements, allowing to measure low currents in Ohmic and non-Ohmic contact conditions.

As shown in Figure 2.4, the holder has several ports for electrical, mechanical and optical signals to go in and out. The mechanical wire is at the downside, which is connected to the holder controller. The two electrical wires on top are connected to various electrical units depending on the experimental goal.

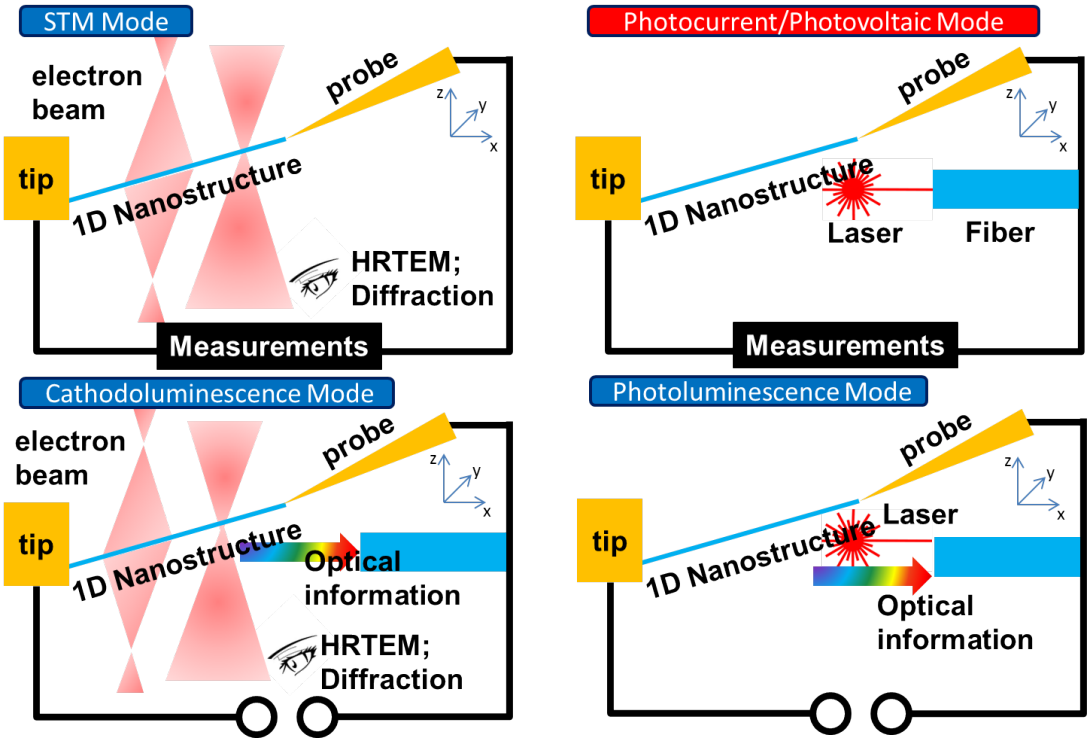

Figure 2.6: Four modes of light-compatible *in situ* TEM.

At the bottom of the holder, optical fiber goes through and may serve as either a light source or a light detector, depending on application.

A lock-in amplifier is used to extract a signal with an understandable carrier wave from a relatively noisy background. Because the light signal or photocurrent signal produced from a nanoscaled structure could be rather weak, detecting the signal against a bright noise could be accomplished using such amplifier. For example, in order to detect the photocurrents as a function of the wavelength of the incident beam one can apply a strong white light source, a chopper, a monochromator, a low-noise amperemeter and a lock-in amplifier, whereas the probe allows for measuring the electronic and optoelectronic responses.

Thus, the optical *in situ* TEM system was developed and optimized by me during the last few years. It is now multi-functional: as shown in Figure 2.5: the white light source and monochromator are used together with the chopper and lock-in amplifier to measure the photocurrents as a function of wavelength. The laser diodes and wave signal generator are used together with the lock-in amplifier to measure photocurrents and photovoltages at a certain wavelength.

The final system is fully compatible with both the laser light source and other light sources such as the Lazer-Driven Light Source (LDLS, Energetiq Technology, Inc.) used by us. Usually, the white light source is utilized in tandem with a monochromator.

2.3 Applications and limitations

2.3.1 Applications

The interface morphology, the contact area and orientation, the material crystallography - all of these factors can precisely be determined under high resolution microscopy, while a bias and a light applied onto the sample.

Four modes were designed for different purposes. These modes are demonstrated in Figure 2.6.

The first mode is the conventional STM-TEM mode, which allows for controlling, measuring and observing a nanostructure. This mode is used to manipulate with the structures and to observe the samples for detailed imaging, including high-resolution imaging and diffraction analysis. The system is also capable for applying chemical functions to the specimen for electrochemical experiments inside TEM.

The second mode is thought to be the most effective one. Photocurrent and photovoltage could be measured in addition to the conventional STM-TEM mode. However, in order to get rid of the influence of electron beam on the sample, it should often be moved away from the sample when measuring.

The third mode is the CL mode. On the opposite way, the optical signal could be obtained through the fiber tip when one applies an electron beam to the structures. By collecting the optical signal from a specimen through the optical fiber, spatially resolved CL information can be gained and correlated to the crystallography information. Also electrical biasing or current flow are optional in this mode.

The fourth mode is the photoluminescence mode. The interference is only happened when two coherent waves are superimposed. The system is not yet available, but it is possible to be established.

In Figure 2.7, the relationships between all factors are presented. The applications of our light-compatible probing *in situ* TEM are not restricted to optoelectronics, flexible electronics/optoelectronics and lithium/sodium ion batteries, which are detailed in Chapters 3-6. More fields, such as a research on CL, PL, photovoltaic and photochemistry applications are expected to be explored in the nearest future.

2.3.2 Limitations

First, the system is based on TEM, therefore, all limitations of TEM are also applied to our system; that is, the sampling requirement is strict, the sampling efficiency is low, TEM imaging gives only 2D information, and electron beam may either damage a specimen, or interfere the experiment.

Secondly, the incident beam is limited by the properties of the optical fiber and the light source. The optical fiber is not easy to replace, and is not recommended to do this frequently. Also, the optical fibers always have their own band pass windows for light, as well as maximum power limitations. For special requirements, for example, for UV/NIR light experiments, a proper UV/NIR light source and a proper UV/NIR fiber are required, the polarization of light needs a special optical fiber, etc.

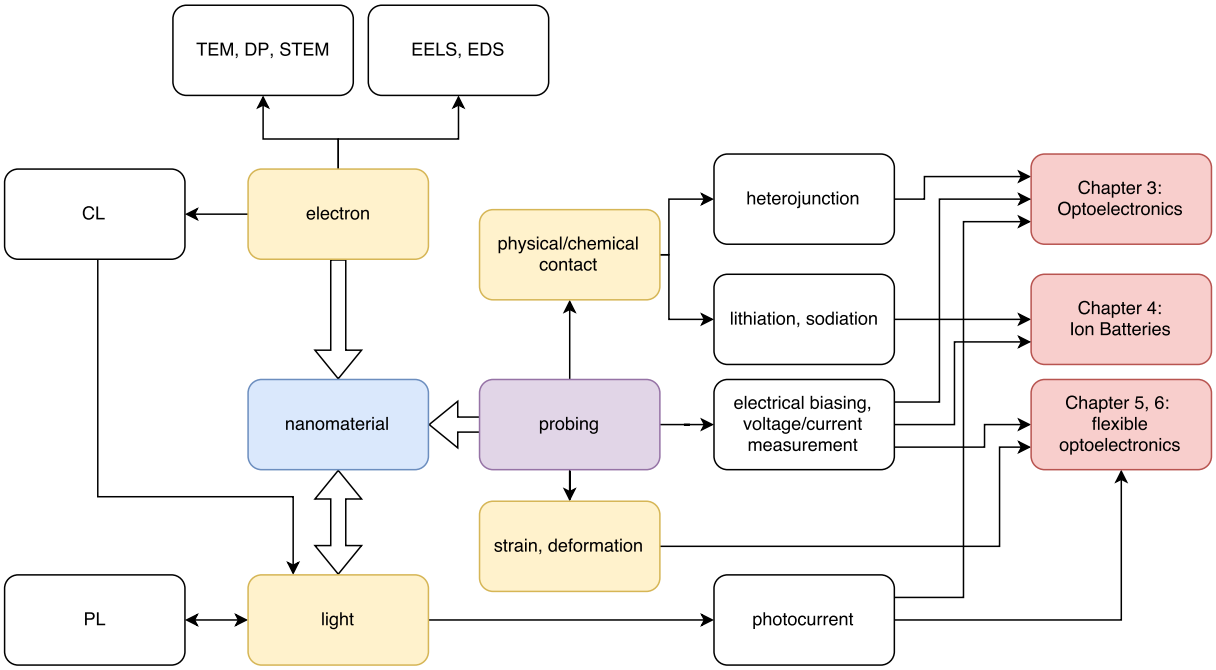

Figure 2.7: Relationships between factors and applications. Important dynamics is marked by yellow, some applications are marked by red, which will be detailed in other Chapters.

Thirdly, the mechanical force is not measurable. Even though I list mechanics as one factor of the system, the mechanical information is quite limited and is only related to the manipulation. In fact, we are able to see a strain (and then evaluate the force by simulations, at least qualitatively) based on deviations on 2D TEM images or diffraction patters, but we are not able to measure the detailed force values or strain/stress distributions directly.

However well designed experiments and professional manipulations can eliminate, or, at least, reduce the burden of the limitations mentioned above.

3

Nanoarchitechtonics of Axial Nanowire Junctions of CdS and p-Si

A DELICATE, HIGH-PRECISION TECHNIQUE was implemented to build and analyze axial nanowire heterojunctions inside a high-resolution transmission electron microscope (HRTEM). Through *in-tandem* using of a sharp tungsten probe as the nanomanipulator and an optical fiber as the optical waveguide the nanoscale CdS/p-Si axial nanowire junctions were constructed, and *in situ* recorded photocurrents from them were detected. Compared to the individual constituting nanowires, the CdS/p-Si axial nanowire junctions exhibit a photocurrent saturation effect which protects them from damage under high voltages. In addition, a set of experiments demonstrates the certain relationship between the saturation photocurrent values and the incident light intensities. The designed technique is envisaged to be valuable for bottom-up nanodevice fabrications, and the documented photocurrent saturation feature should solve the Joule heating-induced failure problem in nanowire-based optoelectronic devices caused by a fluctuating bias.

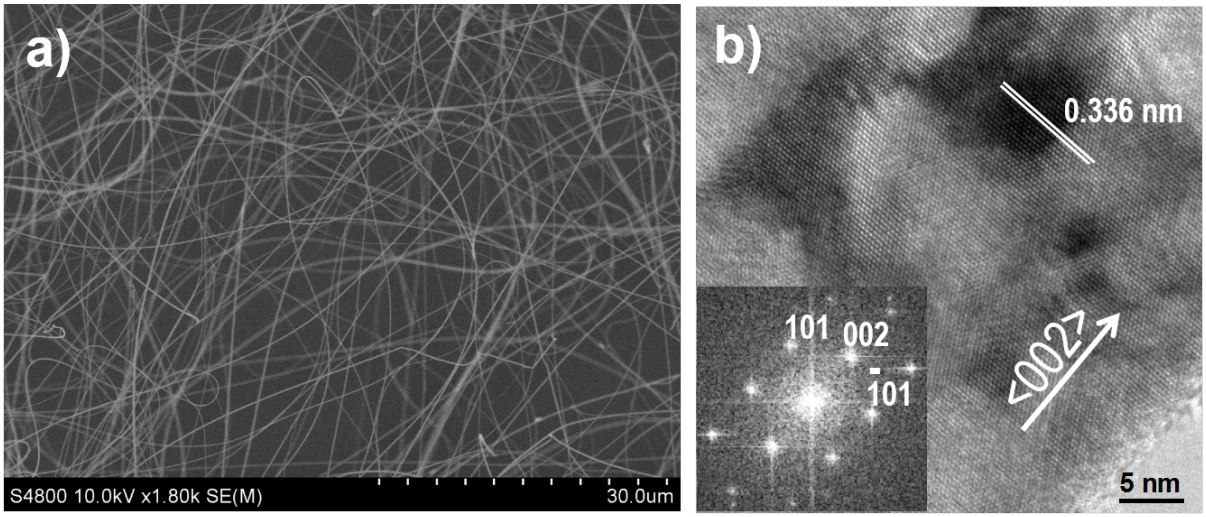

Figure 3.1: (a) SEM image of CdS nanowires. (b) TEM image and corresponding fast Fourier transform pattern of an individual CdS nanowire.

3.1 Introduction

These days, the the key progresses in nanoscale photonics and electronics are made thanks to the significant improvement of device functions and performances. Nanowires, as prime building blocks in the bottom-up technology, have been shown to be the key candidates for the next generation booming nanophotonic applications because of their good crystallinity, high carrier mobility, confinement effects and infinite possibilities of assembling any required architecture for diverse utilizations [63, 80, 89]. However, till now, fabrication of a desired nanoarchitecture employing nanoscale building blocks has been a challenge. Several nanowire-based devices, such as transistors [10, 14, 42], diodes [41], photodetectors [82, 88] and logic circuits [55, 114], have successfully been constructed on substrates through diverse lithography techniques. By contrast, controlled manipulation with two or more individual objects with a nanoscale precision and on-site creation of axial heteroarchitectures made of them (for the immediate optoelectronic probing) has never been tried. Building of the regarded junctions and *in situ* testing of their optoelectronic characteristics must be highly important in relation to the "nanoarhitectonics" concept and uncovering novel physical properties and phenomena.

Cadmium sulfide (CdS) is known as one of the key materials in heterostructured type solar cells because of its advantageous type II window band structure [11]. Also, it was shown that merging CdS and Si materials must create a decent junction. Therefore, numerous new functions and utilizations may be envisioned. In addition, a careful study revealed that CdS/p-type-Si junctions are basically better than CdS/n-type-Si junctions for rectifying properties because of their specific type II band structure [97]. Nevertheless, reliable usage of these two "hot" optical materials, i.e. CdS and Si, is rather rare, because both junction constituents are not transparent to a solar light. And the normal layered structures are considered not to be efficient. In order to directly expose the heterojunctions to the light, a smart way

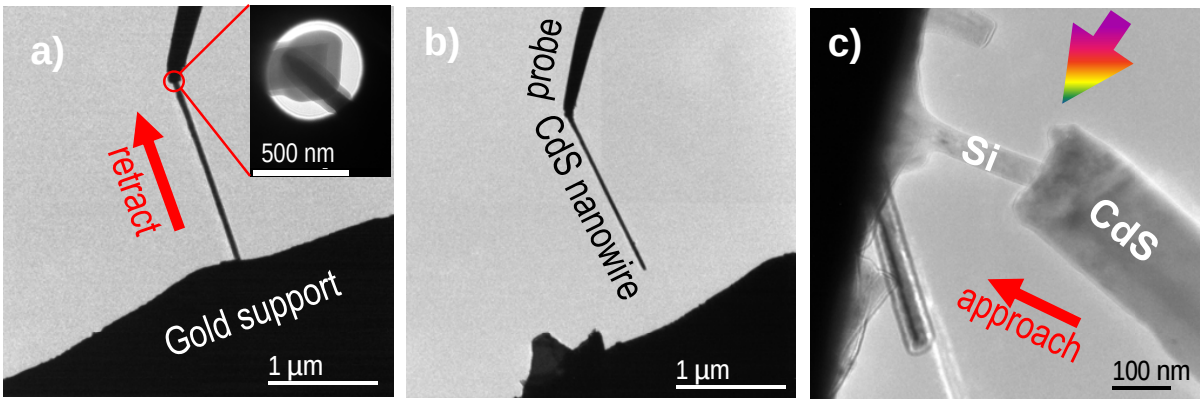

Figure 3.2: *In situ* TEM images illustrating the construction of an axial CdS/p-Si nanowire junction during manipulations in HRTEM. (a) Achieving a physical contact of a piezo-driven sharp W probe with an individual clean CdS nanowire on an Au support during the first stage of the process; the inset depicts soldering the W probe and the wire under convergent electron beam irradiation. (b) Retracting the nanowire from the Au support; (c) Attaching a CdS nanowire to the individual boron-doped Si nanowire during the second stage of the manipulation. The incoming light illuminating the junction is shown with an arrow.

is to build the nanowire array structures [26, 38]. In addition to the wide-spread core-shell nanowire ensembles, constructing axial nanowire heterojunctions by means of two semiconducting materials is a promising experimental route.

Following previously made axial nanowire heterojunctions for diverse optoelectronic applications, CdS nanowires and B-doped Si nanowires have been selected by me as the targeting building blocks. Thus, in this Chapter, I demonstrate an accurate nanomanipulation technique pioneered in a HRTEM for building new axial nanowire architectures. Direct *in situ* electronic and optoelectronic tests are then performed on them using the light of various wavelengths illuminating the objects of interest in TEM. The careful experiments allow me to also simultaneously have an entire control over the crystallography and spatially-resolved chemistry of the two constituting domains and their interfacial region before, during and after optoelectronic probing with high spatial and temporal resolutions specifically peculiar to HRTEM. My experiments reveal clear photosensing properties of the axial CdS/p-Si nanowire junctions. The latter demonstrate selective sensitivity to blue and purple lights rather than to the light of larger wavelengths. Also, the junctions display a photocurrent saturation effect. This implies that such junctions are applicable for detection of light intensities due to their low energy consumption and stability under unexpectedly pulsing biases.

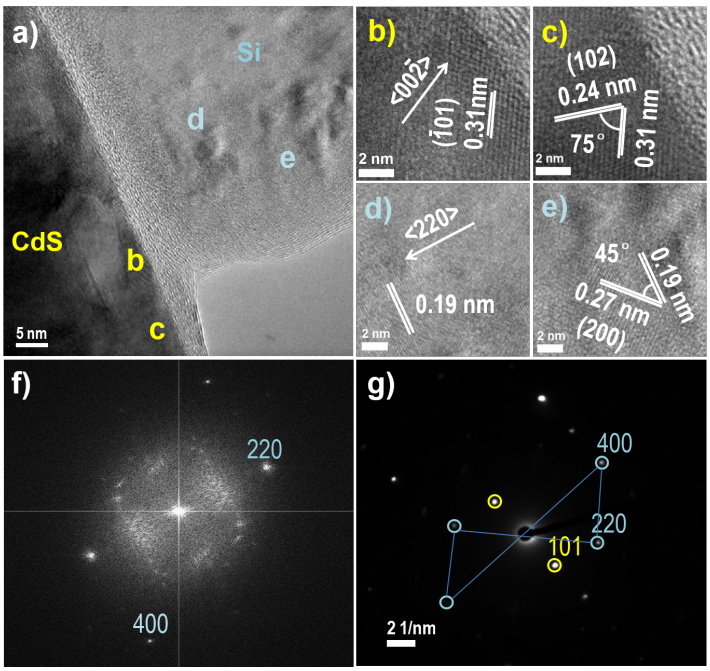

Figure 3.3: (a) Overall HRTEM image of the interfacial portion of the produced CdS-p-Si junction; (b)–(e) HRTEM images acquired in the areas marked in (a); these reveal the single-crystalline nature of both nanowire segments, and (f), (g) corresponding FFT pattern and selected area electron diffraction pattern (SAED) taken from the interface. Peculiar crystallographic orientations (b)–(e) and diffraction spots (f), (g) are marked.

3.2 Experimental

3.2.1 Material Synthesis

The CdS nanowires were prepared using an Au-catalysed vapor-liquid-solid (VLS) synthesis in a chemical vapor deposition (CVD) system, which is analogous to that used in many works [43, 124]. 1 gram of a CdS powder (99.995%) was put on a graphite plate in the tubular furnace center as the source material. A (100) Si wafer covered with a 10 nm thick Au film was put on the other graphite piece located downstream, at a distance of 11.5 cm from the tube center. The tube was purged under N2 flow at 200 °C for 2 h, and then heated to 1000 °C at a rate of 30 °C per min. After 30 min of synthesis, the furnace was naturally cooled down to room temperature. The process proceeded under a N_2 flow of 300 sccm. A wool-like yellowish product was found on the Si substrate after cooling. Si nanowires were fabricated via VLS mechanism in a separate CVD system. Au particles of 3 nm in diameter were taken as a metal catalyst. The boron-doped nanowires were directly prepared onto Au-coated (111) Si substrates at 600°C for 30 min in a flowing 19 sccm of SiH_4 as a Si reactant gas, and diborane (B_2H_6) was employed as a B precursor. The B_2H_6 flow in H_2 was 0.2 sccm and 30 sccm of N_2 served as the carrier gas. Other details related to boron-doped Si nanowires characterizations were presented in the literature. [22, 23, 78].

3.2.2 Techniques

Field-emission scanning electron microscopy (FE-SEM) of the prepared nanostructures was performed on a Hitachi S-4800 FE-SEM operated at 10 kV. HRTEM analysis and *in situ* experiments were carried out using an optimized piezo-driven optical TEM holder, which is discribed in detail in Chapter 2, in an energy-filtering 300 kV JEM 3100FEF (Omega Filter) high-resolution TEM. The multimode fiber (Nanonics Imaging, Ltd.) was threaded through the holder inner channel. The fiber was connected to four laser diodes, with 405, 488, 638 and 808 nm wavelengths, and a tunable power and temperature (Thorlabs, Inc.) were used.

The working temperatures of laser diodes were set at 30°C. Firstly, the numerous CdS nanowires were placed onto a fresh-cut flattened Au tip covered with an electrically conductive Ag epoxy under the flash tip immersing into the CdS nanopowder sample. After heating the paint, the Au tip with the specimen was placed within the sample holder. The ultrasharp W probes used as counter-electrodes and manipulators were prepared under NaOH electrochemical etching. The W tip movements were controlled inside TEM in 3 dimensions using a piezoelectric motor for making a contact, and to test and retract the selected CdS nanowires which had been conveniently oriented with respect to the manipulator. Then the construction of axial CdS/p-Si nanowire junctions was gently performed in two steps, as described below. Typically, prior to contacting the two nanowire building blocks, an electron beam was applied to focus on the tip-ends of both CdS and p-Si nanowires for 30 s to clean the surfaces. The current–voltage (I–V) curves were recorded by using a Keithley 2612B sourcemeter. The electron beam was deliberately blanked during obtaining the quantitative current data.

3.3 Results and discussions

As depicted in SEM image of Figure 3.1a, prepared CdS nanowires, $>$ 50 μm long, were evenly distributed over a Si substrate over a large area. In Figure 3.1b, a high-resolution TEM image and the fast Fourier transform pattern (FFT) confirm that an individual nanowire has a well-crystallized hexagonal structure. The growth direction is parallel to the *c*-axis and the lattice parameter $c = 0.672$ nm.

Because the deoxidized Si nanowires are less stable than CdS nanowires in air, for constructing heterojunctions, it was important to transfer a CdS nanowire into the HRTEM first, and then to contact a Si nanowire, not *vice versa*. As shown in Figure 3.2a, the sharp W probe was carefully manipulated inside the microscope to touch a pre-selected clean individual CdS nanowire on the Au stage. To pull out the CdS nanowire from the sample stage, an electron-beam soldering, i.e. "glue" technique, was utilized for making the tight contact between the probe and the nanowire.

As illustrated in the inset of Figure 3.2a, by focusing a convergent electron beam (about 500 nm in diameter) on the contact area for 20 min, nearly 75 nm thick layer of the residual amorphous carbon (al-

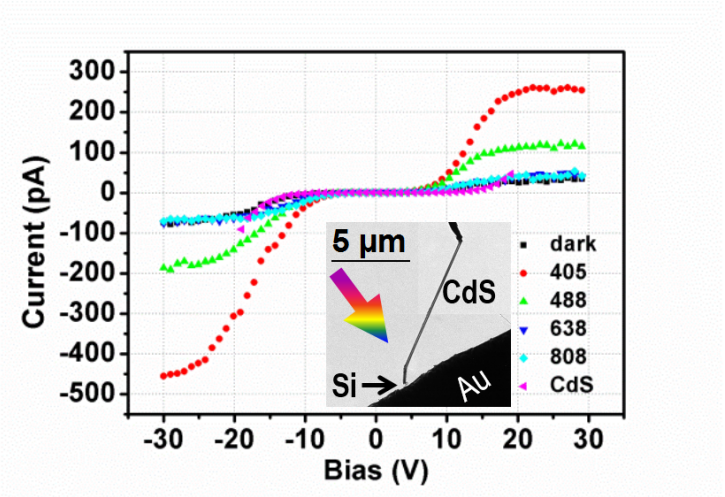

Figure 3.4: A photocurrent outcome of an individual CdS/p-Si axial nanowire junction under dark conditions and during illumination with the light of different wavelengths but of fixed intensity. The inset illustrates the low-magnification TEM image of the CdS nanowire under probing. The multi-coloured arrow reflects the incident incoming light; the black arrow notes a short Si-branch segment.

ways present in the TEM chamber from lenses, apertures etc.) formed on the probe/nanowire surfaces resulting in their intimate nano-soldering.

Then, the targeted CdS nanowire was detached from the Au sample tip under delicate pulling back the W probe, as shown in Figure 3.2b. To build a final heterojunction, the second step was to physically attach the retracted CdS nanowire to a pre-selected single B-doped-Si nanowire. To do so, after pulling-out the holder (with the regarded CdS nanowire adhered to the W probe) from the microscope, the gold sample stage with CdS nanowires was replaced in HRTEM by the fresh Au sample stage with attached numerous deoxidized B-doped Si nanowires. By delicate approaching and touching the end of the CdS nanowire probe to a selected Si nanowire tip, the axial heterojunction architecture was created. Figure 3.2c depicts a representative CdS/p-Si axial nanowire junction. These branched CdS and Si nanowires have diameters of 187 nm and 46 nm, respectively. The electron beam current was immediately weakened after the junction had been made. This was done to prevent the nanostructure overexposure to the electrons which would lead to insurmountable structural changes, e.g. formation of irradiation-induced defects in the material.

Then, a detailed structural study of the junction was conducted using HRTEM imaging and electron diffraction analysis. The HRTEM images of a given CdS/p-Si axial heterojunction are depicted in Figure 3.3. These confirm that both structures are perfect single crystals. The contact interface between two nanowires is atomically smooth. A thin transient graphitic layer is noticed between the wires. It has the origin similar to that mentioned above. In Figure 3.3a, the left-hand-side panel shows the CdS nanowire, whereas the right-hand-side depicts the B-doped Si nanowire. Figures 3.3b and 3.3c present the entire crystallography of the CdS branch. Figure 3.3d and 3.3e present the crystal lattice of the constituting Si

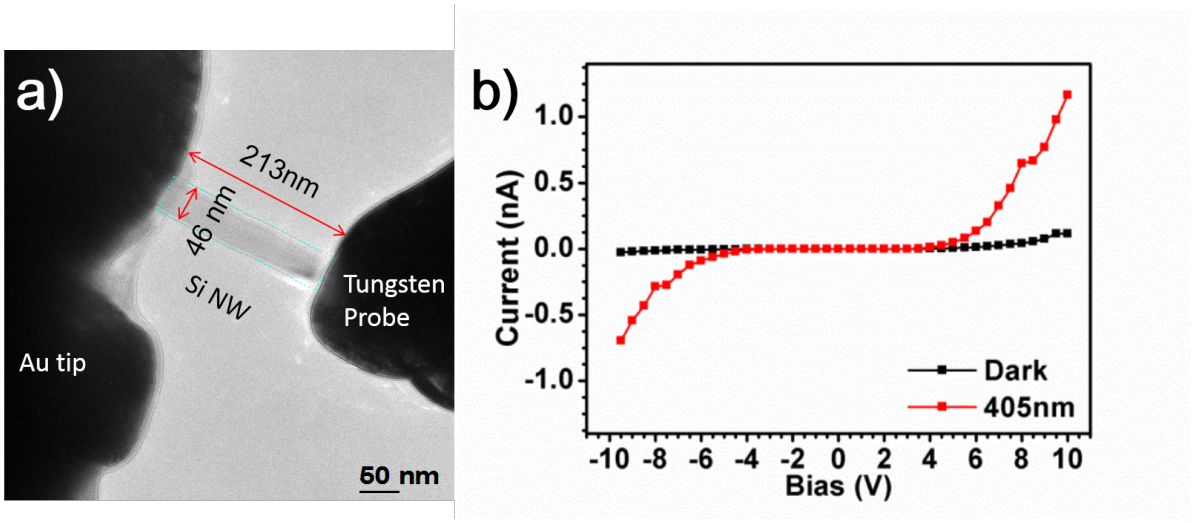

Figure 3.5: (a) *In situ* alignment of a single B-doped Si nanowire for photocurrent measurements. (b) Dark current and photocurrent from the nanowire.

nanowire. Figure 3.3f is the fast Fourier transform pattern of Figure 3.3a. Figure 3.3g is the selected area diffraction pattern taken at the junction interfacial portion. After the detailed structural analysis, which confirmed that high-quality axial heterojunction, constructed of two defect-free pure nanowire single crystals, had indeed been prepared, electrical and optoelectronic tests on it were promptly started.

While applying a voltage and illuminating the preformed CdS/p-Si heterojunction with a light through the optical fiber threaded inside the holder, dark current and photocurrent data were collected. Figure 3.4 illustrate a typical current – voltage diagram of a junction illuminated with lasers of 4 different wavelengths. The powers of all laser diodes were fixed to be the same, 13 mW. A photocurrent from the junction at 405 nm was larger than that at 488 nm, and much higher than those at 638 nm, and 808 nm, and the dark current. Because laser diode wavelengths of 405 nm, 488 nm, 638 nm and 808 nm correspond to energies of 3.06 eV, 2.54 eV, 1.94 eV and 1.53 eV, respectively, while CdS and Si nanowire band gaps are 2.4 eV and 1.5 eV, respectively, [18], the heterostructure light absorption at 3.06 eV and 2.54 eV must be more prominent than that at the energy <2.4 eV. The better photoresponse at 3.06 eV compared to that at 2.54 eV could reflect a complicated band diagram of the heterojunction which creates more light absorption capabilities at a higher energy, and thus results in numerous photo-induced carriers.

The I-V curves of the CdS/p-Si axial junction, where CdS is assumed to be an n-type semiconductor (due to S vacancies), and B-doped Si as a p-type semiconductor, did not display ideal p-n junction parameters. In the forward bias regime, below 10 V, the I-V curves reveal low currents, and the currents tend to be saturated at a bias higher than 20 V. In the reverse bias regime, the currents also display a saturation tendency, over 30 V.

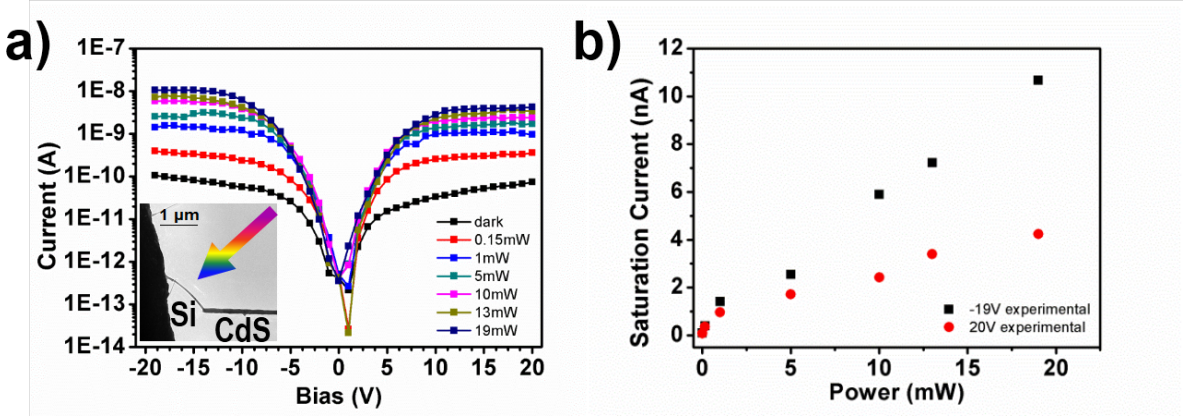

Figure 3.6: Saturation trends of photocurrent and dark current at different of light intensities. (a) I–V curves recorded at various powers of lasers; the inset illustrates the low-magnification TEM image of the structure under testing; the multi-coloured arrow directs the light incidence; (b) current-laser power plots at the two selected biases.

For a comparison it should be noted that, for an individual CdS nanowire or a B-doped Si nanowire, saturation did not occur up to 10 V, as marked in Figure 3.4 and Figure 3.5. Once a bias larger than 10 V had been applied to a single CdS or Si nanowire, their structural breakdown readily happened. This was due to resistive heating at a high current density. [107] In my experiments, the single crystalline nanowires (having narrow contact areas with the electrodes) were particularly vulnerable to current densities larger than $104\,A \cdot cm^{-2}$. Therefore, it is apparent that the CdS/p-Si junction effectively hampered the current density at a high bias, and thus the whole junction ensemble is not deteriorated.

Test experimental runs were performed to understand the associated factors responsible for the current saturation. As marked in Figure 3.6, by recording photocurrents for different light intensities at 488 nm, we observed that photocurrents and dark current of the CdS/p-Si axial nanowire junction at changing laser powers were saturated accordingly.The saturated currents were proportional to the laser diode power. Such phenomenon implies that the CdS/p-Si junction transfers light intensity into an electrical signal with the unmatched voltage tolerance. As shown in Figure 3.7, another junction with a smaller contact area, which was irradiated by a 405 nm laser at 13 mW, also demonstrated a profound saturation effect. The photocurrent saturated at 5 V, the saturation current values were 15 nA and –75 nA. Therefore, it is likely that the junction contact conditions mainly determine the saturation threshold and the current value. Primarily, the photocurrents in nanowire photodetectors are proportional to the voltage [52], while, simultaneously, they are proportional to the light intensity. This implies that the voltage should be certain and stable within a decent tolerance for reliable light detection. Therefore, the currently built CdS/p-Si axial nanowire junctions reveal a good promise toward light intensity sensing not only because they can limit the current density at a high voltage, but also because they do not require an entirely stable voltage.

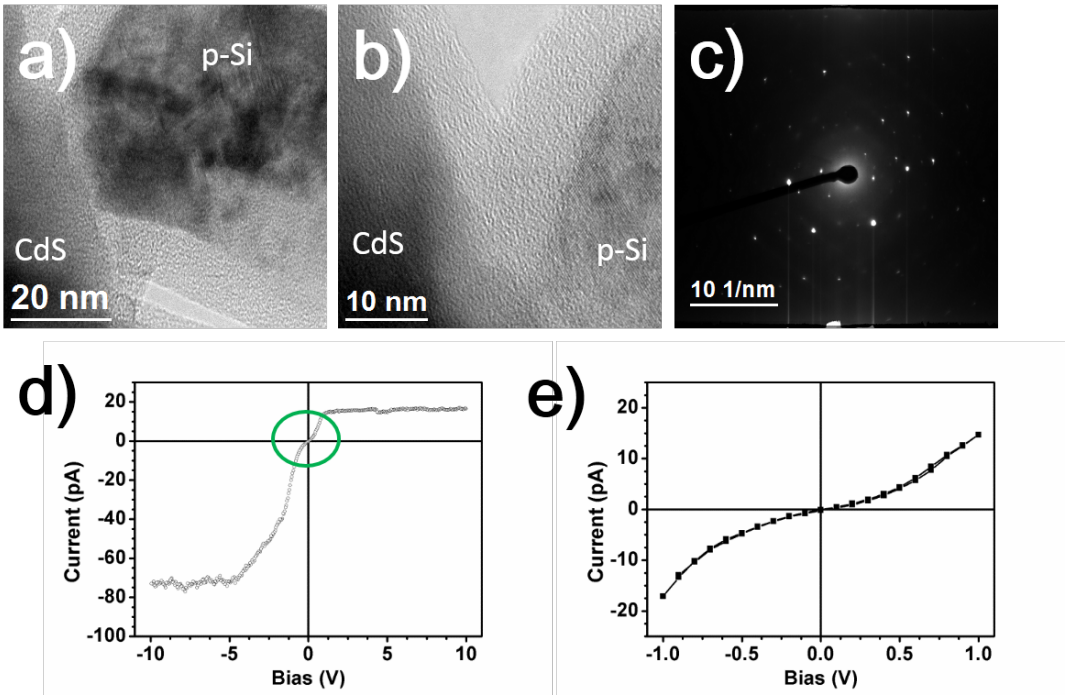

Figure 3.7: (a,b) TEM images, and (c) SAED pattern of a CdS/p-Si junction having the narrow contact region. (d-e) Photocurrent measurements on this junction.

The observed phenomenon of photocurrent saturation at the high bias levels seems to to be analogous to that discovered for a planar Metal-Semiconductor-Metal (MSM) photodetector [70], electron beam excited CdS single crystals [16], a model p-n junction [57] and a p-n junction solar cell [27]. Firstly, the electron beam excitation mechanism should be not taken into account, because the electron beam was shut during the measurements, and it did not have a continuous effect on the material photocurrent [16]. Secondly, the prepared CdS nanowires were confirmed to be defect-free single crystals with a marginal number of sulfur vacancies, and, thus, they did not operate as a heavily doped donor. For an ideal p-n junction, the dark current is written as:

$$I = I_s \left(e^{\frac{V_D}{nV_t}} - 1 \right) \tag{1}$$

Equation (1) is named as Shockley's diode equation [81] and the dark current density of a non-ideal diode could be expressed as:

$$J_F \approx -\frac{q(2D_p)N_i}{L_p} e^{\frac{qV}{mk_oT}} \tag{2}$$

The factor m in Equation (2) is changeable. Under circumstances of very low and very large biases, $m = 2$, and $J_F \propto e^{\frac{qV}{k_oT}}$, the recombination current or the high injection takes an effect, current densities increase linearly; when bias is on a medium level, $m = 1$, $J_F \propto e^{\frac{qv}{2k_oT}}$, the diffusion current becomes important, and the current density exponentially increases. This is similar to the observed I-V curve

trends, but Equation (2) does neither exactly explain the photocurrent saturation phenomenon nor the relationship between the saturation current value and incident light intensity. From the theory of photocurrent saturation developed by Mohammad and Abidi [57], for lightly degenerated semiconductors, where spatial variations of effective mass, carrier lifetime their mobility and diffusivity, and dielectric constant, are marginal and may be neglected, the total current is expressed as:

$$I = Aqg\left(L_n^* + L_p^*\right) - \frac{\left(e^{\frac{qV_j}{kT}-1}\right)\cdot\left(I_o + I_o' e^{-z}\right)}{1 - e^{-2z+z_1+z_2}} \tag{3}$$

where,

$$I_o = \frac{qA}{\tau_a}(n_o(x_{p2})L_n^* + p_o(x_{n2})L_p^*)$$

$$I_o = \frac{qA}{\tau_a}(n_o(x_{p2})L_p^* e^{z_2} + p_o(x_{n2})L_n^* e^{z_1})$$

$$L_n^* = L_p^* = L_a = \sqrt{D_a\tau_a}$$

D_a, τ_a and g are defined as ambipolar-diffusion coefficient, ambipolar lifetime and amibipolar-carrier generation rate, respectively[57]. We do not neglect injection, V_j, V_d, and it is considered that $z_1 = z_2 = 0, z = \frac{q}{kT}(V_d - V_j)$ in nondegenerated semiconductors with uniform doping, Equation (3) could be written as:

$$I = 2qAg\sqrt{D_a\tau_a} - k_v(n_o x_{p2} + p_o x_{n2}) \tag{4}$$

k_v is defined as a factor to simplify the equation. The first term in the right-hand side of this formula represents the uncompensated current relative to light intensity, and the second term stands for the reduction of this photocurrent owing to spatial dependence of band structure of the junction and the junction potential produced by strong injection. For a single B-doped Si or a defect-free CdS nanowire, the current density increases with bias, as this does for a standard semiconductor nanowire with Schottky contacts. However, for the CdS/p-Si nanowire junctions with a limited junction area and under a large bias, the second term in Equation (4) becomes negligible, and, thus, the photocurrent does not increase with a bias but does with the light intensity. The observed saturation current values in accord with the incident light intensities can be explained based on several factors. Because a sufficient bias must be applied to have the flat band at the anode and separate the generated carriers, after the threshold bias, the photocurrent started to notably rise, but when the bias is large enough, effective carriers produced by the incident light become saturated for transmission. In addition, we claim that the CdS/p-Si axial nanowire heterostructures are particularly sensitive to 3 factors: the relative dimensions of the two building blocks (this affects carrier mobility), carrier density and light absorption efficiency; interface crystallography (which also determines the mobility), junction parameters; and light intensity; that influences the photocurrent saturation value.

Experiment No.	1	2	3	4	5
CdS NW Length (μm)	3	0.8	1.6	10	13
CdS NW Diameter (nm)	240	38	135	187	120
Si NW Length (μm)	0.9	1.5	1.3	0.2	1
Si NW Diameter (nm)	55	44	44	46	63
Photoresponse detected	26/26	22/22	16/16	57/57	16/16
Saturation current positive (nA)	16	0.50	3.2	0.12	0.16
Saturation current negative (nA)	-27	-0.69	-7.2	-0.19	-0.2

Table 3.1: Five independent CdS/p-Si nanowire axial heterojunctions exhibiting the saturation effect all having varying sizes and values of currents.

Over this work I fabricated and thoroughly tested 5 distinct CdS/p-Si nanowire junctions. All of them exhibited the regarded saturation effects with notably varying parameters, as depicted in Table 3.1. The results imply that the saturation effects are natural and highly reproducible during *in situ* TEM.

3.4 Conclusions

To sum up, an original *in situ* HRTEM technique to construct individual axial nanowire junctions (perfectly emphasizing the modern *nanoarchitectonics* concept) has been developed for the first time. *In situ* HRTEM and in-parallel structural characterizations and optoelectronic tests highlight the photosensing properties of the single-crystalline axial CdS/p-Si nanowire junctions. They exhibit good selectivity toward the light frequencies higher than those of the yellow range. The junctions possess a specific photocurrent saturation effect; this can be employed in low-consumption light intensity sensing and integrated tunable voltage-driven applications owing to the effects of current limitations and excellent tolerance toward possibly unreliable and unstable bias.

The developed nanoarchitectonics-based approach employing *in situ* structural design and measurements gives a strong motivation for setting new operational principles of single crystalline nano-devices. Moreover, it is also envisaged that the near-field scanning technique can be also integrated for the constructed system for even better uncovering the exciting nanoscale optoelectronic phenomena.[27, 108].

4

In situ TEM Electrical Probing for Ultrastable Sodium Ion Batteries

Sodium-ion batteries (SIBs), as an important alternative for future energy storage, have been on stage since 1980s. Among many anode materials, elemental phosphorus (P) has attracted most of the interest in recent years because of large theoretical capacity, i.e. 2596 mAh/g. The prime disadvantage, however, of a P anode is its poor conductivity and fast structural degradation due to volume expansion, as much as >490%, over working cycles. To address this issue, I redesigned the anode structure *via* fabricating a flexible paper made of amorphous P and N-doped graphene. The as-fabricated anode delivers ultrastable characteristics and superb rate capability, 809 mAh/g at 1500 mA/g. The extraordinary structural integrity of this new anode was then studied *via in situ* experiments inside a high-resolution transmission electron microscope (HRTEM), thereby the cyclic dynamics and sodiation/desodiation mechanisms were thoroughly understood. To confirm my experimental results, Density Functional Theory (DFT) calculations were additionally performed to indeed confirm that the N-doped graphene contributes to an increase in capacity for Na storage, and to an improved anode rate performance.

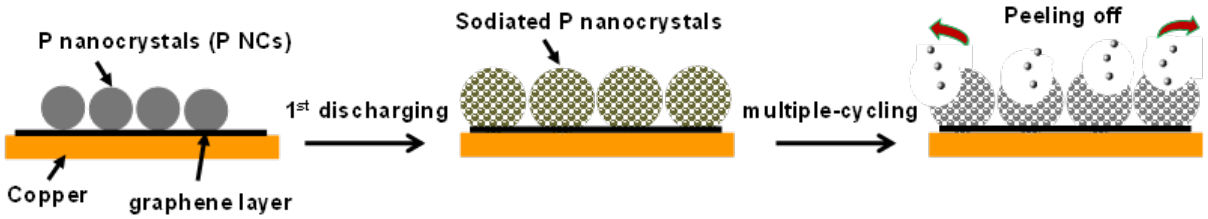

Figure 4.1: Schematic diagram of the structural fracture of a high-volume-change type P anode, in which P nanocrystals anchored on the graphene layer are placed on the surface of a Cu current collector. After 1st discharging, there is a large volumetric expansion (>200-500%) for P NCs; during cycling, such large volume change will lead to the pulverization and thus peeling off the electrode.

4.1 Introduction

Sodium ion batteries (SIBs) are receiving considerable attention and have bright expectations as one of the most promising alternatives to lithium ion batteries (LIBs) for energy storage.[49, 60, 75, 79, 96, 105, 106, 118, 119] Both battery types possess analogous chemistry, but SIBs are cheaper because of more abundant sodium natural resources. In the recent reports, the cathode performance in SIBs was found to be comparable with that of the LIBs.[4, 85] However, the performance is still not good enough for the immediate practical applications. There have been an increasing interest in developing high-power and high-capacity anode materials for the next generation SIBs,[5, 8, 35, 66, 67, 71, 73, 95, 103, 111, 120, 128] such as transition metal oxides[5, 120, 128], Prussian blue analogues[73, 95], hard carbon materials[35], nanowires[8], graphene[103, 105], tin composite[111] and antimony-based materials[71], but their specific capacities are still not competitive for future applications(<800 mAh/g).

Among the hottest materials, elemental phosphorus (P) is one of the most attractive candidates with an ultra-high theoretical capacity of 2596 mAh/g*,[33, 45, 72] i.e. about seven times higher than that of the commercial graphite anode in LIBs. The key challenge associated with a phosphorus anode is its rapid structural degradation caused by huge volume change (>490%) under cycling. For conventional crystalline phosphorus (Figure 4.1), upon Na insertion, the P crystals are pulverized and thus the electrode film surface cracks (as a result of 200-500% volumetric expansion), leading to phosphorus peeling off from the current collector, which, in turn, gives a significant performance fading. So, stabilizing or sustaining the rigidness of the phosphorus anode structure during cycling is the practical key toward the improvement of the cycling performance of a P-based SIB anode. Very recently, notable breakthroughs have been witnessed in stabilizing anode structure through a design of amorphous P/carbon hybrids.[33, 45, 72] For example, Qian et al. reported that the amorphous P/C hybrids prepared under high-energy mechanical milling had demonstrated a considerable capacity retention of 68% after

*All capacities mentioned though the thesis are calculated based on the weight of composites.

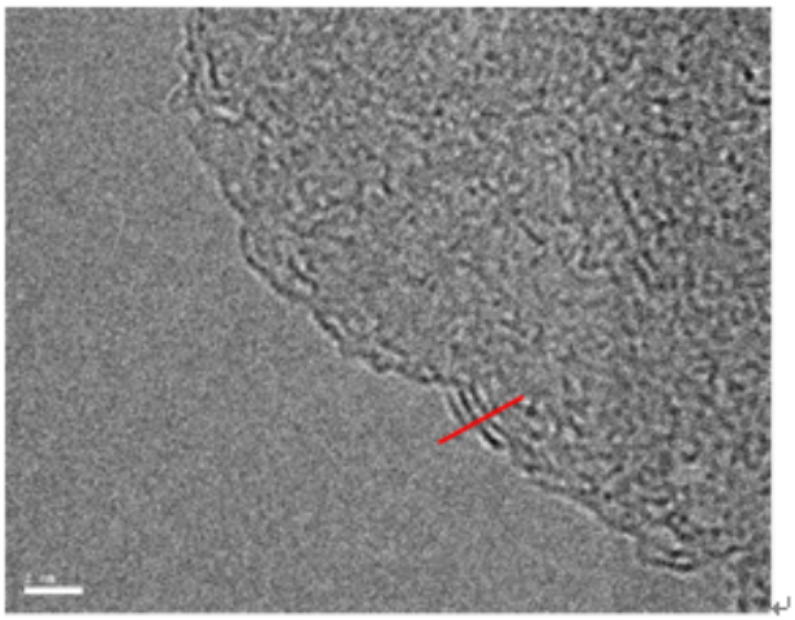

Figure 4.2: HRTEM image of an N-doped graphene (GN).

60 cycles at the current density of 250 mA/g.[72] Kim et al. demonstrated that a similar amorphous P/C structure is able to deliver as high as 80% reversible capacity and less than 7% capacity fading after 30 cycles at a current density of 143 mA/g.[33] In addition, Chou et al. fabricated a composite anode *via* simple hand-grinding of commercial microsized red phosphorus and carbon nanotubes (CNTs); this demonstrated a high capacity retention of 76.6% over 10 cycles.[45] The improvements in cycling stability in the regarded reports were indeed remarkable, however, capacity retentions of less than 80% still indicate that further developments are still needed in order to meet the practical requirements.[54]

To obtain a stable P-based Na-ion battery anode having high capacity retention and rate performance, a flexible hybrid amorphous P-embedded N-doped graphene paper was designed and studied in my work. Unlike the standard methods, which assemble the P and C components by any mechanical mixing (milling or grinding), a smarter design should tackle the existing problems, such as electrode chemical stability during sodiation-desodiation and mechanical robustness after hybridization. Therefore, a few-layered N-doped graphene (GN) (Figure 4.2) is herein selected as a substrate, whose two-dimensional (2D) nanosheet architecture provides a decent framework ensuring uniform deposition of amorphous P.[28, 61] Several advantages associated with the designed amorphous P@GN hybrids (Figure 4.3a) prepared by the developed so-called "phase-transformation" route are:

i Compared with crystalline P (Figure 4.4), amorphous P (Figure 4.9) is more stable because of its relatively small volume change.[33, 72] Through the uniform confinement of the amorphous P within GN frameworks, the flexible GN can effectively buffer the volume change. This effectively

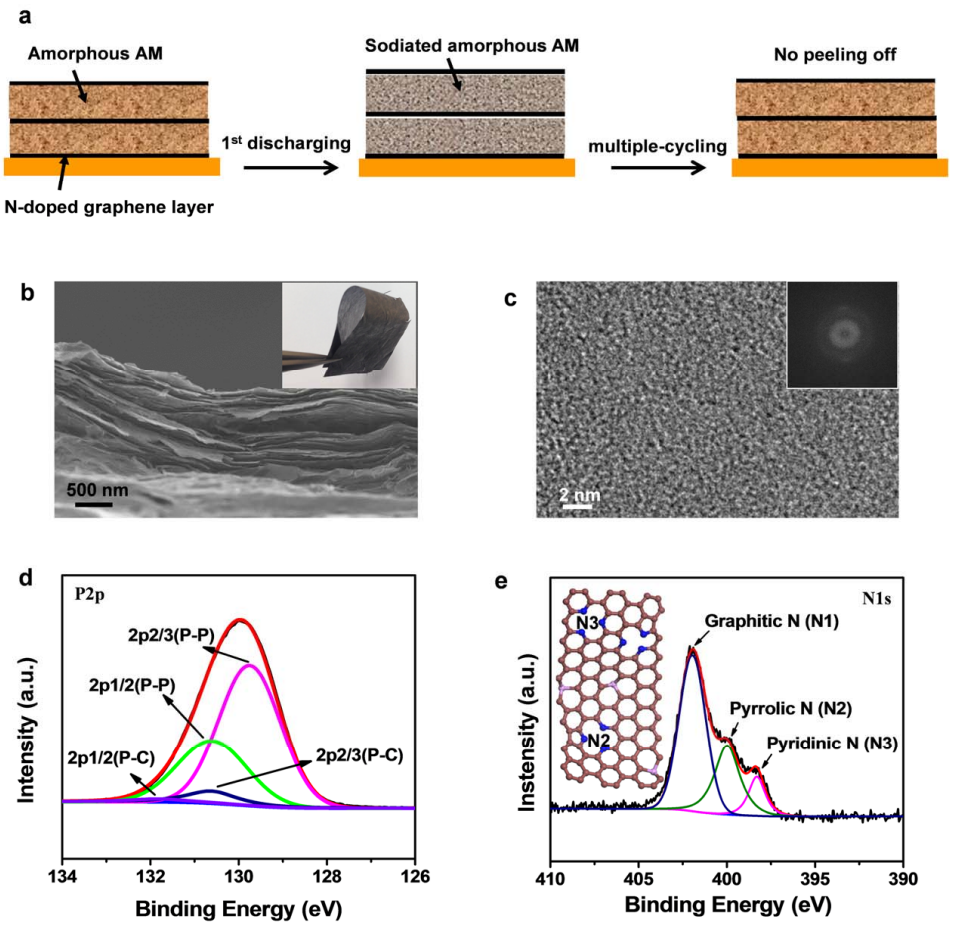

Figure 4.3: (a) Illustrative scheme of the designed layered anode structure. (b) SEM image of the cross section of a P@GN paper, the inset shows its paperlike appearance. (c) HRTEM image and the corresponding FFT pattern of the P@GN portion confirming its amorphous structure. (d-e) P2p and N1s XPS spectra of P@GN. N2 and N3 represent pyrrolic N and pyridinic N, respectively.

prevents the electrode fracture and ensures the improvement of the battery capacity retention during electrochemical cycling;

ii The possibly formed robust P-C bonds between P and GN layers anchor both components, serving like several elastic "springs" between them; this also helps to further enhance the stability of the anode;

iii The GN nanosheets provide high conductivity electron transport networks and robust mechanical backbones, so that amorphous P could be very electrochemically active. In addition, the high tenacity of GN is useful to accommodate the volumetric expansion of P without mechanical damage or peeling off effects. Furthermore, N-doped graphene also contributes with a certain capacity to the SIBs and brings the fast sodium ion transport according to the DFT calculations.

Thus in this Chapter, I show that the above-mentioned three key features of the amorphous

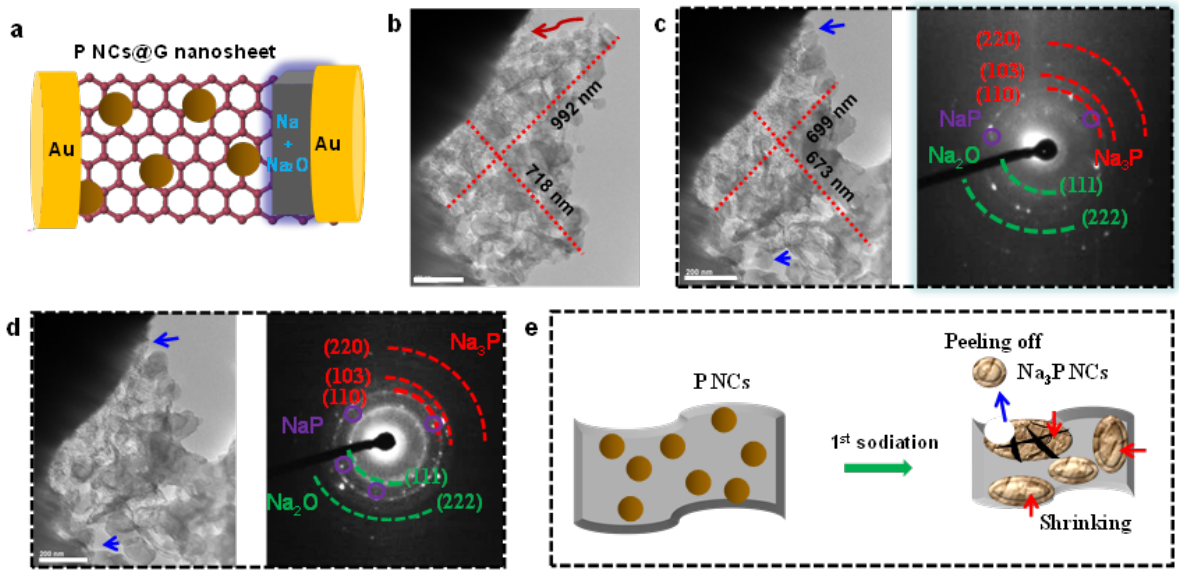

Figure 4.4: a) Schematic illustration of an individual P nanocrystals@G (P NCs@G) nanosheet prototype sodium battery device fabricated under *in situ* TEM. b) TEM image of the nano-SIB at the initial stage. c-d) Time-dependent TEM images and SAED patterns of sodiated P NCs@G nanosheet upon sodiation at 5 s and 120 s. e) The schematic illustration of the 1st sodiation-desodiation process of P@GN nanosheet. Red arrows indicate the shrinkage, while blue arrows indicate particles peeled off. Scale bars: 200 nm.

P@GN structure endows the large-volume-change anode with a superb capacity retention (>85% over 350 cycles), outstanding cycle stability (0.002% decay per cycle from 2nd to 350th cycle), and excellent rate capability (809 mAh/g at 1500 mA/g). Most importantly, state-of-the-art *in situ* probing experiments in HRTEM and supporting theoretical calculations finally uncover the key advantages of the present design and ensure the future developments of the P-based high-performance SIB anode structures, while getting deep insights into the associated atomistic mechanisms.

4.2 Experimental

Amorphous P@GN paper was prepared by a designed "phase-transformation" route. Bulk red P was heated to form P4 vapors in a sealed ampule, which were adsorbed and deposited within the inter-layers of GN; it changed back into amorphous red P after condensation.[77] Thus, a butter-bread-like structure composed of flexible conductive GN layers and thin amorphous red P layers between them was fabricated (Figure 4.3b).

Synthesis of P@GN:

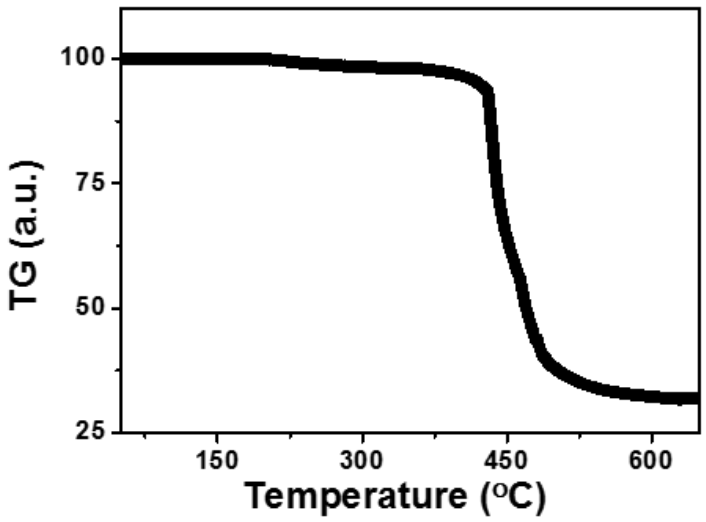

Figure 4.5: TGA curve of a P@GN sample.

Graphene oxide (GO) suspension used in this work was prepared *bia* a modified method. 50 mg of graphene oxide was loaded in a ceramic boat in a tube furnace followed by its heat treatment at 600 °C for 1.5 h in a gas mixture of NH_3 and Ar (1:2 vol/vol) under a total flow rate of 150 ml/min. Commercial red phosphorus was dispersed in water and put into a Teflon-lined stainless autoclave. The autoclave was heated to 200 °C and maintained for 12 h to remove surface oxides. As-prepared N-doped graphene (GN) products were properly mixed together with the pretreated red phosphorus powder, and sealed in an ampule in an inert Ar atmosphere. The sealed reactors were thermally treated at 500 °C for 1 h and then at 280 °C for several hrs in the furnace, before natural cooling to room temperature. The final product was washed with CS_2, water and methanol, and then dried at 60 °C.

Characterization:

TEM images were taken with a 300 kV JEOL 3000F microscope. Samples were first dispersed in ethanol and then collected using carbon-film-covered copper grids. To avoid possible electron beam effects (such as radiolysis or sputtering damage of both Na-containing species and graphene lattice) the beam intensity was minimized. Scanning electron microscopy (SEM) images were recorded on a Hitachi S4800 electron microscope operating at 15 kV. XRD patterns were taken on a Philips X Pert PRO MPD X-ray diffractometer operated at 35 kV and 45 mA with Cu Kα radiation. XPS measurements were carried out on an ESCALab220i-XL spectrometer by using a twin-anode Al Ka (1486.6 eV) X-ray source. All the spectra were calibrated to the binding energy of C 1s peak at 284.6 eV. The background pressure was 3 x 10-7 Pa. Raman spectra were collected on a Horiba Jobin-Yoon T6400 Raman spectrometer.

Electrochemical tests:

The electrochemical properties of P@GN and P NCs@G samples were studied using a 2032-type

coin cell on a Hokudo Denko Charge/Discharge apparatus. The working electrode was prepared by directly pressing a piece of sample onto the Cu mesh current collector. Na metal foil was selected as the reference and counter electrode. The electrolyte was 1 M $NaPF_6$ in ethyl carbonate (EC) and diethyl carbonate (DEC) ($EC : DEC = 1 : 1 vol/vol$). The cells were assembled in a glove box filled with a pure argon gas.

Construction of individual prototype P@GN (P NCs@G)-based SIB:

In situ TEM observations were conducted in a JEOL-3100 FEF equipped with an Omega filter and a *Nanofactory Instruments* STM-TEM holder. In order to build up the test cell, an individual P@GN or P NCs@G nanosheets were attached to the fresh-cut flattened Au wire, which was then attached to the piezo-manipulator. A small piece of Na foil was placed to another Au wire as a reference and counter electrode. Before insertion of the holder into the TEM column, a piece of Na foil covered with a Na2O layer was placed on the surface of metal Au tip. Then isolated P@GN or P NCs@G samples were chosen for direct electrochemical tests. Under the following delicate piezo-driven TEM mechanical manipulations the two electrodes were connected and the probe cell was finally constructed. The sodiation was carried out at a negative bias in the range of -2 V to 0 V with respect to the Na metal.

DFT calculations:

The first principle calculations were carried out using the Vienna ab initio simulation package (VASP),[37] where projected-augmented-wave (PAW) potential was adopted.[36] The functional of Perdew, Burke, and Ernzerhof (PBE) and the generalized gradient approximation (GGA)[69] were employed in the calculations. We used a $3 \times 3 \times 1$ mesh in the irreducible Brillouin zone for structure relaxation and $6 \times 6 \times 1$ mesh for self-consisted calculations. In all the calculations the forces were relaxed to the values lower than 0.02 eV/Å.

4.3 Results and discussions

It is considered that some P-C bonds possibly exist between amorphous P and GN layers which would tightly anchor those layers. Scanning electron microscopy characterization (Figure 4.3b) illustrates the cross section of the structure of anode, where we can see a lot disordered and flexible layered structures. It is considered that most GN sheets can not be tranfered back to graphite by restacking even under longtime heating or mechanical induced compression.[28] From HRTEM image and the corresponding fast Fourier transform (FFT) patterns, crystallography of P was uncovered: it is amorphous, as depicted in Figure 4.3c. We were able to observe the disordered nature of P@GN of structure from the diffused rings and the absence of clear lattice fringes.

The constitution of P in the composite was characteried to be 66% by thermogravimetric analysis curve as shown in Figure 4.5. In Figure 4.3d, the P2p X-ray photoelectron spectroscopy (XPS) reveals 2p1/2 and 2p3/2 doublets, where two peaks at 129.75 eV (2p3/2) and 130.6 eV (2p1/2) suggest the

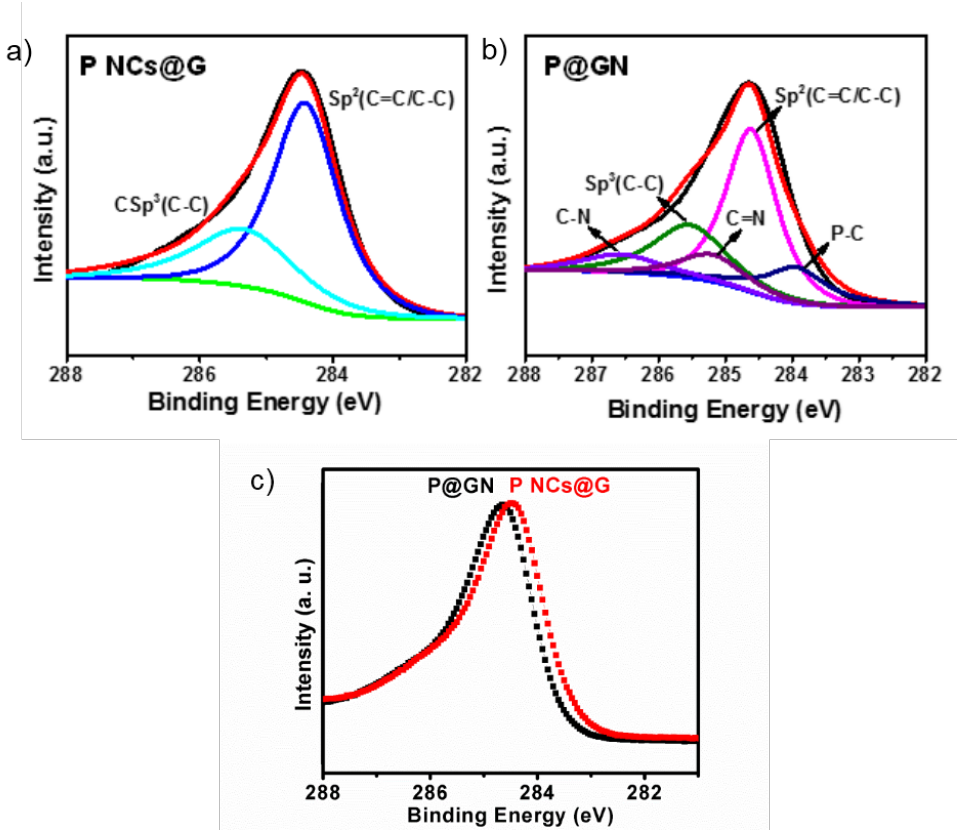

Figure 4.6: a-b) C1s XPS spectra of PNCs@G and P@GN samples. c) Overlay of the two surveys for C1s spectra of the two samples.

possible existance of P-C bonding.[31, 62, 122]

According to the theoretical simulations,[12, 85] among all P-C bonding types – sp3, sp2 in plane, sp2 at edge, and sp2 in the aromatic ring – the most stable one is the sp2 hybridized P-C bonds in aromatic ring because of bond length in the "π-p* conjugation plane is the shortest. As the inset image illustrates in Figure 4.3e, GN would provide sp2 P-C bond at the edge and/or at the aromatic rings.

In addition, another evidence from C1s XPS spectra, as shown in Figure 4.6, depicts the possibly existing P-C bonds in P@GN. In order to get clear comparison, P nanocrystlas in pure graphene sample (this sample name will be called as P NCs@G) was also prepared for test. As shown in Figure 4.6a, clearly, there are no P-C bonds found in P NCs@G.

As compared with the sample set of P NCs@G, the sp2 carbon atom fraction decreases while sp3 C-C (285.3 eV) bonds prevail in P@GN (Figure 4.6b) possibly due to some defects caused by nitrogen doping. Three N-doping types are found to exist in P@GN (Figure 4.3e): graphitic, quaternary N (N1, 401.7 eV), pyrrolic N (N2, 400.2 eV), and pyridinic N (N3, 399.1 eV).[77, 98, 101, 102] The N2 and N3 dopants are generally thought to be located at the edges or surface defect sites such as vacancies.

The specially designed layere structure exhibits excellent electrochemical performances. In Figure

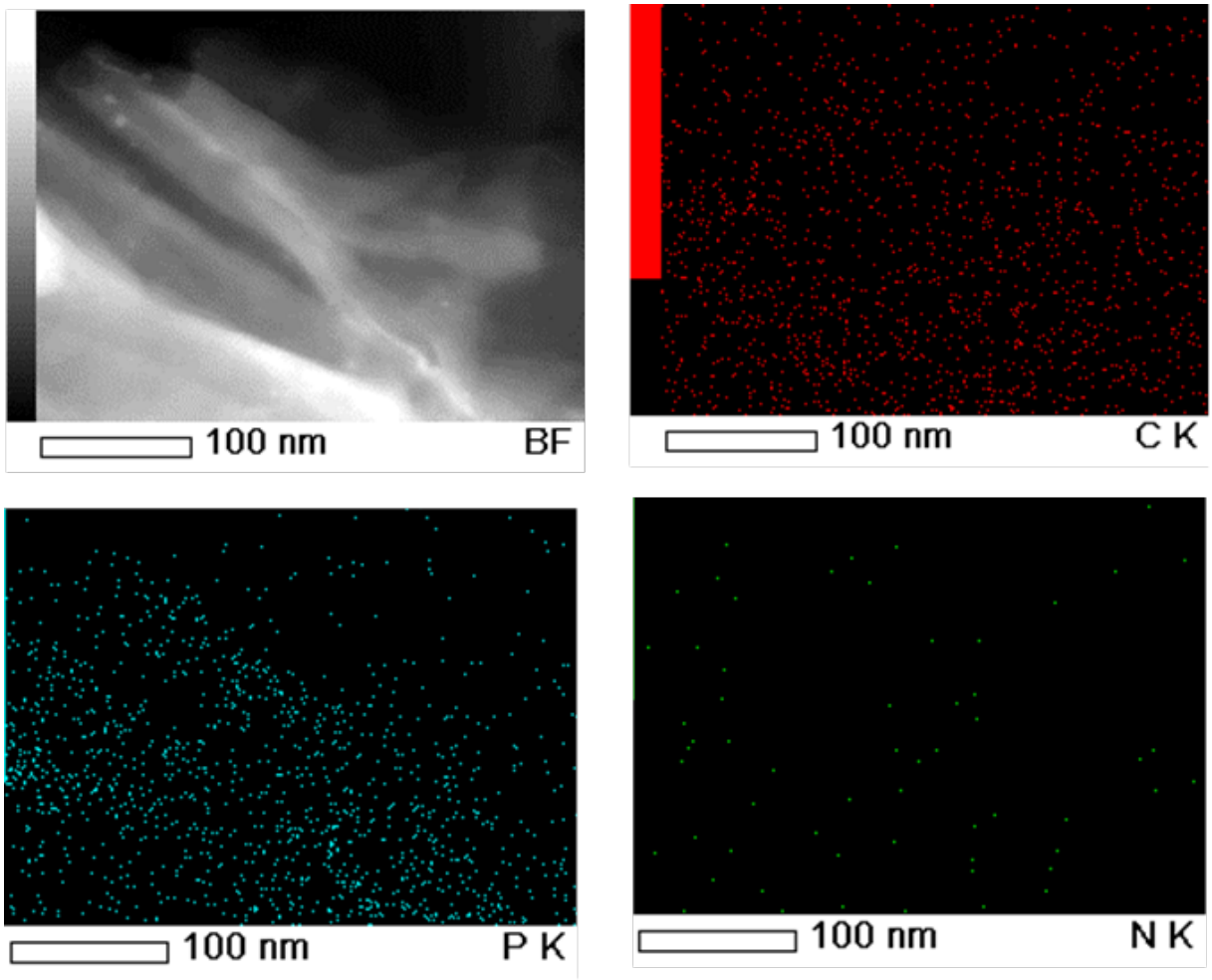

Figure 4.7: HAADF-STEM image, and C-, P- and N-elemental maps of a P@GN nanosheet.

4.9, the battery performances of the P@GN were evaluated by using standard CR2032 coin cells.

As a comparison sample set, red P nanocrystals (NCs) placed on pure graphene (P NCs@G) were also manufactured by grinding of nanoscale red phosphorus and graphene. As shown in Figure 4.9a, the initial Coulombic efficiency of P@GN is 87%, higher than that of 85% for a reported P@C hybrid electrode.[45] From the 2nd to 120th cycles at 200 mA/g or 350th cycle at 800 mA/g, the Coulombic efficiencies are more than 98%. A discharge plateau, as depicted in Figure 4.9b, corresponds to an anodic peak spreads from 0 V to 0.5 V, implying the formation of Na_3P with a theoretical capacity of 2596 mAh/g. The conversion chemical reaction from P to Na_3P takes place. The chemical reaction process is then eventually proved by *in situ* HRTEM experiments which will be discussed in the following paragraphs. In a reversed scan, a main anodic peak appears at 0.53 V, which possibly matches the main sodium ion de-intercalation process *via* chemical reaction from Na_3P to P. However, no clear peaks at any other potentials (for instance 0.63 V assigned to NaP) were found. This indicates that this electrode probably experiences a reversible discharging/charging chemical cycling between Na_3P and P and affords very high capacity because of existence of Na_3P.

Over 350 battery cycles, the capacity retention of P@GN battery is more than 85%. From the 2nd to 350th cycle at 200 mA/g, the capacity decay is even less than 3%. The excellent capacity retention and stability (about 0.002% decay per cycle) are among the best cycling stablity performances of all reported P-based anodes to date. To reveal the mechanism of the unusual cyclic stablity, the original and after-cycled P@GN electrodes were examined by a high angular annual dark field (HAADF) imaging in a scanning TEM (STEM) mode with the EDS mapping as illustrated in Figure 4.9c, Figure 4.7 and Figure 4.8. Obviously, the integrity of the battery structure is maintained quite well in the desodiated states after even 120 cycles.

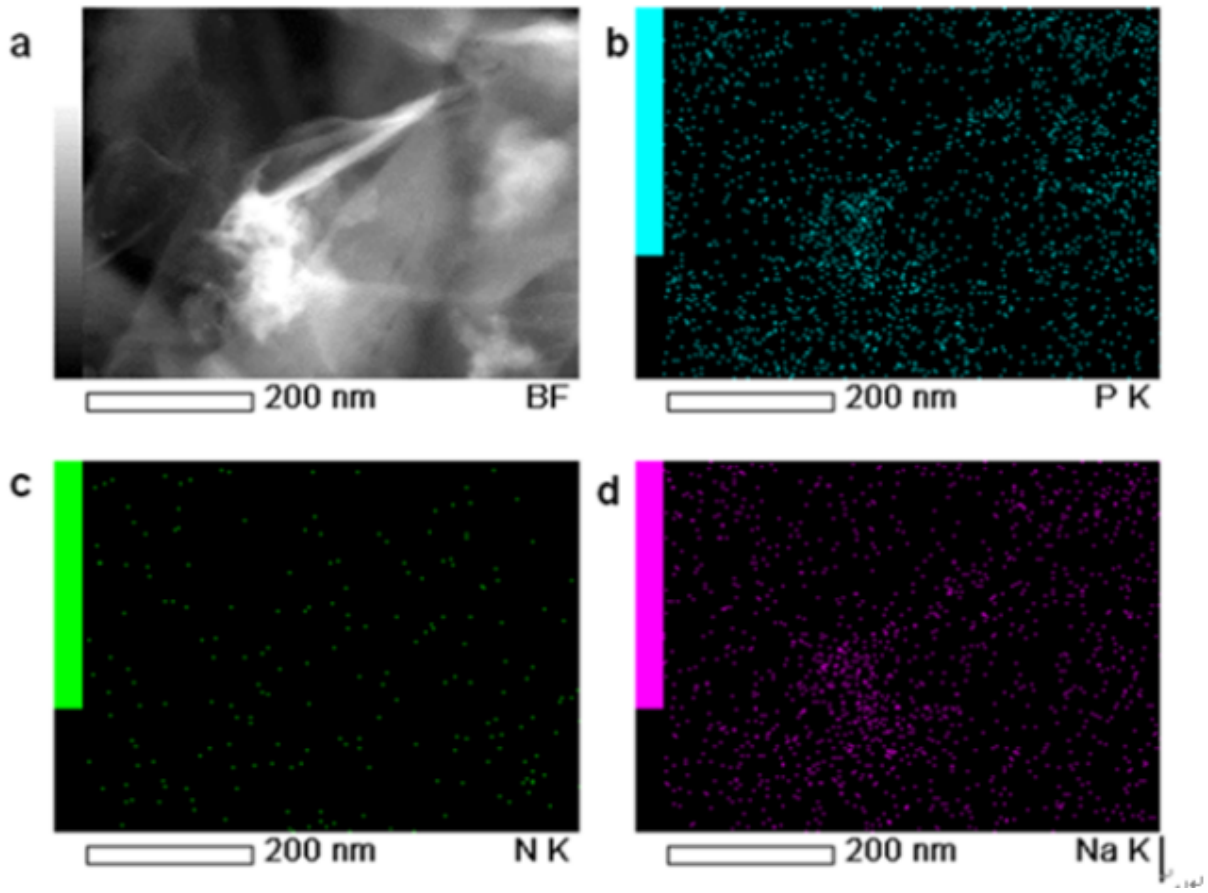

Figure 4.8: The HAADF-STEM image and the corresponding elemental maps of a P@GN nanosheet at the fully desodiated state after 150 cycles.

It is also noted that upon sodiation, distribution of sodium species is very homogeneous over the nanosheet (Figure 4.9c), this suggests the successful intercalation of sodium ions. The reduced volume expansion of P layers are significantly buffered and confined by GN layers, which is the key for preventing failure of the anode structure. Moreover, P@GN anode material exhibits improved rate capability as compared with P NCs@G material, as marked in Figure 4.9d. At a high current rate (1500 mA/g),

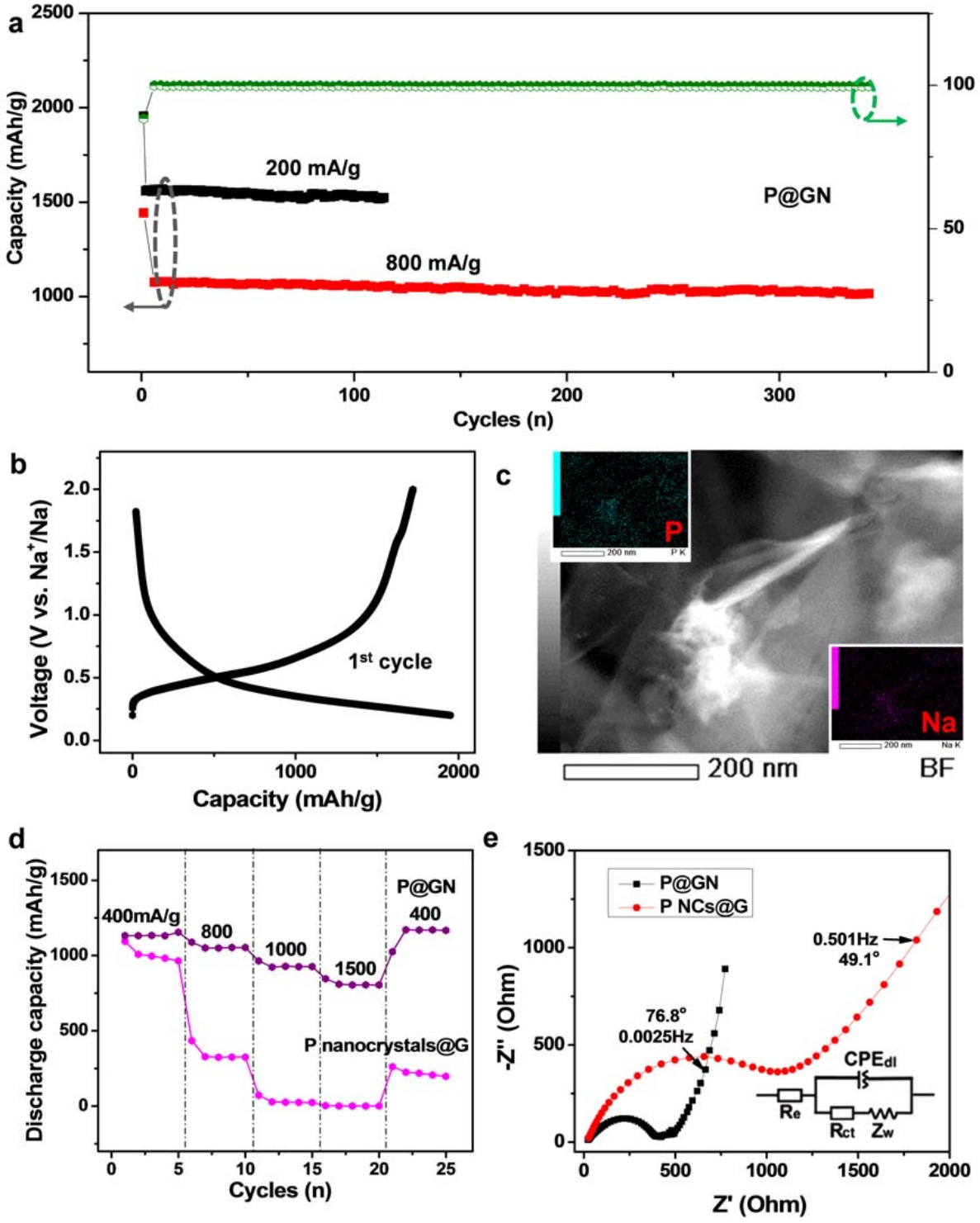

Figure 4.9: (a) Cyclic capacity and Coulombic efficiency of P@GN at 200 mA/g and 800 mA/g. (b) Galvanostatic charge and discharge profile of P@GN anode at 200 mA/g. (c) The HAADF-STEM image and the corresponding EDS maps of a P@GN nanosheet at the desodiated state (after 120 cycles). (d) Rate capabilities of P@GN and P NCs@G. (e) Nyquist plots and equivalent circuit model of P@GN and P NCs@G electrodes after 10 cycles at 0.1 A/g in the discharged state.

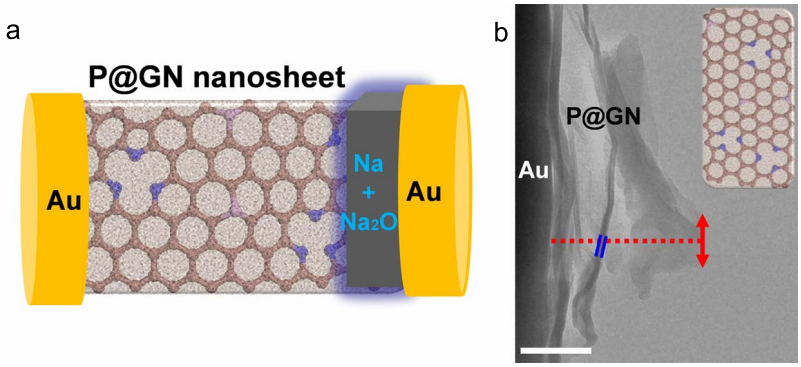

Figure 4.10: (a) Schematics of an individual P@GN nanosheet sodium ion battery device test performed by *in situ* TEM. (b) TEM image of the SIB at the initial stage. Scale bar: 100 nm.

the reversible capacity still reaches 809 mAh/g for P@GN. This capacity is twice higher than that of the theoretical capacity of the commercial graphite (370 mAh/g) in LIBs. And, of course, these results are far better than those of the P NCs@G (10 mAh/g at 1500 mA/g).

This is especially meaningful for future secondary battery choice. In fact, sodium-ion batteries are expected to be of low cost and high capacity.

To compare the battery anode kinetics of P@GN and P NCs@G, their electrochemical impedance spectroscopy (EIS) was performed as ploted in Figure 4.9e. The Nyquist curves demonstrate that a diameter of the semicircle for P@GN anode material in high-medium frequency region is much smaller than that of P NCs@G electrode. This suggests that P@GN anode possesses a lower contact and better charge-transfer impedance. Based on the modified Randles equivalent circuit, shown in the inset of Figure 4.9e, the P@GN anode exhibits a significant lower charge-transfer resistance. Therefore, P@GN holds a high electrical conductance and also provides more stable surfaces such as SEI layer. This leads to the better rate capability and reversible capacity as comparison with P NCs@G. In addition, the angle of low-frequency slope for P@GN (76.8 degrees) is steeper than that of P NCs@G (49.1 degrees), indicating higher diffusivity of Na^+ for sodium ion uptake and extraction in P@GN anode due to the steep low-frequency tail.[85]

It is very important to maintain the structural integrity during cycling to realize stable performance for large capacity and low-cost anode material.[49] To analyze a mechanism of the anode stability of our ultra-stable decice, I performed an *in situ* TEM study of the chemical and structural changes of the as-fabricated anode during electrochemical cycling (Figure 4.10). The *in situ* TEM experimental set-up is very similar to some previous reports (Figure 4.10a).[100, 102]

The setup mainly consists of two parts: the sample is placed on a gold wire tip, while another gold wire with a small piece of sodium is put on the opposite side. Special care is required for sodium loading. Sodium is loaded to the probe (which is on the TEM holder) in glovebox filled with argon. Then the holder was capped under argon atmosphere. A few seconds before insertion of holder, the cap was

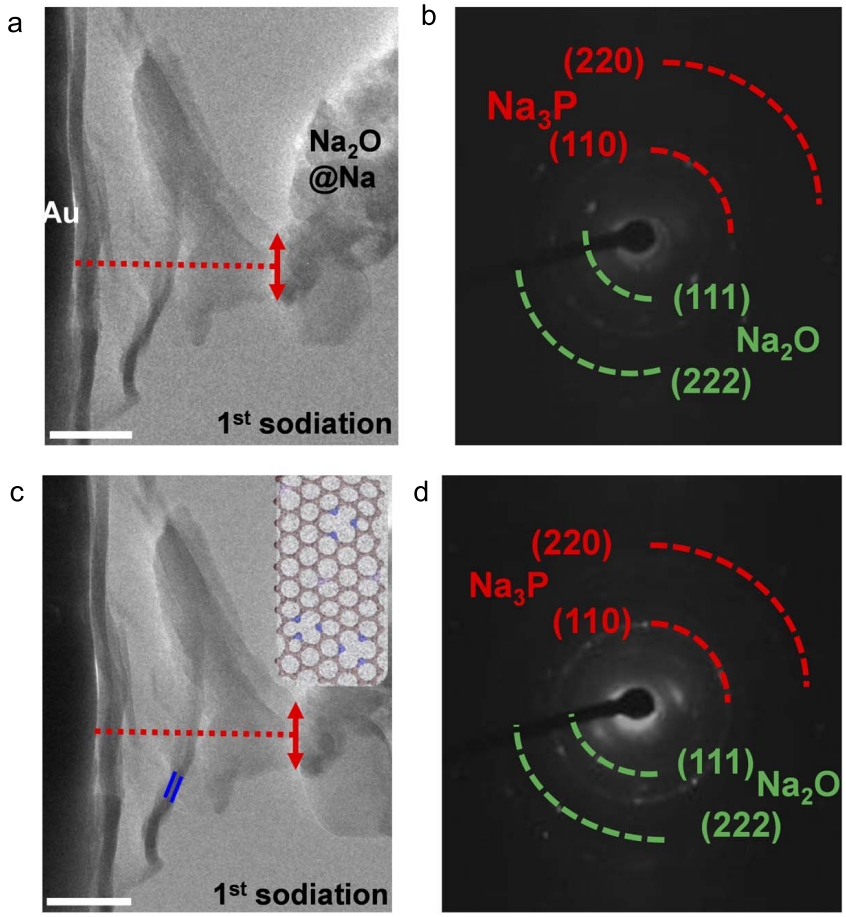

Figure 4.11: TEM image and SAED pattersn of the *in situ* SIB at (a) 15 s and (b) 120 s of sodiation during first discharging. Scale bars: 100 nm.

removed. During transferring process, a very thin layer of Na_2O was formed on the sodium metal surfaces. The Na_2O layer serves as a natural solid electrolyte for the single nanostructured SIB. Figure 4.10b depicts a TEM image of a freestanding P@GN nanosheet material.

Figure 4.11 presents the sodiation process of an individual P@GN anode. A -2 V potential was applied to P@GN anode with respect to the sodium potential. The anode material immediately expanded in both longitudinal and transverse directions after applying the bias, as shown in Figures 4.11. After sodiation, the length of nanosheet increased from initial 210 nm to the sodiated 250 nm, and the length of a regional edge enlarged to 83 nm from the previous 65 nm. The experiment further implies that an effective Na transport along/across the hybrid structure indeed took place.

It is noted that the expansion rate in the one direction, from 210 nm to 250 nm, becomes less than that for another one, from 65 nm to 83 nm. This might indicate that small-sized nanoribbons could possess higher electrochemical activities. No significant evidence of structural degradation was found even after the entire sodiation (Figure 4.11b). This is confirmed by the decent flexibility of GN and amorphous

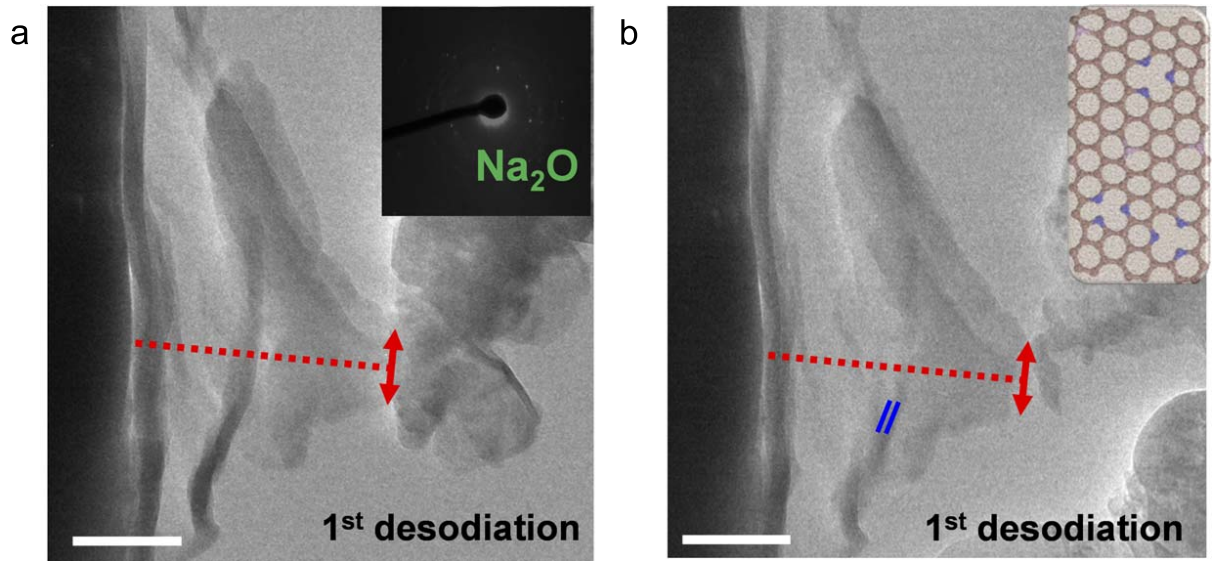

Figure 4.12: (a) 5 s and (b) 120 s of time-dependent TEM images of desodiation during 1st charging. Inset in (b) shows the corresponding schematic atomic structure. The inset in (a) depicts the corresponding SAED pattern. Scale bars: 100 nm.

P layer which can effectively buffer the large volume expansions during insertion of sodium ions. The nanosheet thickness also increased from 10 nm to 14 nm, as it is marked by blue color in Figures 3b and 3d during discharge process. The SAED pattern of the sodiated P@GN (Figure 4.11) reveals the crystallography information after phase changes after sodiation. The main phase of the sodiated anode material is identified to be Na_3P – which takes more sodium ions than NaP per single P atom. This result is consistent with the battery test shown in Figure 4.9b.

The desodiation process took place when a 2 V bias was applied to the nanostructure. As presented in Figure 4.12, the volume shrinkage became observable along both the longitudinal and transverse directions. It is observed that desodiated nanosheet after sodium extraction looks quite similar to the initial status. What is more, the edge segment perfectly kept the initial state. The experiment demonstrates that the designed layered structure is able to buffer the anode volume expansion and shrinkage during electrochemical cycling. Therefore, the *in situ* experiments explain the stable cycling performance as revealed by the *ex situ* battery measurements (Figure 4.9b). Integrity of the P@GN nanosheet is preserved quite well, suggesting that the butter-bread-like structure is effective for relaxing the strain and overcoming pulverization caused by volume expansion, and, hence, it can be a very promising anode candidate for SIB.

The comparison material, an individual P NCs@G nanosheet, was also build and tested by *in situ* microscopy. As shown in Figure 4.4, during discharging, P nanocrystals expanded immediately. The whole P NCs@G nanosheet drastically shrinks instead of expanding upon sodium insertion along all directions, because the sodiated crystals aggregated together and also their size grew larger under the

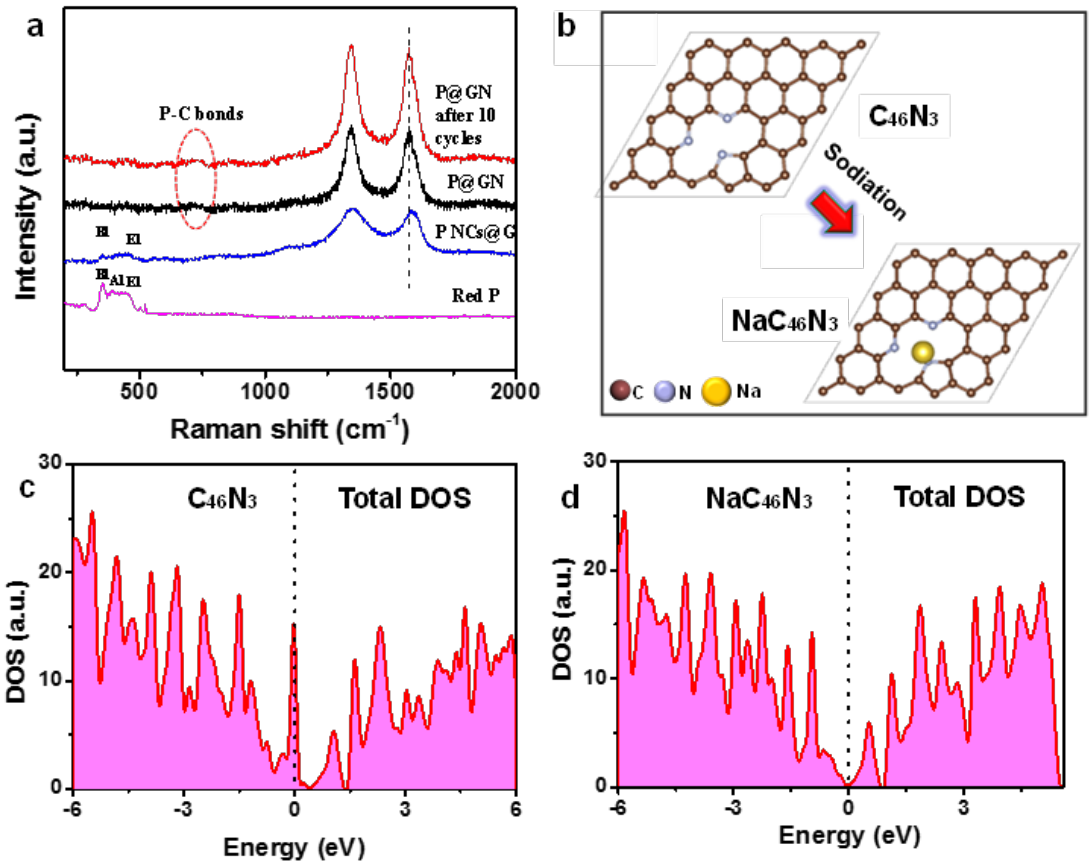

Figure 4.13: (a) Raman spectra of red P, P NCs@G, and P@GN before and after sodiation. (b) The schematics of the insertion of sodium into a $C_{46}N_3$ sheet based on DFT calculations. (c-d) DOS of $C_{46}N_3$ and its sodiated product $NaC_{46}N_3$.

Ostwald ripening.

Therefore, the strong adhesive forces between graphene and P NCs compressed the whole structure into an aggregate form of P NCs. Note that the phenomenon is more significant at the edges, as compared with the basal plane due to their higher electrochemical activities. Moreover, peeling off of an active material can also be observed during *in situ* TEM processing which is marked by blue arrows in Figure 4.4c-d. Two particles in the upper part and another nanocrystal in the lower part disappeared after sodiation. The peeling off of active material implies that the P NCs@G experienced significant expansion, which leads to the irreversible peeling off, and hence, caused a loss of capacity. It is noted that some NaP phases are seen in SAED patterns in Figures 4.11, for the desodiated material. The NaP phase (instead of Na_3P) implies that only conversion of P into NaP rather than into Na_3P took place. It is know that Na_3P holds much higher capacity, 2569 mAh/g, than NaP, which is only 856 mAh/gh. Sodiation of phosphorus in P NCs@G sample can be associated with its low electrical conductivity and large crystal size. Therfore, the irreversible structural failure and the presence of NaP (instead of N_3P)

undoubtedly limit the performance for P NCs@G. The *in situ* experiment condlusion is consistent with the battery cycling performance and rate properties (Figure 4.9c).

It is believed that maintaining amorphous morphology of P during cycling is a key factor for ultra-stable battery performance. This is confirmed by the Raman spectroscopy presented in Figure 4.13a. Spectrum features of red P between $300 - 500cm^{-1}$ can be attributed to P–P stretching bonds of P_9 and P_7 cages while establishing the pentagonal tubes in paired layers.

Compared with red P material, the amorphous phosphorus and nitrogen doped graphene hybrid structure does not display Raman peaks natural for P, but shows two typical D-band and G-band peaks (peculiar to graphene).[33] The result indicates that the layerd P@GN paper was well maintained during cycling. Additionally, Raman spectra of various samples provide more evidences for the existence of the stable P-C bonds after multiple cycles. In Figure 4.13a, a broad envelope centered at about $700cm^{-}1$ for P@GN, which is marked by red circle, could be attributed to P-C bond stretching modes. Therefore, stable P-C bonds may exist after cycling, as shown in Figure 4.13a.

Last but not least, DFT simulations were performed to uncover the function of N-doped graphene for battery performance of SIB. Some previous works used doped graphenes for LIB and SIB anode materials.[98, 102, 103, 105, 118] First, the adsorption energy of sodium ions on different graphene structures were calculated. For graphene and N1 graphene, the value is positive, at around +0.50 eV. This means that both graphene and N1 graphene are unfavorable for sodium absorption, and, hence, they deliver no capacity to the battery. For N2 and N3 doped graphene and P doping, the absorption energy turns to be negative. The negative energy value means that the material is attractive for sodium absorption. The corresponding sodium absorption energy on GN surfaces are illustrated in Figure 4.13b. Then, the corresponding capacities based on the simulation of the maximum sodium concentration were calculated. It is acknowledged that graphene is not conductive, and hence the theoretical capacity is exactly zero. $C_{46}N_3$ holds a 0.851 e charge transfer, and capacity of 373.3 mAh/g. This value is 1.2 times of the capacity of hard carbon at 300 mAh/g, suggesting that N and P doped graphenes are decent candidates for modern anode materials due to their positive roles in the electron transport.

All three kinds of doped graphenes show a large charge transfer from sodium. For instance, sodium donates 0.853 e charge to $C_{46}N_3$. It implies that doping sites could provide the high efficiency to improve the interactions between sodium and G surface for future sodium ion storage. The high rate capability of the N-doped graphene is also supported by the density of states simulations, as shown in Figure 4.13c-d, N doping makes $C_{46}N_3$ metallic. As a consequence, theoretically, N doped graphene is favorable for electron and ion transfer, high rate capability, decent capacity, and long battery lifetime for SIB.

4.4 Conclusions

To sum up, I applied a phase-transformation approach to fabricate nitrogen doped graphene-phosphorus structure with layered morphologies where thin amorphous phosphorus layers are formed within flexible and electrically conductive N-doped graphene structures. Advantages of the designed anode material have been studied using various characterization techniques, device tests, *in situ* microscopy and theoretical calculations. These advantages are namely:

(1) Thin P layer on the doped graphene (instead of crystalline P) anode shows ultrastable efficiency of 0.002% decay per cycle and good rate capability of 809 mAh/g at 1500 mA/g;

(2) P-C stable bonds may exist to bond GN and P layers;

(3) *In situ* HRTEM experiments verified and revealed the reason of the materials' ultrastable performance.

5

Opto-Mechano-Electrical Tripling in Zinc Oxide Nanowires Probed by *In situ* Photocurrent Spectroscopy in TEM

For future flexible optoelectronics, three important factors must be considered: light, force and electricity. Thus, photosensing spectroscopy of free-standing Zinc Oxide (ZnO) nanowires in a high-resolution transmission electron microscope (TEM) is studied herein. By applying the optical *in situ* TEM system described in Chapter 2, novel opto-mechano-electrical tripling phenomenon in Zinc Oxide nanowires is discovered. Interestingly, splitting of photocurrent spectra at 3.3 eV under *in situ* TEM bending of Zinc Oxide nanowires directly corresponds to the nanowire deformation. It is established that such effect is caused by the expanded and compressed nanowire sides, especially at the nanowire edges. Theoretical calculations of deformed Zinc Oxide nanowire bend structure changes has a perfect agreement with the *in situ* experimental data. The splitting of photocurrent spectra can be understood in terms of changes in the valence band structure of Zinc Oxide nanowires because of the lattice strain. The deformation-induced splitting gives a valuable information for flexible optoelectronics and piezo-phototronics when using nanowire building blocks.

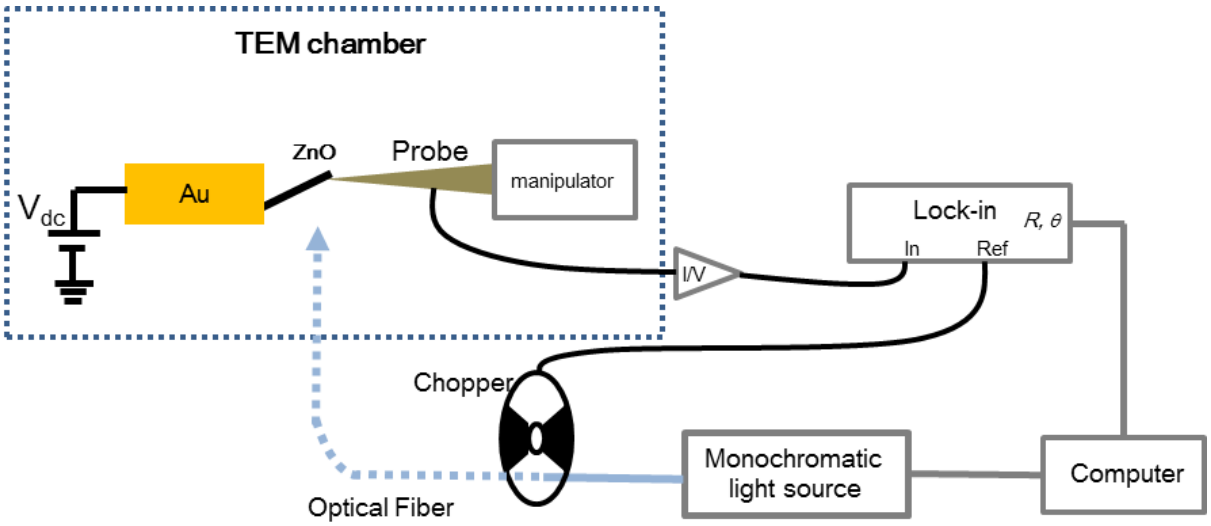

Figure 5.1: Scheme of experimental setup inside and outside of a high-resolution TEM for the ZnO nanowire testing.

5.1 Introduction

These years, transmitting information at a wide band width, long distance, ultra-high speed and low power consumption relies on photons passing through optical fibers, instead of using electrons in electrical wires.

However, the industries and consumers are still not satisfied with the current status of integrations of optoelectronic components within rigid or flexible substrates.[32, 48, 74] To achieve highly efficient integrations with multi-functionalities, the sizes of light sources (including laser diodes and light emitting diodes), modulators, resonators, waveguides, photodetectors in optoelectronic systems or even additional strain sensors, accelerometers etc. in Micro-Opto-Electro-Mechanical Systems are expected to be downsized to the nanoscale.[68] To catch up with the currently mature silicon microelectronics industries, the light-matter interactions in novel optoelectronic semiconducting materials should be carefully studied, especially with respect to using them as individual building blocks for bottom-up optoelectronic technology. However, conventional approaches are not able to detect, operate and modify optoelectronic property/functions of a single nanomaterial directly and at the high spatial resolution.

In addition, flexible and stretchable electronics and optoelectronics attract prime attention of general consumers nowadays. Nanowires, as one of the most promising building blocks for bottom-up flexible optoelectronics, have not been yet comprehensively studied at a level of a single free-standing material. A zinc oxide nanowire is one of the most promising and hot 1-D materials for opto-mechano-electrical applications because of its ideal piezo-phototronic properties.[104, 112, 115, 116] Many published reports on flexible nanowire photodetectors have relied on various substrates.[25, 99, 110] Obviously, choosing a right substrate is always an essential factor in flexible optoelectronics; that is, the physi-

cal properties of a nanostructure are strongly affected by the substrates. For instance, it has been reported that the optical absorption coefficient, the band-edge and near-band-edge (NBE) characteristics of zinc oxide films are very much dependent on the substrate type/quality and its treatments.[83] Consequently it is very important to characterize mechano-optoelectronic properties of zinc oxide nanostructures in free-standing conditions and in high vacuum. For example, Ohno et al. studied photoluminescence (PL) and cathodoluminescence (CL) spectra of a piece of the diamond crystal in TEM;[64] Yang et al. measured photocurrent values of deformed zinc oxide nanowires in TEM after their illumination by light with fixed wavelength.[117] However, the wide-band-range photocurrent spectroscopy of free-standing zinc oxide nanowires or any other nanomaterials has not been researched as yet. In this Chapter, I investigate the photocurrent spectroscopy of individual free-standing zinc oxide nanowires by means of *in situ* probing optical-STM-TEM. It is discovered that the photocurrent spectra of zinc oxide nanowires experience a specific splitting. Additionally, the splitting values exactly correlate with the elastic strains applied. Under relevant theoretical calculations, the valence band structure is found to change accordingly on two sides of the bent nanowire. The calculations nicely fitted and matched the experimental results.

5.2 Experimental

Zinc oxide nanowires were prepared through a chemical vapor deposition (CVD) method similar to that in previous reported publications.[112] *In situ* characterizations and manipulations were performed by the optimized *Nanofactory Instruments AB* opto-TEM-STM sample holder with a nanomanipulator and an optical fiber, as detailed in Chapter 2, in a 300 kV JEOL-3100FEF (Omega filter) high-resolution microscope. Zinc oxide nanowires were carefully placed onto the gold wire stage of the holder tip-frame by using the minimum amount of silver epoxy. Then, inside TEM, the electrochemically etched tungsten probe was moved to contact a chosen individual nanowire by controlling the piezo-nanomanipulator movements. Also, the optical fiber was manipulated to illuminate the specimen in tandem with its probing. The experimental configuration is schematically shown in Figure 5.1. By controlling the tungsten probe, deformation of nanowires was delicately carried out. The photocurrent was then tested by applying a voltage between the two ends of a zinc oxide nanowire. While, with the aid of the monochromator, scanning of the light wavelength from 2.5 eV to 4.5 eV, and recording the photocurrent spectrum were performed. By applying a lock-in amplifier, photocurrent response was rectified according to the chopper frequency in order to resolve the weak signals from the noise background.

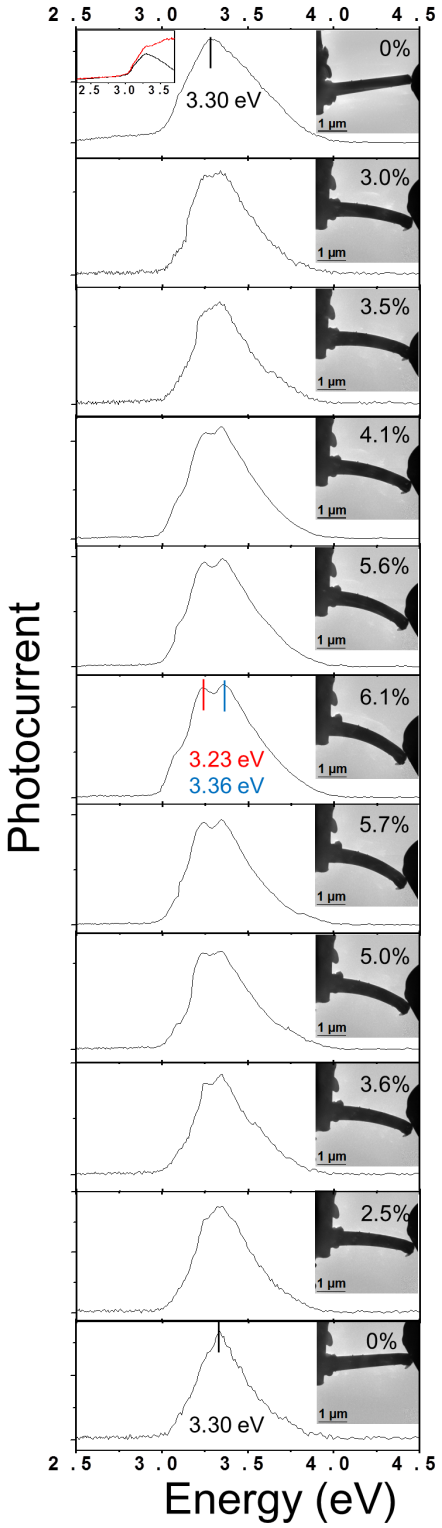

Figure 5.2: Photocurrent spectra (raw data) recorded under bending deformations from 0% to 6.1%, and back to 0%. Red line in the upper left inset of the first panel depicts the normalized (to the incident photons) spectrum at a zero strain (normalized from the measured photocurrents shown as the black line in the inset).

5.3 Results and discussions

In Figure 5.2, an experimental run on a given zinc oxide nanowire is shown. The nanowire was initially straight, as illustrated in the uppermost panel of Figure 5.2. Please note that the normalized spectrum to the incident photons at the zero strain state was calculated and is shown in the inset. Due to the large exciton binding energy at 60 meV for ZnO, a strong exciton absorption peak is seen even at room temperature. The nanowire was probed under its bending in the horizontal plane. Photocurrent-wavelength raw spectra in Figure 5.2 demonstrate the specific splitting phenomenon which is apparently related to the strain in the deformed nanowire. The nanowire diameter was measured to be 385 nm. The strain, was calculated as follows *:

$$\varepsilon = \frac{r}{R}$$

, where r is a distance from the compressed or expanded side of the nanowire to the middle point of the compressed or expanded region and R is the radius of curvature of the deformed nanowire.

The first manipulation deformed the nanowire to 3.0% strain and then to 3.5%, 4.1%, 5.55% and 6.1% gradually. Next, the probe was carefully moved backwards. The strains then decreased to 5.66%, 5.0%, 3.6% and 2.5% gradually. Finally, the nanowire returned to its original unbent state. Before taking any photocurrent spectrum after each probing, the electron beam of the microscope was taken off and away from the sample. One side of the deformed nanowire experiences a compressive strain; the other side is under tension. The high-resolution TEM image, as shown in Figure 5.3, clearly displays the (002) lattice fringes along the c-axis, which is also the growth direction of the nanowire.[125] The local lattice distance within the compressed nanowire edge is 0.243 nm, which is smaller than the usual value of 0.260 nm of the ZnO bulk material.[9] The local lattice distance is larger away from the compressed edge, up to 0.257 nm. Once the nanowire is bent, at first, the photocurrent spectra remain a of very similar shape displaying one broad peak centered at about 3.30 eV. Once the strain is increased under further *in situ* bending, the pristine broad peak splits into two components. Upon a 3.0% strain, the separated two peaks are centered at 3.24 eV and 3.34 eV. Therefore the corresponding red-shift and blue-shift are 0.06 eV and 0.04 eV, respectively. Upon the largest strain applied at 6.1%, the red-shift becomes larger, about 0.07 eV, while the blue shift is 0.06 eV. The splitting values are determined by the gap between the centers of the two peaks of the photocurrent spectra on the deformed nanowire. These are listed in sequence in Table 5.1.

The peak positions are also plotted in Figure 5.4d to clearly depict the relationship. It is clear that there is an obvious correlation between the strain and the peak position shifts. To get the deeper insights into such correlation, the theoretical calculations were conducted.

*Please note that the strain value determination is intrinsically the same as that in Chapter 6 but with 2 times constant difference.

Splitting Values (eV)	Strain
0.01	3.0%
0.09	3.5%
0.10	4.1%
0.12	5.6%
0.13	6.1%
0.11	5.7%
0.13	5.0%
0.10	3.6%
0.08	2.5%

Table 5.1: Splitting values of photocurrent spectra on the deformed nanowire.

Photocurrent spectroscopy is one of the most important methods to obtain the band gap information from crystals. So, researchers have typically explained photocurrent behaviors in the frame of band gap theories. In my work, zinc oxide nanowire is appeared to be a highly crystalline direct band gap material tested without a substrate and in high vacuum. During bending, no other variables are added. Under such ideal conditions, it is reasonable to assume that changing of the band gap is directly correlated with the energy values of the photocurrent peak and its splitting. The total spectra containing an overall photoresponse might be mainly affected by the surface of the nanowire rather than its total body, also they may be affected by some pre-existing defects (usually oxygen vacancies, not created by bending), hence, the spectrum broadening due to splitting is probably hidden. Another detail is that the fiber transmission efficiency in my experiment is somewhat limited. The transmission efficiency decreases quite a lot at the UV range, at around 400 nm (or 3.1 eV), which cuts off the intensity of the incident light energy.

Theoretical calculations for deformed ZnO nanowires were performed by using Density Functional Tight Binding (DFTB) method which is implemented in the DFTB+ software package.[86] DFTB approach has widely been used for the accurate and efficient description of electronic, structural and transport properties of various inorganic materials especially for those which contain more than 1000 atoms in the simulation system. However, we are still limited by the simulation capability with regard to the number of atoms involved. Therefore we chose to simulate a ZnO nanowire with a diameter of 1.5 nm. Parametrization of Zn atom interactions with O atoms has been used for various bulk Zn-crystals such as hcp-Zn, zinc-blende-ZnS and wurtzite-Zinc Oxide, and ZnO surfaces (surface is clean with a small amount of adsorbates), and Zinc Oxide nanostructures. Such parameterization provided a good description of electronic band structures of zinc oxide including reasonable representations of the band structure and its band gap of 4.1 eV.[58]

We simulated a bent zinc oxide nanowire with various degrees of curvature and in accordance with the experimental deformation values, as shown in Figure 5.4a. Two sides of the nanowire are marked

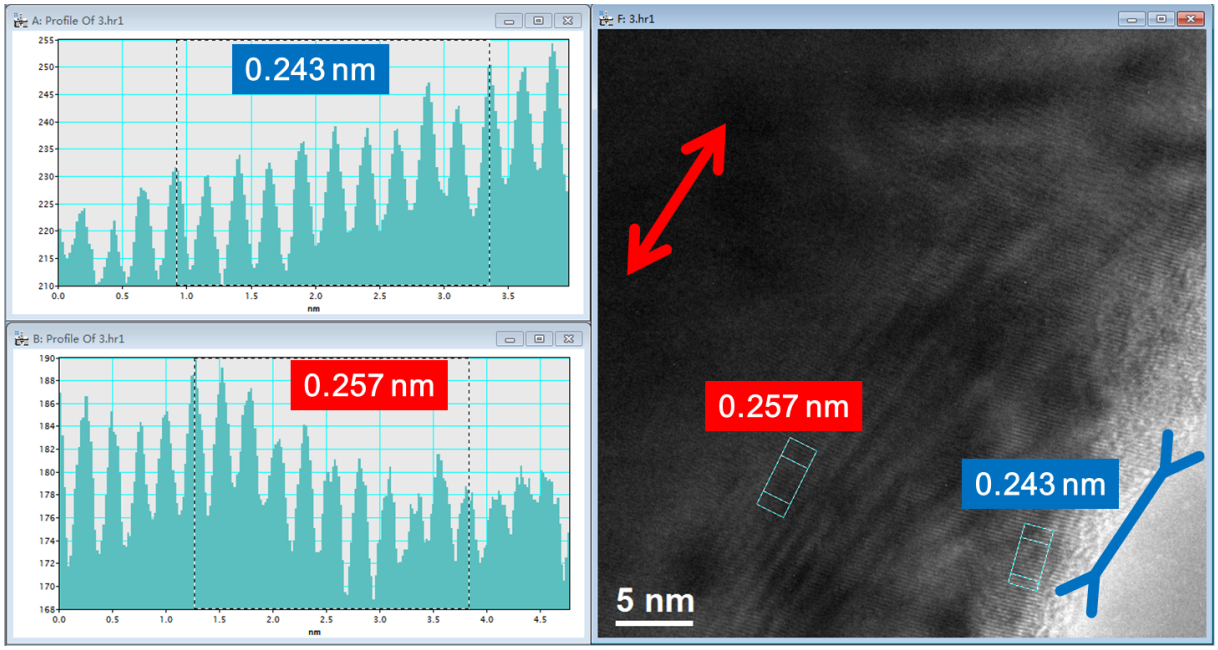

Figure 5.3: High-resolution TEM image of a deformed Zinc Oxide nanowire. The (002) lattice fringe separation is 0.243 nm at the most compressed sample edge, and 0.257 nm at the less compressed core.

by red or blue colors along with its expanded or compressed portions, respectively.

A simulated zinc oxide nanowire is constructed by 1500 atoms of Zn and O. To exclude the effect of dangling bonds and surface currents on the deformed structures, the simulated supercell surface was covered by a uniform layer of hydrogen atoms. Splitting of the photocurrent spectra is directly related to the splitting of levels in the valence band at Γ point with the corresponding red/blue shifts of the peaked wavelength values under bending. .[47]

The values of splitting partial density of states (PDOS) were calculated for the expanded and compressed sides of a nanowire, as shown in Figure 5.4b. During bending under TEM probing, the position of the conduction band was not changed. Only the valence band was affected.

In Figure 5.4b, the alternations in the valence band of the bent zinc oxide nanowire experiencing a strain of 4% are shown. PDOS peculiar to the expanded/compressed sides of the zinc oxide nanowire are marked in red and blue colors, respectively. Calculation results imply that the valence band shifts in a direction of a red range of wavelengths, whereas the compression causes the blue shift. This is a perfect match with the experimental data.

More simulations were also carried out for zinc oxide nanowires having various bending deformations from 1% to 4%. As shown in Figure 5.4c, these reveal a clear dependence of the band gap on strain. The changes of the band gap are obviously correlated with the changes in the photocurrent peak center, as measured in the *in situ* probing experiments, Figure 5.4d. Thus the obtained computational data exhibit a perfect agreement with the experimental data.

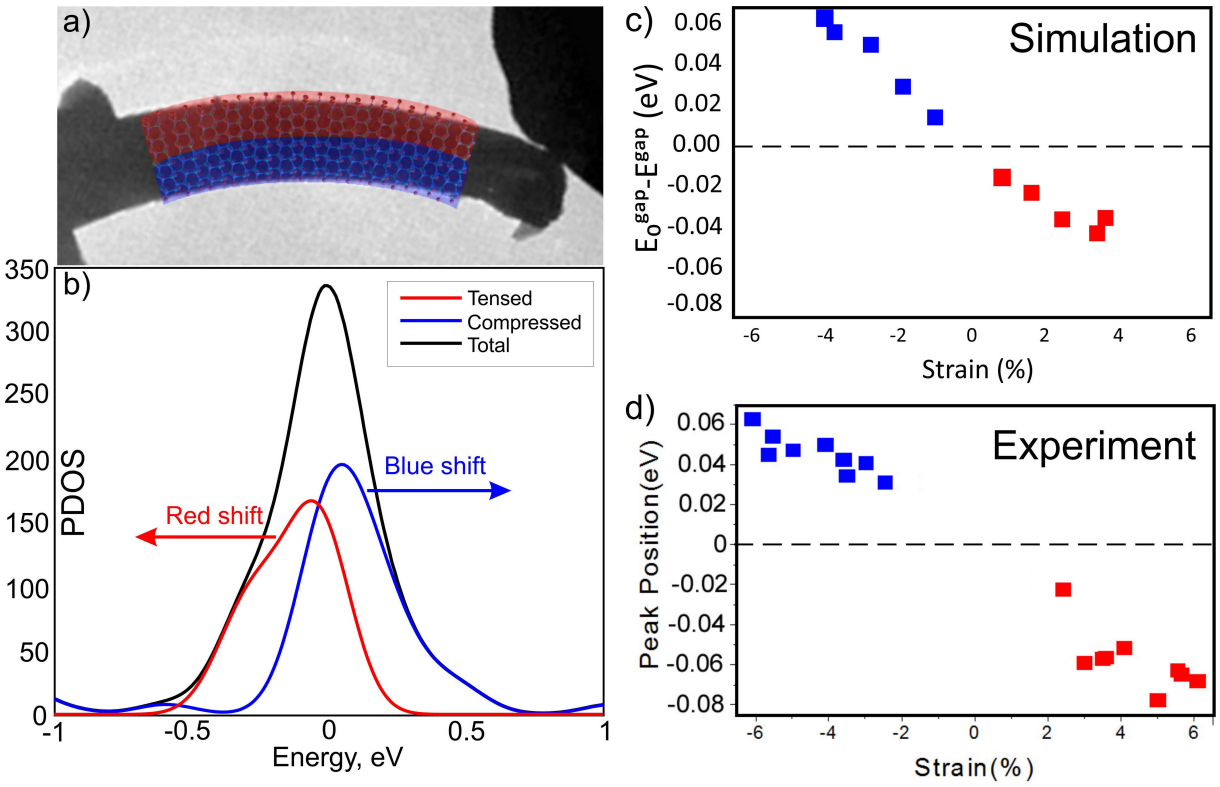

Figure 5.4: (a) Computed geometry of a deformed Zinc Oxide nanowire in accord with the experimental data. The simulated structure is divided into two domains (marked by red and blue colored portions) for the simulation of PDOS in expanded and compressed regions. Notice that the size of calculated geometry is not the same as for the experimental picture. (b) PDOS of expanded (red) and compressed (blue) sides of the deformed Zinc Oxide nanowire. Black curve shows the total DOS for the unbent nanowire, as a whole. Bending strain is 4%. (c) Dependence of the Zinc Oxide wire band gap on the bending strain in the frame of the DFTB approach adopted; (d) Dependence of the photocurrent peak position on the bending strain obtained experimentally. Red and blue colors denote the expanded and compressed regions of Zinc Oxide nanowires, respectively.

A few published results on deformed zinc oxide nanowires or microwires are in consistence with ours. For example, Xue et al. studied the strain effects on NBE of ZnO, which are characterized by CL inside a scanning electron microscope (SEM). They found that the emissions had had a relation with the strain.[113] Liao et al. also researched CL splitting and shift in deformed zinc oxide microwires in SEM. It is noted that the relationship between the excitation spectra evolution and compressive edges was rather clear. Also, it is believed that the valence band splitting would contribute to the NBE splitting.[58] In my *in situ* probing experiments, the splitting takes place not during CL measurements (a process stimulated by electron beam to emit light) but during recording of a photoresponse as the electrical current. This is a result of light absorption and the generation of electron-hole pairs. But, anyway, both processes share the same strain conditions that result in splitting of energy levels in the valence band at the Γ point.

5.4 Conclusions

To conclude, this Chapter discussed on opto-mechano-electrical tripling phenomena under *in situ* imaging and probing measurements of photocurrents in zinc oxide nanowires in real time, and under high spatial resolution. By comparing photocurrent spectra of individual free-standing zinc oxide nanowires under strain, splitting of photocurrent spectra was recorded. The shifts of photocurrent peaks were in an obvious correlation with the bending strains. The red/blue shifts were proved to be directly related to the splitting of energy levels in the valence band at the Γ point. DFTB calculations documented a perfect match with the *in situ* experimental results. The splitting of photocurrent spectroscopy gives an important clue for future flexible optoelectronics and piezo-phototronics. For example, it would be highly useful for strain-tuned wavelength-division multiplexing modules or MOEMS devices, and for flexible optoelectronics where photocurrent splitting values must be evaded as a key variable.

6

Statistically Analyzed Photoresponse of CdS Nanowires by *in situ* TEM

To get the missing information for future flexible optoelectronics based on nanoscale building blocks, as I discussed in Chapter 5, light, force and electrical currents are all important factors to be included into an *in siu* probing experiment. I demonstrate herein that high resolution TEM coupled with light illumination of a specimen and its electrical/mechanical probing can be applied for the *in situ* study of initiated photocurrents in free-standing individual nanowires. The crystallography of numerous individual CdS nanowires is analyzed simultaneously with the photocurrent measurements. My research implies that elastically deformed wurtzite CdS nanowires show statistically unchanged values of photo-to-dark current (ON/OFF) ratios. It is discovered that the cut-off wavelength possesses red shifts of photocurrent spectrum after nanowire bending. It is caused by deformation-induced lattice strain or associated changes in the electronic band structure, which is additionally proved by selected area electron diffraction (SAED) analyses and density functional tight binding (DFTB) calculations. The stable ratios of ON/OFF ratios, as well as photocurrent spectroscopy shifts of deformed CdS nanowires are important clues for future flexible optoelectronics and photovoltaics.

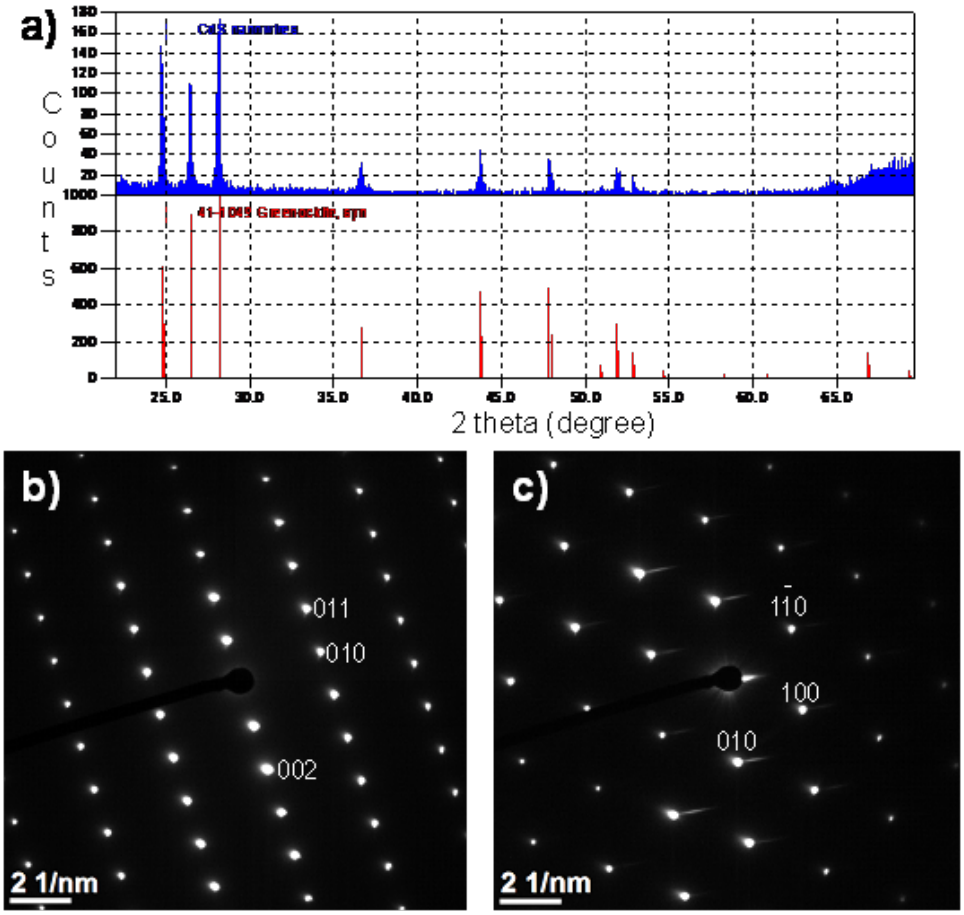

Figure 6.1: (a) XRD data of the nanowire sample (upper panel) fits a CdS hexagonal phase, JCPDS Card No. 41-1049 (lower panel). (b,c) Two SAED patterns of a CdS nanowire taken along the [100] and [001] directions, respectively.

6.1 Introduction

As I mentioned in Chapter 1, flexible electronics and optoelectronics have attracted general public attentions in recent years because of the growing requirements for portable electronic devices having high performance and a low manufacturing cost.[6, 51, 53] With high surface-to-volume ratios, excellent carrier mobility and chemically decorated surfaces, which can further be modified/functionalized, one-dimensional inorganic semiconducting nanostructures are attractive candidates for lithium-ion batteries,[93] future flexible displays,[34] solar cells,[127] supercapacitors,[44] nanogenerators,[19] sensors,[126] etc.

One of the crucial challenges for future applications is the nanostructure electrical and mechanical statistical stability. Although usually most reports claim that the nanowire conductivity is stable during mechanical deformations, there have been no deep and direct investigations related to the photoconductivity or photocurrent spectroscopy of free-standing individual nanowires under conditions which

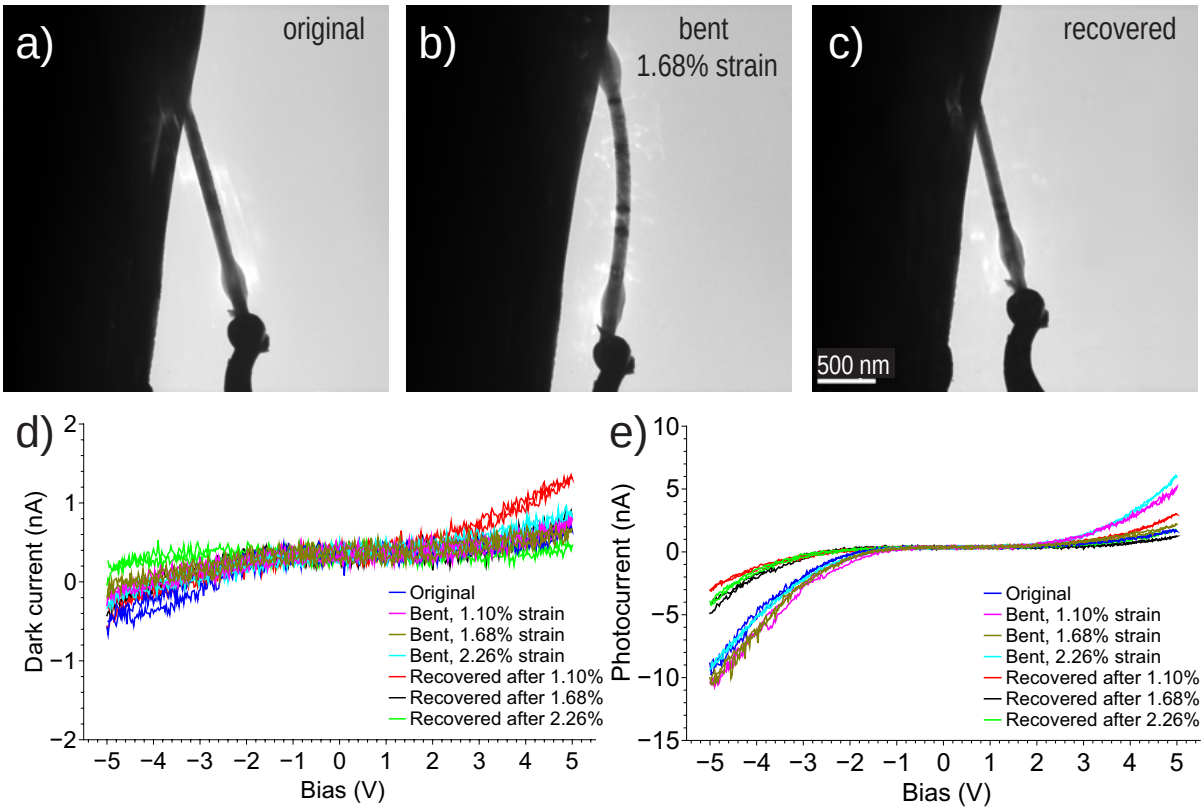

Figure 6.2: Representative TEM images of the original (a), bent (b) and recovered (c) states of an individual CdS nanowire positioned between fixed Au (left hand side) and movable W (right hand side) electrodes; and a summary of dark current (d) and photocurrent (e) measurements at different stages of the bending-recovery process. Calculated strains are marked on the TEM image and I-V plots.

allow for the real-time observations of deformation-induced strains.

Hence, it is rather unclear how the crystallography changes in deformed nanowires affect their photoresponses. It is noteworthy that some materials were found to be unstable during elastic deformations.[1] Herein, I thoroughly consider these issues by performing *in situ* HRTEM experiments using the optical TEM holder discussed in Chapter 2.

I chose cadmium sulfide (CdS), a direct band gap semiconductor for diverse photoelectronic devices, as my testing nanowire material.[109] Using paired probing and microscopy techniques, the electrical currents generated in light-illuminated specimen were measured by source-measuring units.

Initial testings revealed an unclear correlation between deformations and current values. To exclude the uncertainty introduced by the contact conditions, and to account for the structural diversity of the nanowires, I performed detailed statistical analysis based on numerous sets of experiments. Then the photocurrent spectroscopy measurements were performed. The spectroscopy reveals red-shifts for the cut-off wavelength of the nanowires under strain. The final part of the work attempts to characterize the strain-induced structural changes using electron diffraction analysis.

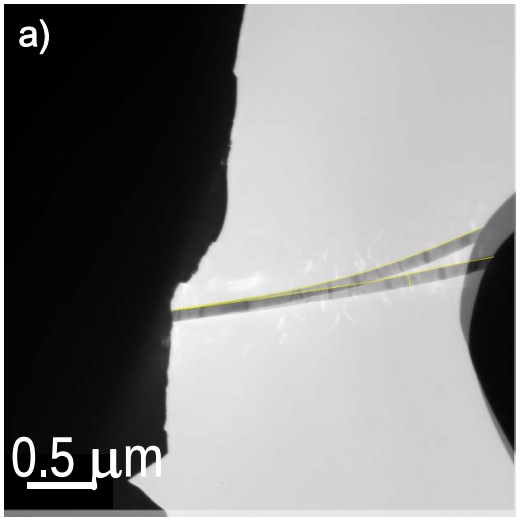

b)

Parameter	Value (µm)
Radius of original state	27.189
Radius of deformed state	7.639
Diameter of the nanowire	0.081

Figure 6.3: Strain values for an individual nanowire was determined under TEM imaging. (a) Two overlapped images of the nanowire in different states. (b) Measurements of the diameter of the nanowire, and its radius of curvature for the two cases. The strain was calculated as d/R, where d and R represent the diameter and the radius of curvature, respectively. The values were measured by using the *Digimizer* software*.

6.2 Experimental

CdS nanowires were synthesized via traditional chemical vapor deposition (CVD) method on silicon substrates or graphite plates. The fabrication conditions were reported in my published work.[123] The sizes of nanowires were around 100 nm in diameter and a few micrometers in length. The crystal structure of the nanowires was wurzite, which was confirmed by X-ray diffraction and SAED pattern, as shown in Figure 6.1. The samples were put onto a freshly-cut flattened gold wire tip by using a minimum amount of electrically-conductive silver epoxy.

As illustrated in Figure 2.5 in Chapter 2, the system is equipped with an optical fiber protruded through the TEM specimen holder, and with a piezo-tube for an electrical/mechanical probing inside the pole piece of the microscope. The probe with a tip radius ranging from 50 nm to several micrometers was aligned to the axis of the optical fiber core at a distance of 0.5 mm. Probing, imaging and diffraction studies were conducted by using the same energy-filtered 300 kV JEM-3100FEF high-resolution TEM, under high vacuum (10^{-5} Pa) at room temperature. For more information please refer to the description of engineering details of a piezo-driven optical TEM holder in Chapter 2.

Two types of *in situ* experiments were conducted:

(1) Photocurrent I-V measurements, as illustrated in Figure 2.5 Scheme 1 in Chapter 2, while probing the I-V response of nanowires irradiated by a laser diode with a working wavelength of 488 nm.

(2) Photocurrent spectroscopy measurements, as described in Figure 2.5 Scheme 2 in Chapter 2, while measuring the wavelength dependency of the electrical current generated inside the nanowire

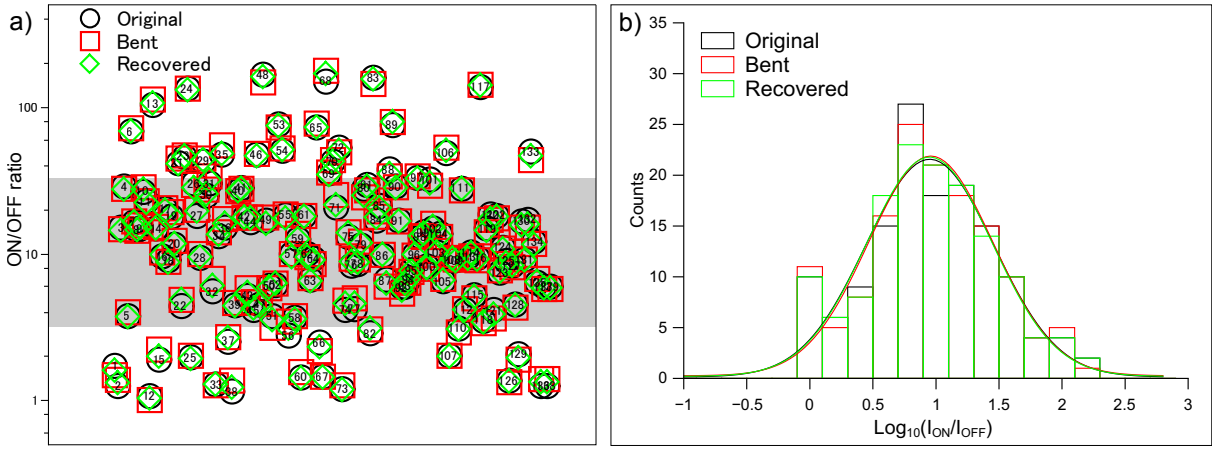

Figure 6.4: Statistical distribution of the measured ON/OFF (photocurrent/dark current) ratios for 139 bending/recovery experiments performed on free-standing single CdS nanowires. (a) ON/OFF ratios scatter mainly fits a gray region where the majority of measured ratios are included. (b) Statistical analysis of the ratios in log scale. The lines represent Gaussian fits for the three histograms.

under light illumination. The light source for photocurrent spectroscopy was a powerful laser driven light source (LDLS). The output of LDLS was then monochromated in order to carry out wavelength-selected measurements. In order to resolve the signal out of the noise, a chopper and a lock-in amplifier were applied in the measurement system.

6.3 Results and Discussions

Photocurrents and dark currents of the nanowires were carefully measured by the sourcemeter before deformation, after it and after final and complete nanostructure recovery. Some of nanowires revealed stable contact properties during the deformations and recoveries, the other deviated from the stable behavior and possessed changed currents. Figure 6.2a illustrates a contact to a nanowire in its original non-deformed state.

The average strain was defined as $\varepsilon = \frac{d}{R}$, where d is the diameter of the nanowire, R is its radius of curvature.† These two parameters were determined by a software, employing a curvature fit to the TEM images, as presented in Figure 6.3 for a representative nanowire. I always try my best to get an intimate and stable physical contact, therefore the probe was slightly pressed towards the nanowire to avoid possible sliding between the probe and the specimen, as presented in Figure 6.2a. The probe was then moved within the image plane for about 200 nm, leading to a strain of up to 1.68%, as presented in Figure 6.2b. The nanowire was finally recovered to its unbent state by moving the probe backwards, as illustrated in Figure 6.2c. The I-V measurements were performed in both dark and illuminated conditions

†Please not the the strain value determination here is the same as that in Chapter 5 in principle, but with a difference of constant factor of 2.

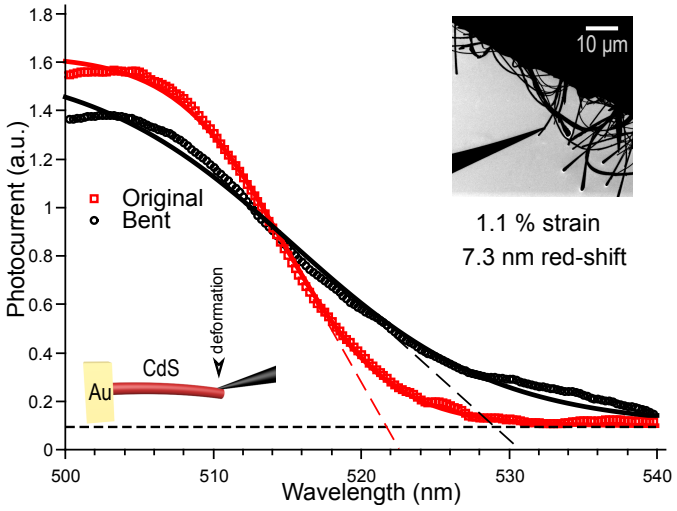

Figure 6.5: Photocurrent spectroscopy measurements performed on a representative individual CdS nanowire. The spectra have been fitted with logistic decay functions (solid lines); the regions of the curves corresponding to the symmetry point of each function have been extrapolated (dashed lines) to determine the intersections with the horizontal asymptote (dotted line). Left inset shows a schematic of the bending experiment. Right inset shows a low-magnification TEM image of the selected nanowire in contact with the W probe.

in each state, as summarized in Figure 6.2d-e. In order to get a clear understanding of the correlation between the deformation states of the nanowires and the photocurrent responses, I performed numerous experiments for a comprehensive statistical analysis. The current values were found to be very much scattered. However, I found that the light ON/OFF ratio (photocurrent to dark current ratio) of the nanowires could be nearly stable.

In this Chapter, I define three ON/OFF ratios, corresponding to the original, deformed and recovered states as:

$$R_{ori} = \frac{I_{ph-ori}}{I_{dr-ori}}, R_{def} = \frac{I_{ph-def}}{I_{dk-def}}, R_{rec} = \frac{I_{ph-rec}}{I_{dk-rec}}$$

, where *dk* and *ph* correspond to dark current and photocurrent, while *ori*, *def* and *rec* refer to the original, deformed and recovered states of the nanowire, respectively.

As presented in Figure 6.4a, the values vary a lot for different cases. This might be caused by contact changes during probing, but the ON/OFF ratios are rather stable for each individual case. The statistical distributions of the ON/OFF values in Figure 6.4b imply that this trend is valid in a wider scale and also allows us to estimate an average value of about 10, or around 7 to 20. The results of stable ON/OFF ratios made the majority of cases but some data had some deviations. Actually it is due to limitations of our setup with respect to the number of electrodes employed. These are only two. With only two electrical contacts, the contact resistance becomes an important uncertainty.[29] We expect that this variable could be reduced by the statistical analysis (on the basis that the contact resistance is normally randomly distributed). We expect that the nature of this variable (with respect to the resistance of the

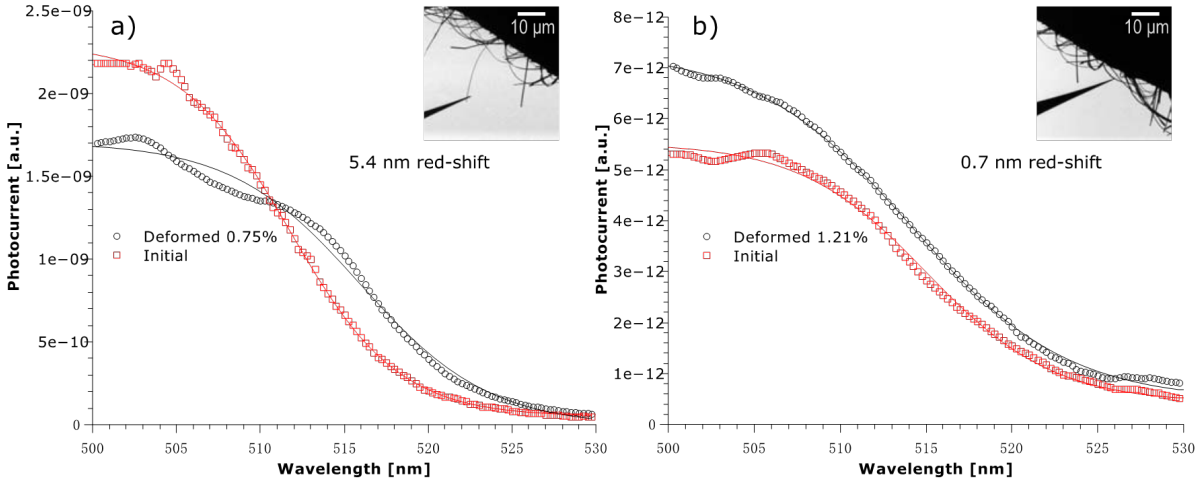

Figure 6.6: (a,b) Additional examples of photocurrent spectroscopy on individual CdS nanowires, in their initial and deformed states. Low magnification TEM images are shown in the insets for each case. Strain and red-shift values are marked on each plot.

nanowire itself) allows for various contributions to be effectively separated. This enables us to observe the effects which are intrinsic to the nanowire samples themselves.

To get an additional information the photocurrent spectroscopy was performed under simultaneous TEM imaging.

In Figure 6.5, the photocurrent spectroscopy results are plotted before and during the deformation process which introduces a 1.1% elastic deformation. The NW photocurrent cut-off wavelength possesses a 7.3 nm red shift under strain. At the initial state the edge wavelength was located at 521.8 nm. After deformation, the cut-off wavelength increased to 529.1 nm. More examples which feature similar red-shifts for the cut-off wavelength are shown in Figure 6.6. To sum up, the shifts of cut-off wavelength with regard to strains are listed in Table 6.1.

Thus an average value of 3.3 ± 2.9 nm is obtained from Table 6.1. The shift data shows that the effect is not limited to individual cases. The cut-off wavelength of the photocurrent spectrum is directly related to the electronic band structure. Thus it determines the near-band-edge emission (NBE) of the material. Our observations are consistent with the previous publications performed by measuring the CL of CdS

Strain (%)	Red shifts (nm) (%)
1.68	1.2
0.75	5.4
1.59	-0.6
1.21	0.7
3.36	5.5

Table 6.1: Cut-off wavelength shift values for the independently deformed nanowires.

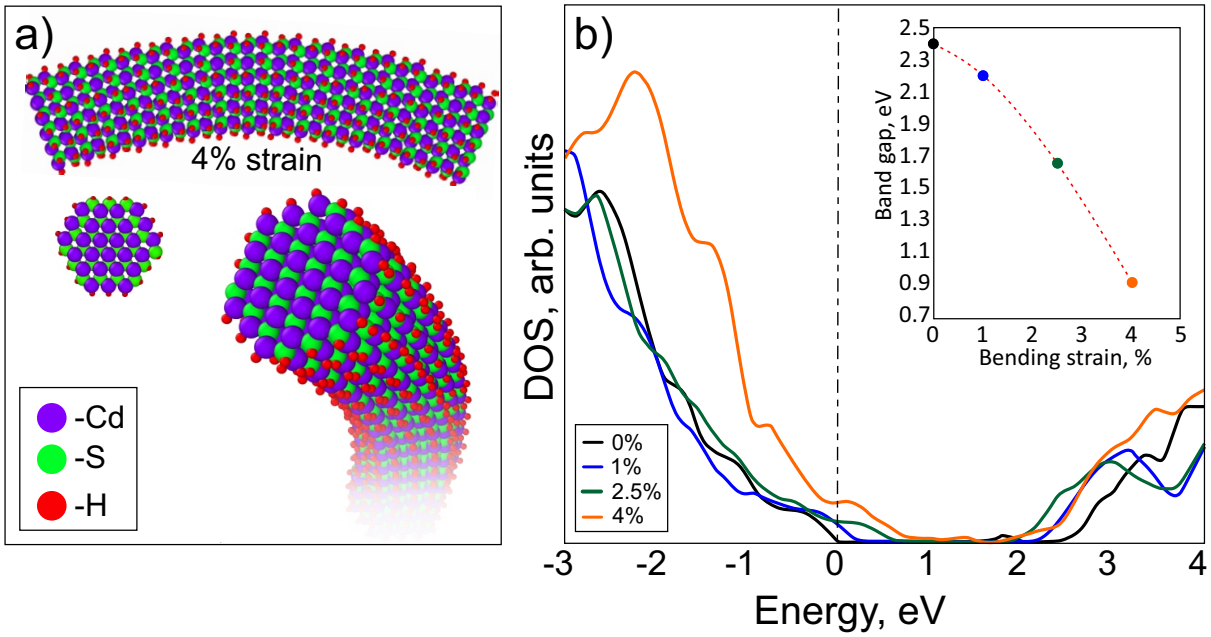

Figure 6.7: (a) Simulated atomic model of the CdS nanowire in plane, top, and 3D views. (b) Electron DOS for CdS nanowires with different degrees of bending. The Fermi energy is shifted to zero. The right-hand-side inset shows the band gap dependence on the bending strain.

nanowires inside SEM, where the authors observed red-shifted emission for the NBE peak under strain. This is an indication for a decrease in the bandgap value and it is in agreement with our data.[21]

Then we developed a model of bent CdS nanowires having various degrees of curvature in accordance with the experimental deformation values. A simulated supercell of a CdS nanowire (consisting of 1500 atoms of Cd and S) is illustrated in Figure 6.7. In order to avoid the presence of dangling bonds and surface currents over the bent nanowires, they were covered by a uniform layer of hydrogen atoms.

For each bending strain the electron density of states (DOS) was calculated (Figure 6.7b). It was found that with increasing strain the band gap value decreases (see Figure 6.7b), which is caused by the change of the top of the valence band and of the bottom of the conduction band. The obtained band gap behavior agrees well with the earlier DFT calculations carried out within a small bending range (up to 2%).[21] Decreasing of the band gap is directly related to the experimentally observed red shift of the photocurrent response. In the inset of Figure 6.7b the dependence of the band gap value on the bending strain is shown. By increasing the strain to 4% the band gap decreases from 2.4 eV to 0.9 eV.

Because of the relatively low strain and absence of temperature effects in calculations no structural defects are obvious. Only direct surface reconstruction within the bent regions was observed which could generate the small distortion (decreasing distance between the neighboring surface atoms) and further reduce the band gap. Also, the present nanowires were deformed elastically, compared to the previous research where larger strains (>10%) took place.[94]

Evidence of the strain effects may cause the valence band decrease. Such strain effects may be ob-

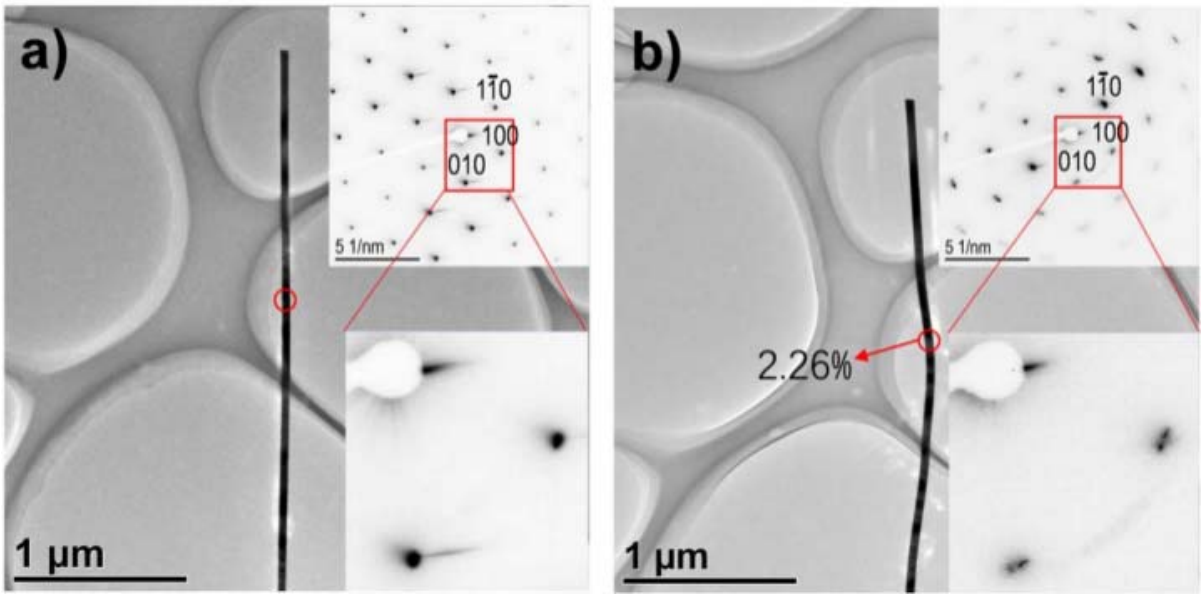

Figure 6.8: TEM images of the nanowire (a) before, and (b) after bending on a TEM carbon grid using a standard double-tilt holder due to the electron beam irradiation of the supporting C segments. The insets show SAED patterns along the [001] direction from areas marked by red circles. Representative framed parts of the SAED patterns are zoomed-in in the lower-right parts of the panels.

served by electron microscopy. Figure 6.8ab presents the images of a CdS nanowire at the initial and deformed states. Insets of Figure 6.8ab are SAED patterns from the area marked in Figure 6.8ab.

The averaged results presented here cannot accurately describe a single selected nanowire for its overall functional performance. In fact, the nanowires vary based on their morphology and structural peculiarities, even within the same synthetic batch of the material. There is a contradiction between the needs to accurately control the properties of every nanowire and the requirements for their high-yield production. However, from a statistical point of view, within a large number of structures, the nanowires studied here have common properties with respect to their photocurrent-to-dark current ratios.

This means that the drawn conclusion is particularly important for devices fabricated by a large amount of nanowires (their bunches) instead of a single nanowire device. Some successful examples of making flexible photodetectors,[112] flexible transparent electrodes,[49] flexible supercapacitor electrodes,[49] LED arrays,[92] lithium-ion batteries,[93] and solar cells,[127], etc should be mentioned in this regard.

6.4 Conclusions

In conlusion, I have successfully performed photocurrent measurements for elastically deformed CdS nanowires inside the HRTEM. Using *in situ* probing technique and the light illumination, I have characterized the electronic (dark current) and optoelectronic features of individual nanowires under mechanical deformation. To make the data reliable for future bottom-up applications, a large variety of nanowires was measured, which made possible an accurate statistical analysis of their properties. All nanostructures reveal fairly similar ON/OFF ratios in original, bent and recovered states, with this value mainly locating between 7 to 20. Photocurrent spectroscopy of several nanowires revealed red shifts of cut-off wavelength of several nanometers. These tiny shifts are mainly caused by deformation-induced strains, which induce changes in the electronic band structure. By taking SAED patterns, the strain induced structural deformation was vizualized after bending. The experiments reflect a variety of bending-induced stability features for individual nanowires. However, from a statistical point of view, the nanowires display common features in their response to deformation, making them highly valuable for future flexible optoelectronic applications.

7

Conclusions and Future Perspectives

In summary, probing technique is applied to nanomaterials using *in situ* TEM with many factors considered, such as chemical transitions, physical (electrical and mechanical) contacts and light illuminations. I reviewed and introduced related research in *in situ* probing TEM of nanomaterials for flexible optoelectronics and ion batteries applications in Chapter 1. Then the engineering details are discussed and presented in Chapter 2. Some behaviours or performances are revealed and discussed in Chapters 3-6, I finally summarize them herein and express my views of the future prospects based on my detailed understanding due to my PhD research experience.

7.1 Conclusions

In Chapter 3, a direct and informative *in situ* probing *nanoarchitectonics* technique to construct individual axial nanowire junctions has been for the first time realized. *In situ* HRTEM and in-tandem crystallography characterizations and optoelectronic behavior studies uncover the optical sensing properties of the single-crystalline axial CdS/p-Si nanowire junctions. The junctions exhibit decent selectivity toward the light wavelength shorter than those of the yellow range. It is very interesting that the junctions hold specific photocurrent saturation effect. The saturation of photocurrent at a relatively large bias could be utilized for the low power consumption light intensity sensing and integrated tunable voltage-

driven devices, thanks to the corresponding current limitations and excellent tolerance toward some unreliable/unstable biases. Obviously, the present *nanoarchitectonics* approach employing *in situ* structural design and measurements gives hope for the timely establishing detailed operational principles of bottom-up nano-devices.

In Chapter 4, the designed phase-transformation route was found to be successful for fabrication of an N doped graphene-phosphorus anode material with layered sandwich-like morphologies where very thin amorphous red P layers are placed within flexible and conductive N-doped graphene frameworks.

Advantages of the as-designed anode material have been studied by various characterization techniques, device tests, *in situ* microscopy and theoretical calculations. These advantages are:

(1) Thin P layer on the doped graphene (instead of crystalline P) anode shows ultrastable efficiency of 0.002% decay per cycle and good rate capability of 809 mAh/g at 1500 mA/g;

(2) P-C stable bonds may exist to tighly bind GN and P layers;

(3) *In situ* HRTEM experiments verified and revealed the reasons behind the ultrastable performance.

Chapter 5 discusses on the opto-mechano-electrical tripling phenomenon under *in situ* observation and probing measurements of photocurrents in zinc oxide nanowires in real time, and under high spatial resolution. By comparing photocurrent spectra of individual free-standing zinc oxide nanowires under strains, splitting of photocurrent spectra is established. The shifts of photocurrent peaks are in obvious correlation with the bending strains. The red/blue shifts are proved to be directly related to the splitting of energy levels in the valence band at Γ point. DFTB calculations show a perfect match with the *in situ* probing experimental results. The splitting of photocurrent spectroscopy provides an important information for future flexible optoelectronics and piezo-phototronics. For example, this can be considered for strain tuned wavelength-division multiplexing modules or MOEMS devices, and for flexible optoelectronic components where photocurrent splitting value should be evaded as a key variable.

In Chapter 6, I have successfully performed photocurrent measurements for elastically deformed CdS nanowires inside the HRTEM. Using *in situ* probing technique and light illumination, I have characterized the electronic (dark current) and optoelectronic features of individual nanowires under mechanical deformation. To make the data reliable for future bottom-up applications, a large variety of nanowires was measured, which made possible an accurate statistical analysis of their properties. All nanostructures reveal similar ON/OFF ratios in original, bent and recovered states, with a value mainly locating bwtween 7 and 20. Photocurrent spectra of several nanowires possess red shifts of cut-off wavelength of several nanometers. These tiny shifts are mainly caused by deformation induced strains, which result in the changes in the electronic band structure. By taking SAED patterns, the strain-induced structural deformation was confirmed after bending. The experiments reveal a variety of bending-induced stability for individual nanowires. However, from a statistical point of view, the nanowires display common features in their response to deformation, making them valuable for future flexible optoelectronic appli-

cations.

7.2 Future perspectives

7.2.1 Nanoscale building blocks in future

Although many researchers always claim that their nanomaterial samples are perfect and uniform, the quality is not that perfect to clarify on identical physical or chemical properties.

In Chapter 3, we noticed that the reproducibility (Table 3.1) is very high for heterojunctions with respect to the discovered saturation effect. But the current values vary a lot based on different sizes of building blocks. In Chapter 6, it is noticed that even the ratios of photo-to-dark current ratios in different states are more or less stable, the photo-to-current ratios of each nanowire are very different from each other. The scattered distribution of the ratios is caused by non-uniform structural features and chemical compositions. To use the nanowires in bundles is practical in some applications, while it is not practical to apply them in a single nanowire device for the mass production.

It is expected that nanoscale building blocks can be really uniform at the nanoscale. Such nanoscale building blocks become the bricks for the follow-up architecture. When the synthesis of various nanoscale building blocks can be well controlled to reach identical morphology, surface, physical, and chemical properties, the manufacturing process will become reliable and reproducible.

Another problem is that the current understanding of many nanomaterials is not yet comprehensive. But if the materials are synthesized with the identical morphology and crystallography, their properties are easier to be controlled.

7.2.2 Nanomanipulations in microscopy in the future

We are now in 2017, the age of nanotechnology, gene engineering, information technology, artificial intelligence and many more striking discoveries. According to the history of tools, human beings are now quite new to the nanometer scale. The tools we are using for the nano-world are electron microscopy, atomic force microscopy, lithography, piezoelectric probing and other technologies. It is true that various nanostructures are indeed successfully synthesized these days, they may be designed on electronic chips for mass production, and their observations may be performed at the atomic resolution. However, lithography technology does not work for many other applications, microscopy has sampling limitations, mechanical technology is not mature yet to handle nanoscale building blocks easily.

During my research toward a PhD degree, I successfully performed thousands of nanoscale operations manually. Most processes are based on my personal experience. If we are able to translate our experience into codes for a machine, it is very possible that machines become able to perform the repeatable operations. In Figure 7.1, an example of automation of nanomanipulation is illustrated. In

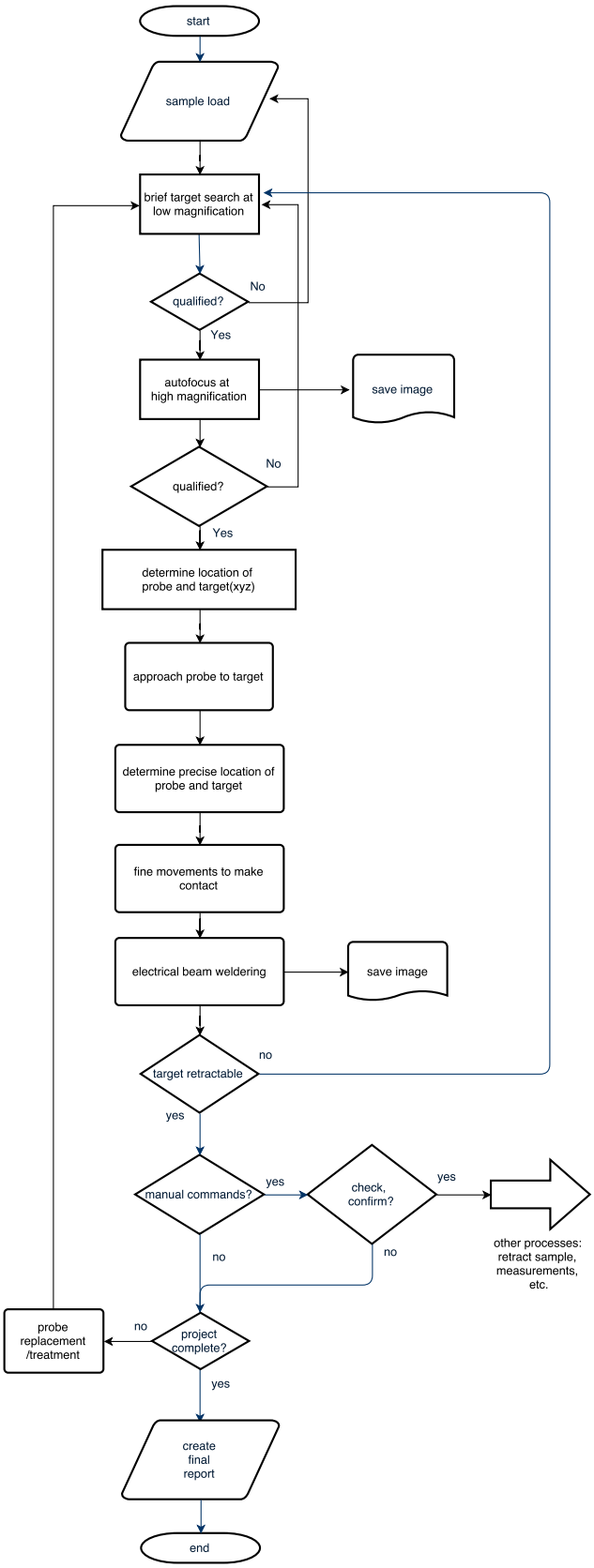

Figure 7.1: The workflow for nanoscale manipulations by automation.

this workflow figure, the machine starts from sample loading, and then performs searching of qualified nanostructure targets, followed by automation of microscopy, second qualification check, autofocus and auto-alignment for high resolution imaging, third qualification check, determining location of probe and target sample, approaching and contacting probe to target, electron beam soldering, retracting a nanostructure target, and many other possible functions. Automation of nanoscale handling through SEM and AFM is also under research now. [20] We expect that automation will be mature for mass production of future micro- and nano-flexible optoelectronics based on bottom-up technology using various nanomaterials.

7.2.3 Nanomaterials for energy storage in the future

Nanomaterials are superior in offering large surface to volume ratios, decent transport properties, variable physical parameters, and confinement effects owing to their nanoscale dimensions, and have been extensively studied for energy-related applications, such as solar cells, thermoelectrics, ion batteries, supercapacitors, and gas storage accumulators.

It is expected that the future energy storage is structurally designed down to nanoscale world to fully ultilize the nanodimensions – as Feynman said, *there is plenty of room at the bottom*. The volumetric capacity could be much higher, while at the same time the battery becomes stable and safe.

The problems may be solved through:

(i) generating optical effects to enhance the optical absorption in solar cells,

(ii) implementing a large surface area to boost the electrochemical reaction or molecular adsorption occurring at the solid–liquid or solid–gas interfaces, and

(iii) ensuring perfect crystallinity and/or porous structures to boost the electron or ion transport and electrolyte diffusion, so as to guarantee that the electrochemical process takes place with high efficiency. It is stressed that, in order to further optimize the capabilities of nanostructured materials for energy conversion and storage, new mechanisms and nanostructures are eagerly awaited.

In addition to highlighting the obvious advantages of nanostructured materials, their limitations and challenges for the usage in solar cells, lithium ion batteries, supercapacitors, and hydrogen storage systems are also required to be further investigated in all details.[17]

7.2.4 Nanoscale optoelectronics in the future

All of us are expecting optoelectronics to be integrated into our daily life. To develop an integrated optical interconnect technology and to significantly decrease the energy consumption of future computing systems such paradigm could not be underestimated. The low-loss and high-speed features of optical interconnects would allow for the usage of much greater bandwidths. Taking electrical signals from processors and transferring them into optical/light signals, which are then transmitted *via* optical

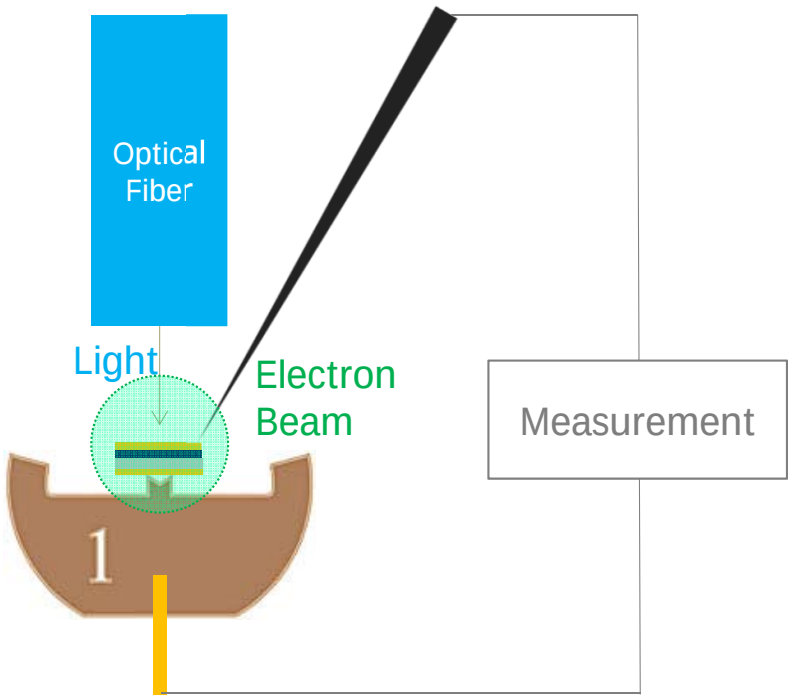

Figure 7.2: *in situ* TEM built solar cell. The layered specimen is prepared as a cross section of the solar cell.

waveguides on printed circuit boards, are the urgent steps. This is paving the way for integrating optical and electrical functions, as well as building components directly in the processors.

We probably would not get rid of silicon technology because it is still the best choice for microelectronics. However for an optical-electrical transfer, we require many semiconductors with different intrinsic electrical band structures. It is possible to integrate other materials, such as direct and wide band gap materials (such as CdS, ZnO), into silicon electronics.

Once the quality of these nanoscale building blocks becomes good enough (especially the present probably inconsistency is eliminated), once the nanoscale manipulation technology finds itself mature enough (mass automated production), the nanoscale optoelectronics should arrive at the real market. By simply placing several optoelectronic semiconducting nanoscale building blocks around a processor, optical-electrical signals within a single chip will first be applied to "green" and high-end computing, and then to our daily life necessities.

7.2.5 *In situ* probing TEM in the near future

To create pathways for future applications, experiments and investigations through *in situ* microscopy are fundamental and essential.

Various materials were tested using *in situ* probing microscopy. Besides Si, CdS, P@GN and ZnO, as discussed in previous chapters, many other materials, such as TiO_2 nanocrystals, MoS_2 nanosheets, ZnSe/GaP nanowires and CdS/ZnO branched nanostructures also exhibited clear photocurrent re-

sponses, while SnO_2@G microsheets, Si/C nanospheres, Cu/$Li_4Ti_5O_{12}$ scaffolds, MoS_2/C nanosheets and N doped graphene showed decent energy storage performances.

For electrical/optical *in situ* probing TEM experiments, many other samples which I measured did not demonstrate strong photocurrent responses. For example, In_2O_3, ZnS, boron nitride(BN), BN – C, BCNO, CN with wide/indirect band gap or low conductivity do not respond to the light illumination. For BN family materials, strong deep UV laser may excite carriers and lead to new results, but in my experiments, some regularly changing current signals were caused by absorbing light energy and heating.

Therefore, for the indirect band gap semiconductors, and for the not well-defined band gap materials, the electrical/optical *in situ* probing TEM is not easy to detect possible small optoelectronic signals for various optoelectronic applications, but it is expected to do so in the future. It is also thought that the optical fiber plus electrical measuring equipments shall be upgraded to collect and process lower scale signals from smaller (regions of) samples.

As I mentioned in Chapter 2, *in situ* photovoltage measurements are also possible to be performed by the similar microscopy setup.

For instance, solar cells are not investigated in detail by *in situ* TEM. One of my experimental designs for *in situ* solar cell is presented in Figure 7.2. The solar cell can be processed by slicing and FIB and then placed in TEM.

For physical/chemical *in situ* probing TEM experiments toward energy storage applications, the near future research is more clear, but still challenging. It is expected that the structure design would be more complicated and space-efficient while taking care of higher-level control of structural consistency, and quality of the samples. The *in situ* probing experiments for energy storage, including new types of ion-batteries (Aluminum-ion batteries and Magnesium-ion batteries), super-capacitors and some of the pseudocapacitors, are interesting directions which are anticipated.

References

[1] M. Antsov, L. Dorogin, S. Vlassov, B. Polyakov, M. Vahtrus, K. Mougin, R. Lõhmus, and I. Kink, *Analysis of static friction and elastic forces in a nanowire bent on a flat surface: A comparative study*, Tribology International, 72 (2014), pp. 31–34.

[2] M. Armand and J.-M. Tarascon, *Building better batteries*, Nature, 451 (2008), pp. 652–657.

[3] F. Banhart, *In-Situ Electron Microscopy at High Resolution*, World Scientific, 2008.

[4] P. Barpanda, G. Oyama, S.-i. Nishimura, S.-C. Chung, and A. Yamada, *A 3.8-V earth-abundant sodium battery electrode*, Nature Communications, 5 (2014), p. 4358.

[5] R. Berthelot, D. Carlier, and C. Delmas, *Electrochemical investigation of the P2–NaxCoO2 phase diagram.*, Nature Materials, 10 (2011), pp. 74–80.

[6] J. J. Boland, *Flexible electronics: Within touch of artificial skin.*, Nature materials, 9 (2010), pp. 790–792.

[7] P. G. Bruce, B. Scrosati, and J.-M. Tarascon, *Nanomaterials for rechargeable lithium batteries.*, Angew. Chem. Int. Ed., 47 (2008), pp. 2930–2946.

[8] Y. Cao, L. Xiao, M. L. Sushko, W. Wang, B. Schwenzer, J. Xiao, Z. Nie, L. V. Saraf, Z. Yang, and J. Liu, *Sodium ion insertion in hollow carbon nanowires for battery applications*, Nano Letters, 12 (2012), pp. 3783–3787.

[9] C. Y. Chen, J. H. Huang, J. Song, Y. Zhou, L. Lin, P. C. Huang, Y. Zhang, C. P. Liu, J. H. He, and Z. L. Wang, *Anisotropic outputs of a nanogenerator from oblique-aligned ZnO nanowire arrays*, ACS Nano, 5 (2011), pp. 6707–6713.

[10] D. Chen, Z. Liu, B. Liang, X. Wang, and G. Shen, *Transparent metal oxide nanowire transistors*, Nanoscale, 4 (2012), p. 3001.

[11] E. Çigdem and B. Murat, *Electrical and photovoltaic characterization of nCdS:In/Si heterojunction devices*, Solar Cells, 26 (1989), pp. 253–262.

[12] F. Claeyssens, J. N. Hart, N. L. Allan, and J. M. Oliva, *Solid phases of phosphorus carbide: An ab initio study*, Physical Review B - Condensed Matter and Materials Physics, 79 (2009), p. 134115.

[13] L. F. Cui, R. Ruffo, C. K. Chan, H. Peng, and Y. Cui, *Crystalline-amorphous core-shell silicon nanowires for high capacity and high current battery electrodes*, Nano Letters, 9 (2009), pp. 491–495.

[14] Y. Cui, Z. Zhong, D. Wang, W. U. Wang, and C. M. Lieber, *High performance silicon nanowire field effect transistors*, Nano Letters, 3 (2003), pp. 149–152.

[15] J. Deng, H. Ji, C. Yan, J. Zhang, W. Si, S. Baunack, S. Oswald, Y. Mei, and O. G. Schmidt, *Naturally rolled-up C/Si/C trilayer nanomembranes as stable anodes for lithium-ion batteries with remarkable cycling performance*, Angewandte Chemie - International Edition, 52 (2013), pp. 2326–2330.

[16] C. T. Dervos, P. D. Skafidas, J. a. Mergos, and P. Vassiliou, *pn Junction Photocurrent Modelling Evaluation under Optical and Electrical Excitation*, Sensors, 4 (2004), pp. 58–70.

[17] M. C. Dos Santos, O. Kesler, and A. L. M. Reddy, *Nanomaterials for energy conversion and storage*, Journal of Nanomaterials, 2012 (2012), pp. 3127–3171.

[18] F. Fabbri, E. Rotunno, L. Lazzarini, N. Fukata, and G. Salviati, *Visible and infra-red light emission in boron-doped wurtzite silicon nanowires.*, Scientific reports, 4 (2014), p. 3603.

[19] F. R. Fan, Z. Q. Tian, and Z. L. Wang, *Flexible triboelectric generator*, Nano Energy, 1 (2012), pp. 328–334.

[20] S. Fatikow and U. Rembold, *Microsystem Technology and Microrobotics*, Springer, 1997.

[21] Q. Fu, Z. Y. Zhang, L. Kou, P. Wu, X. Han, X. Zhu, J. Gao, J. Xu, Q. Zhao, W. Guo, and D. Yu, *Linear strain-gradient effect on the energy bandgap in bent CdS nanowires*, Nano Research, 4 (2011), pp. 308–314.

[22] N. Fukata, J. Kaminaga, R. Takiguchi, R. Rurali, M. Dutta, and K. Murakami, *Interaction of boron and phosphorus impurities in silicon nanowires during low-temperature ozone oxidation*, Journal of Physical Chemistry C, 117 (2013), pp. 20300–20307.

[23] N. Fukata, S. Matsushita, N. Okada, J. Chen, T. Sekiguchi, N. Uchida, and K. Murakami, *Impurity doping in silicon nanowires synthesized by laser ablation*, Applied Physics A: Materials Science and Processing, 93 (2008), pp. 589–592.

[24] K. Furumoto, T. Tanabe, N. Yamamoto, T. Daio, S. Matsumura, and K. Yasuda, *Development of Novel Optical Fiber System for Cathodoluminescence Detection in High Voltage Transmission Electron Microscope*, Materials Transactions, 54 (2013), pp. 854–856.

[25] L. Gao, D. Dong, J. He, K. Qiao, F. Cao, M. Li, H. Liu, Y. Cheng, J. Tang, and H. Song, *Wearable and sensitive heart-rate detectors based on PbS quantum dot and multiwalled carbon nanotube blend film*, Applied Physics Letters, 105 (2014), p. 153702.

[26] E. Garnett and P. Yang, *Light trapping in silicon nanowire solar cells*, Nano Letters, 10 (2010), pp. 1082–1087.

[27] Y. Gu, E. S. Kwak, J. L. Lensch, J. E. Allen, T. W. Odom, and L. J. Lauhon, *Near-field scanning photocurrent microscopy of a nanowire photodetector*, Applied Physics Letters, 87 (2005), p. 043111.

[28] Y. Huang, H. Hu, Y. Huang, M. Zhu, W. Meng, C. Liu, Z. Pei, C. Hao, Z. Wang, and C. Zhi, *From industrially weavable and knittable highly conductive yarns to large wearable energy storage textiles*, ACS Nano, 9 (2015), pp. 4766–4775.

[29] M. Hummelgård, R. Zhang, H. E. Nilsson, and H. Olin, *Electrical sintering of silver nanoparticle ink studied by In-situ TEM probing*, PLoS ONE, 6 (2011), p. e17209.

[30] B. W. Jaskula, *US Geological Survey of Lithium Reserves 2011*, tech. rep., U.S. Department of the Interior, 2011.

[31] Y. Jiao, Y. Zheng, M. Jaroniec, and S. Z. Qiao, *Origin of the electrocatalytic oxygen reduction activity of graphene-based catalysts: A roadmap to achieve the best performance*, Journal of the American Chemical Society, 136 (2014), pp. 4394–4403.

[32] Y. Kang, H.-D. Liu, M. Morse, M. J. Paniccia, M. Zadka, S. Litski, G. Sarid, A. Pauchard, Y.-H. Kuo, H.-W. Chen, W. S. Zaoui, J. E. Bowers, A. Beling, D. C. McIntosh, X. Zheng, and J. C. Campbell, *Monolithic germanium/silicon avalanche photodiodes with 340 GHz gain–bandwidth product*, Nature Photonics, 3 (2009), pp. 59–63.

[33] Y. Kim, Y. Park, A. Choi, N. S. Choi, J. Kim, J. Lee, J. H. Ryu, S. M. Oh, and K. T. Lee, *An amorphous red phosphorus/carbon composite as a promising anode material for sodium ion batteries*, Advanced Materials, 25 (2013), pp. 3045–3049.

[34] H. Klauk, *Device physics: nanowires' display of potential.*, 2008.

[35] S. Komaba, W. Murata, T. Ishikawa, N. Yabuuchi, T. Ozeki, T. Nakayama, A. Ogata, K. Gotoh, and K. Fujiwara, *Electrochemical Na insertion and solid electrolyte interphase for hard-carbon electrodes and application to Na-ion batteries*, Advanced Functional Materials, 21 (2011), pp. 3859–3867.

[36] G. Kresse, *From ultrasoft pseudopotentials to the projector augmented-wave method*, Physical Review B, 59 (1999), pp. 1758–1775.

[37] G. Kresse and J. Furthmüller, *Efficient iterative schemes for ab initio total-energy calculations using a plane-wave basis set*, Physical Review B, 54 (1996), pp. 11169–11186.

[38] J. Kupec, R. L. Stoop, and B. Witzigmann, *Light absorption and emission in nanowire array solar cells*, Opt. Express, 18 (2010), pp. 27589–27605.

[39] S. Kuze, J. Kageura, and S. Matsumoto, *Development of a Sodium Ion Secondary Battery*, SUMITOMO KAGAKU, 2013 (2013), pp. 1–13.

[40] P. F. Lang and B. C. Smith, *Ionic radii for Group 1 and Group 2 halide, hydride, fluoride, oxide, sulfide, selenide and telluride crystals.*, Dalton transactions (Cambridge, England : 2003), 39 (2010), pp. 7786–7791.

[41] C. S. Lao, J. Liu, P. Gao, L. Zhang, D. Davidovic, R. Tummala, and Z. L. Wang, *ZnO nanobelt/nanowire schottky diodes formed by dielectrophoresis alignment across au electrodes*, Nano Letters, 6 (2006), pp. 263–266.

[42] G. Larrieu and X.-L. Han, *Vertical nanowire array-based field effect transistors for ultimate scaling*, Nanoscale, 5 (2013), pp. 2437–2441.

[43] H. Li, X. Wang, J. Xu, Q. Zhang, Y. Bando, D. Golberg, Y. Ma, and T. Zhai, *One-dimensional CdS nanostructures: A promising candidate for optoelectronics*, Advanced Materials, 25 (2013), pp. 3017–3037.

[44] S. Li, J. Wen, X. Mo, H. Long, H. Wang, J. Wang, and G. Fang, *Three-dimensional MnO2 nanowire/ZnO nanorod arrays hybrid nanostructure for high-performance and flexible supercapacitor electrode*, Journal of Power Sources, 256 (2014), pp. 206–211.

[45] W. J. Li, S. L. Chou, J. Z. Wang, H. K. Liu, and S. X. Dou, *Simply mixed commercial red phosphorus and carbon nanotube composite with exceptionally reversible sodium-ion storage*, Nano Letters, 13 (2013), pp. 5480–5484.

[46] B. Liang, Y. Liu, and Y. Xu, *Silicon-based materials as high capacity anodes for next generation lithium ion batteries*, 2014.

[47] Z.-M. Liao, H.-C. Wu, Q. Fu, X. Fu, X. Zhu, J. Xu, I. V. Shvets, Z. Zhang, W. Guo, Y. Leprince-Wang, Q. Zhao, X. Wu, and D.-P. Yu, *Strain induced exciton fine-structure splitting and shift in bent ZnO microwires*, Scientific Reports, 2 (2012), pp. 1–6.

[48] A. Liu, R. Jones, L. Liao, and D. Samara-rubio, *A high-speed silicon optical modulator based on a metal – oxide – semiconductor capacitor*, Nature, 427 (2004), pp. 615–619.

[49] J. W. Liu, J. L. Wang, Z. H. Wang, W. R. Huang, and S. H. Yu, *Manipulating nanowire assembly for flexible transparent electrodes*, Angewandte Chemie - International Edition, 53 (2014), pp. 13477–13482.

[50] N. Liu, Z. Lu, J. Zhao, M. T. McDowell, H.-W. Lee, W. Zhao, and Y. Cui, *A pomegranate-inspired nanoscale design for large-volume-change lithium battery anodes.*, Nature nanotechnology, 9 (2014), pp. 187–92.

[51] Z. Liu, J. Xu, D. Chen, and G. Shen, *Flexible electronics based on inorganic nanowires*, Chem. Soc. Rev., 44 (2015), pp. 161–192.

[52] V. J. Logeeswaran, J. Oh, A. P. Nayak, A. M. Katzenmeyer, K. H. Gilchrist, S. Grego, N. P. Kobayashi, S.-Y. Wang, A. A. Talin, N. K. Dhar, M. S. Islam, L. VJ, J. Oh, A. P. Nayak, A. M. Katzenmeyer, K. H. Gilchrist, S. Grego, N. P. Kobayashi, S.-Y. Wang, A. A. Talin, N. K. Dhar, and M. S. Islam, *A Perspective on Nanowire Photodetectors: Current Status, Future Challenges, and Opportunities*, IEEE Journal of Selected Topics in Quantum Electronics, 17 (2011), pp. 1002–1032.

[53] Y.-Z. Long, M. Yu, B. Sun, C.-Z. Gu, and Z. Fan, *Recent advances in large-scale assembly of semiconducting inorganic nanowires and nanofibers for electronics, sensors and photovoltaics*, Chemical Society Reviews, 41 (2012), pp. 4560–4580.

[54] F. Luo, B. Liu, J. Zheng, G. Chu, K. Zhong, H. Li, X. Huang, and L. Chen, *Review—Nano-Silicon/Carbon Composite Anode Materials Towards Practical Application for Next Generation Li-Ion Batteries*, Journal of the Electrochemical Society, 162 (2015), pp. A2509–A2528.

[55] R. M. Ma, L. Dai, H. B. Huo, W. J. Xu, and G. G. Qin, *High-performance logic circuits constructed on single CdS nanowires*, Nano Letters, 7 (2007), pp. 3300–3304.

[56] B. K. Miller and P. A. Crozier, *In Situ Visible and UV Illumination of ETEM Samples*, Microscopy and Microanalysis, 18 (Suppl (2012), pp. 1074–1075.

[57] S. N. Mohammad and S. T. H. Abidi, *Theory of saturation photocurrent and photovoltage in p-n junction solar cells*, Journal of Applied Physics, 61 (1987), pp. 4909–4919.

[58] N. H. Moreira, G. Dolgonos, B. Aradi, A. L. Da Rosa, and T. Frauenheim, *Toward an accurate density-functional tight-binding description of zinc-containing compounds*, Journal of Chemical Theory and Computation, 5 (2009), pp. 605–614.

[59] S. Nagarajan, C. Pioche-Durieu, L. H. G. Tizei, C.-Y. Fang, J.-R. Bertrand, E. Le Cam, H.-C. Chang, F. Treussart, and M. Kociak, *Simultaneous cathodoluminescence and electron microscopy cytometry of cellular vesicles labeled with fluorescent nanodiamonds*, Nanoscale, 8 (2016), pp. 11588–11594.

[60] J. Ni, Y. Zhao, T. Liu, H. Zheng, L. Gao, C. Yan, and L. Li, *Strongly coupled Bi2S3@CNT hybrids for robust lithium storage*, Advanced Energy Materials, 4 (2014), p. 1400798.

[61] V. Nicolosi, M. Chhowalla, M. G. Kanatzidis, M. S. Strano, and J. N. Coleman, *Liquid Exfoliation of Layered Materials*, Science, 340 (2013), p. 1226419.

[62] F. Niu, L.-M. Tao, Y.-C. Deng, Q.-H. Wang, and W.-G. Song, *Phosphorus doped graphene nanosheets for room temperature NH3 sensing*, New Journal of Chemistry, 38 (2014), p. 2269.

[63] K. O'Brien, N. D. Lanzillotti-Kimura, J. Rho, H. Suchowski, X. Yin, and X. Zhang, *Ultrafast acousto-plasmonic control and sensing in complex nanostructures.*, Nature communications, 5 (2014), p. 4042.

[64] Y. Ohno, S. Takeda, and F. Scieace, *A new apparatus for in sifu photoluminescence in a transmission electron microscope*, October, 66 (1995), pp. 95–98.

[65] H. Okada, *Piezoelectric actuator*, 2002.

[66] S. P. Ong, V. L. Chevrier, G. Hautier, A. Jain, C. Moore, S. Kim, X. Ma, and G. Ceder, *Voltage, stability and diffusion barrier differences between sodium-ion and lithium-ion intercalation materials*, Energy & Environmental Science, 4 (2011), p. 3680.

[67] V. Palomares, P. Serras, I. Villaluenga, K. B. Hueso, J. Carretero-Gonzalez, and T. Rojo, *Na-ion batteries, recent advances and present challenges to become low cost energy storage systems*, Energy Environ. Sci., 5 (2012), pp. 5884–5901.

[68] H. Park, A. W. Fang, O. Cohen, R. Jones, M. J. Paniccia, and J. E. Bowers, *A hybrid AlGaInAs-silicon evanescent amplifier*, IEEE Photonics Technology Letters, 19 (2007), pp. 230–232.

[69] J. P. J. Perdew, K. Burke, and M. Ernzerhof, *Generalized Gradient Approximation Made Simple*, Phys. Rev. Lett., 77 (1996), pp. 3865–3868.

[70] W. Picht and W. Ruppel, *Photocurrent saturation in CdS single crystals under electron beam excitation*, Physica Status Solidi (B), 47 (1971), pp. 119–128.

[71] J. Qian, Y. Chen, L. Wu, Y. Cao, X. Ai, and H. Yang, *High capacity Na-storage and superior cyclability of nanocomposite Sb/C anode for Na-ion batteries*, Chemical Communications, 48 (2012), p. 7070.

[72] J. Qian, X. Wu, Y. Cao, X. Ai, and H. Yang, *High capacity and rate capability of amorphous phosphorus for sodium ion batteries*, Angewandte Chemie - International Edition, 52 (2013), pp. 4633–4636.

[73] J. Qian, M. Zhou, Y. Cao, X. Ai, and H. Yang, *Nanosized Na 4 Fe(CN) 6/C composite as a low-cost and high-rate cathode material for sodium-ion batteries*, Advanced Energy Materials, 2 (2012), pp. 410–414.

[74] G. T. Reed, *The optical age of silicon*, Nature, 427 (2004), pp. 595–596.

[75] W. Ren and H.-M. Cheng, *The global growth of graphene*, Nature Nanotechnology, 9 (2014), pp. 726–730.

[76] E. Roduner, *Size matters: why nanomaterials are different*, Chemical Society Reviews, 35 (2006), p. 583.

[77] W. L. Roth, T. W. DeWitt, and A. J. Smith, *Polymorphism of Red Phosphorus*, Journal of the American Chemical Society, 69 (1947), pp. 2881–2885.

[78] K. Sato, A. Castaldini, N. Fukata, and A. Cavallini, *Electronic level scheme in boron- and phosphorus-doped silicon nanowires*, Nano Letters, 12 (2012), pp. 3012–3017.

[79] W. Shen, C. Wang, Q. Xu, H. Liu, and Y. Wang, *Nitrogen-doping-induced defects of a carbon coating layer facilitate Na-storage in electrode materials*, Advanced Energy Materials, 5 (2015), p. 1400982.

[80] W. Shim, J. Yao, and C. M. Lieber, *Programmable resistive-switch nanowire transistor logic circuits*, Nano Letters, 14 (2014), pp. 5430–5436.

[81] W. Shockley and H. J. Queisser, *Detailed balance limit of efficiency of p-n junction solar cells*, Journal of Applied Physics, 32 (1961), pp. 510–519.

[82] C. Soci, A. Zhang, B. Xiang, S. A. Dayeh, D. P. R. Aplin, J. Park, X. Y. Bao, Y. H. Lo, and D. Wang, *ZnO nanowire UV photodetectors with high internal gain*, Nano Letters, 7 (2007), pp. 1003–1009.

[83] V. Srikant and D. R. Clarke, *Optical absorption edge of ZnO thin films: The effect of substrate*, Journal of Applied Physics, 81 (1997), p. 6357.

[84] D. a. Stevens and J. R. Dahn, *High Capacity Anode Materials for Rechargeable Sodium-Ion Batteries*, Journal of The Electrochemical Society, 147 (2000), p. 1271.

[85] J. Sun, G. Zheng, H. W. Lee, N. Liu, H. Wang, H. Yao, W. Yang, and Y. Cui, *Formation of stable phosphorus-carbon bond for enhanced performance in black phosphorus nanoparticle-graphite composite battery anodes*, Nano Letters, 14 (2014), pp. 4573–4580.

[86] F. T., *DFTB+, a Sparse Matrix-Based Implementation of the DFTB Method†*, Journal of Physical Chemistry A, 111 (2007), pp. 5678–5684.

[87] T. Tanabe, S. Muto, and S. Tohtake, *Development of new TEM specimen holder for cathodoluminescence detection*, Journal of Electron Microscopy, 51 (2002), pp. 311–313.

[88] W. Tian, C. Zhang, T. Zhai, S. L. Li, X. Wang, J. Liu, X. Jie, D. Liu, M. Liao, Y. Koide, D. Golberg, and Y. Bando, *Flexible ultraviolet photodetectors with broad photoresponse based on branched ZnS-ZnO heterostructure nanofilms*, Advanced Materials, 26 (2014), pp. 3088–3093.

[89] K. T. Tsai, G. A. Wurtz, J. Y. Chu, T. Y. Cheng, H. H. Wang, A. V. Krasavin, J. H. He, B. M. Wells, V. A. Podolskiy, J. K. Wang, Y. L. Wang, and A. V. Zayats, *Looking into meta-atoms of plasmonic nanowire metamaterial*, Nano Letters, 14 (2014), pp. 4971–4976.

[90] V. S. Vishnevsky, V. L. Kavertsev, I. A. Kartashev, V. V. Lavrinenko, M. M. Nekrasov, and A. A. Prez, *Piezoelectric motor structures*, 1977.

[91] M. M. Waldrop, *The chips are down for Moore's law*, Nature News, 530 (2016), p. 144.

[92] C. Wang, R. Bao, K. Zhao, T. Zhang, L. Dong, and C. Pan, *Enhanced emission intensity of vertical aligned flexible ZnO nanowire/p-polymer hybridized LED array by piezo-phototronic effect*, Nano Energy, 14 (2015), pp. 364–371.

[93] J. Wang, H. Wang, B. Zhang, Y. Wang, S. Lu, and X. Zhang, *A Stable Flexible Silicon Nanowire Array as Anode for High-Performance Lithium-ion Batteries*, Electrochimica Acta, 176 (2015), pp. 321–326.

[94] L. Wang, P. Liu, P. Guan, M. Yang, J. Sun, Y. Cheng, A. Hirata, Z. Zhang, E. Ma, M. Chen, and X. Han, *In situ atomic-scale observation of continuous and reversible lattice deformation beyond the elastic limit.*, Nature communications, 4 (2013), p. 2413.

[95] L. Wang, Y. Lu, J. Liu, M. Xu, J. Cheng, D. Zhang, and J. B. Goodenough, *A superior low-cost cathode for a Na-Ion battery*, Angewandte Chemie - International Edition, 52 (2013), pp. 1964–1967.

[96] L. Wang, Z. Xu, W. Wang, and X. Bai, *Atomic mechanism of dynamic electrochemical lithiation processes of MoS2 nanosheets*, Journal of the American Chemical Society, 136 (2014), pp. 6693–6697.

[97] W. Wang, Q. Zhao, K. Laurent, Y. Leprince-Wang, Z.-M. Liao, and D. Yu, *Nanorainforest solar cells based on multi-junction hierarchical p-Si/n-CdS/n-ZnO nanoheterostructures.*, Nanoscale, 4 (2012), pp. 261–8.

[98] X. Wang, X. Cao, L. Bourgeois, H. Guan, S. Chen, Y. Zhong, D. M. Tang, H. Li, T. Zhai, L. Li, Y. Bando, and D. Golberg, *N-doped graphene-SnO 2 sandwich paper for high-performance lithium-ion batteries*, Advanced Functional Materials, 22 (2012), pp. 2682–2690.

[99] X. Wang, B. Liu, R. Liu, Q. Wang, X. Hou, D. Chen, R. Wang, and G. Shen, *Fiber-based flexible all-solid-state asymmetric supercapacitors for integrated photodetecting system*, Angewandte Chemie - International Edition, 53 (2014), pp. 1849–1853.

[100] X. Wang, D.-M. Tang, H. Li, W. Yi, T. Zhai, Y. Bando, and D. Golberg, *Revealing the conversion mechanism of CuO nanowires during lithiation–delithiation by in situ transmission electron microscopy*, Chemical Communications, 48 (2012), p. 4812.

[101] X. Wang, W. Tian, D. Liu, C. Zhi, Y. Bando, and D. Golberg, *Unusual formation of ??-Fe2O3 hexagonal nanoplatelets in N-doped sandwiched graphene chamber for high-performance lithium-ions batteries*, Nano Energy, 2 (2013), pp. 257–267.

[102] X. Wang, Q. Weng, X. Liu, X. Wang, D. M. Tang, W. Tian, C. Zhang, W. Yi, D. Liu, Y. Bando, and D. Golberg, *Atomistic origins of high rate capability and capacity of N-doped graphene for lithium storage*, Nano Letters, 14 (2014), pp. 1164–1171.

[103] Y. X. Wang, S. L. Chou, H. K. Liu, and S. X. Dou, *Reduced graphene oxide with superior cycling stability and rate capability for sodium storage*, Carbon, 57 (2013), pp. 202–208.

[104] Z. L. Wang, *Piezopotential gated nanowire devices: Piezotronics and piezo-phototronics*, Nano Today, 5 (2010), pp. 540–552.

[105] Y. Wen, K. He, Y. Zhu, F. Han, Y. Xu, I. Matsuda, Y. Ishii, J. Cumings, and C. Wang, *Expanded graphite as superior anode for sodium-ion batteries.*, Nature communications, 5 (2014), p. 4033.

[106] R. Wu, X. Qian, K. Zhou, J. Wei, J. Lou, and P. M. Ajayan, *Porous spinel ZnxCo3- xO4 hollow polyhedra templated for high-rate lithium-ion batteries*, ACS Nano, 8 (2014), pp. 6297–6303.

[107] Y. Wu, J. Xiang, C. Yang, W. Lu, and C. M. Lieber, *Single-crystal metallic nanowires and metal/semiconductor nanowire heterostructures.*, Nature, 430 (2004), pp. 61–65.

[108] B. Xiang, D. J. Hwang, J. B. In, S. G. Ryu, J. H. Yoo, O. Dubon, A. M. Minor, and C. P. Grigoropoulos, *In Situ TEM near-field optical probing of nanoscale silicon crystallization*, Nano Letters, 12 (2012), pp. 2524–2529.

[109] X. Xing, Q. Zhang, Z. Huang, Z. Lu, J. Zhang, H. Li, H. Zeng, and T. Zhai, *Strain Driven Spectral Broadening of Pb Ion Exchanged CdS Nanowires*, Small, 12 (2016), pp. 874–881.

[110] J. Xu and G. Shen, *A flexible integrated photodetector system driven by on-chip microsupercapacitors*, Nano Energy, 13 (2015), pp. 131–139.

[111] Y. Xu, Y. Zhu, Y. Liu, and C. Wang, *Electrochemical performance of porous carbon/tin composite anodes for sodium-ion and lithium-ion batteries*, Advanced Energy Materials, 3 (2013), pp. 128–133.

[112] Z. Xu, C. Zhang, W. Wang, Y. Bando, X. Bai, and D. Golberg, *Lateral piezopotential-gated field-effect transistor of ZnO nanowires*, Nano Energy, 13 (2015), pp. 233–239.

[113] H. Xue, N. Pan, M. Li, Y. Wu, X. Wang, and J. G. Hou, *Probing the strain effect on near band edge emission of a curved ZnO nanowire via spatially resolved cathodoluminescence.*, Nanotechnology, 21 (2010), p. 215701.

[114] H. Yan, H. S. Choe, S. Nam, Y. Hu, S. Das, J. F. Klemic, J. C. Ellenbogen, and C. M. Lieber, *Programmable nanowire circuits for nanoprocessors.*, Nature, 470 (2011), pp. 240–244.

[115] Q. Yang, X. Guo, W. Wang, Y. Zhang, S. Xu, D. H. Lien, and Z. L. Wang, *Enhancing Sensitivity of a Single ZnO Micro-/Nanowire Photodetector by Piezo-phototronic Effect*, ACS Nano, 4 (2010), pp. 6285–6291.

[116] Q. Yang, W. Wang, S. Xu, and Z. L. Wang, *Enhancing light emission of ZnO microwire-based diodes by piezo-phototronic effect*, Nano Letters, 11 (2011), pp. 4012–4017.

[117] S. Yang, L. Wang, X. Tian, Z. Xu, W. Wang, X. Bai, and E. Wang, *The piezotronic effect of zinc oxide nanowires studied by in situ TEM*, Advanced Materials, 24 (2012), pp. 4676–4682.

[118] Z. Yang, J. Zhang, M. C. W. Kintner-Meyer, X. Lu, D. Choi, J. P. Lemmon, and J. Liu, *Electrochemical energy storage for green grid*, Chemical Reviews, 111 (2011), pp. 3577–3613.

[119] J. Yao, B. Liu, S. Ozden, J. Wu, S. Yang, M.-T. F. Rodrigues, K. Kalaga, P. Dong, P. Xiao, Y. Zhang, R. Vajtai, and P. M. Ajayan, *3D Nanostructured Molybdenum Diselenide/Graphene Foam as Anodes for Long-Cycle Life Lithium-ion Batteries*, Electrochimica Acta, 176 (2015), pp. 103–111.

[120] H. Yu, Y. Ren, D. Xiao, S. Guo, Y. Zhu, Y. Qian, L. Gu, and H. Zhou, *An ultrastable anode for long-life room-temperature sodium-ion batteries*, Angewandte Chemie - International Edition, 53 (2014), pp. 8963–8969.

[121] L. F. Zagonel, S. Mazzucco, Tence, K. March, R. Bernard, B. Laslier, G. Jacopin, M. Tchernycheva, L. Rigutti, F. H. Julien, R. Songmuang, and M. Kociak, *Nanometer scale spectral imaging of quantum emitters in nanowires and its correlation to their atomically resolved structure*, Nano Letters, 11 (2011), pp. 568–573.

[122] C. Zhang, N. Mahmood, H. Yin, F. Liu, and Y. Hou, *Synthesis of phosphorus-doped graphene and its multifunctional applications for oxygen reduction reaction and lithium ion batteries*, Advanced Materials, 25 (2013), pp. 4932–4937.

[123] C. Zhang, M. Neklyudova, L. Fang, Q. Xu, H. Wang, F. D. Tichelaar, and H. W. Zandbergen, *In situ electrical characterization of tapered InAs nanowires in a transmission electron microscope with ohmic contacts.*, Nanotechnology, 26 (2015), p. 155703.

[124] C. Zhang, W. Tian, Z. Xu, X. Wang, J. Liu, S.-L. Li, D.-M. Tang, D. Liu, M. Liao, Y. Bando, and D. Golberg, *Photosensing performance of branched CdS/ZnO heterostructures as revealed by in situ TEM and photodetector tests.*, Nanoscale, 6 (2014), pp. 8084–90.

[125] C. Zhang, Z. Xu, D. G. Kvashnin, D. M. Tang, Y. M. Xue, Y. Bando, P. B. Sorokin, and D. Golberg, *Opto-mechano-electrical tripling in ZnO nanowires probed by photocurrent spectroscopy in a high-resolution transmission electron microscope*, Applied Physics Letters, 107 (2015), p. 91103.

[126] W. Zhang, R. Zhu, V. Nguyen, and R. Yang, *Highly sensitive and flexible strain sensors based on vertical zinc oxide nanowire arrays*, Sensors and Actuators, A: Physical, 205 (2014), pp. 164–169.

[127] Y. Zhang, Y. Yang, and Z. L. Wang, *Piezo-phototronics effect on nano/microwire solar cells*, Energy & Environmental Science, 5 (2012), p. 6850.

[128] C. Zhu, X. Mu, P. A. Vanaken, Y. Yu, and J. Maier, *Single-layered ultrasmall nanoplates of MoS2 embedded in carbon nanofibers with excellent electrochemical performance for lithium and sodium storage*, Angewandte Chemie - International Edition, 53 (2014), pp. 2152–2156.

[129] Y. Zhu, M. Milas, M.-G. Han, J. Rameau, and M. Sfeir, *Multimodal Optical Nanoprobe for Advanced In-Situ Electron Microscopy*, Microscopy Today, 20 (2012), pp. 32–37.

Publications & Presentations

Journal articles

2016

1. Zhang C., Cretu O., Kvashnin D., Kawamoto N., Mitome N., Wang X., Bando Y., Sorokin P., Golberg D. "Statistically analyzed photoresponse of elastically bent CdS nanowires probed by light-compatible *in situ* High-Resolution TEM". *Nano Letters* 16(10), 6008-6013(2016);

2. Zhang C., Wang X., Liang Q., Liu X., Weng Q., Liu J., Yang Y., Dai Z., Ding K., Bando Y. Golberg D. "Amorphous phosphorus/nitrogen-doped graphene paper for ultrastable sodium-ion batteries". *Nano Letters* 16(3), 2054-2060(2016);

3. Xue Y., Dai P., Jiang X., Wang X., Zhang C., Tang D., Weng Q., Wang X., Pakdel A., Tang C. Bando Y., Golberg D. "Template-free synthesis of boron nitride foam-like porous monoliths and their high-end applications in water purification". *Journal of Material Chemistry A* 4(4), 1469-1478(2016);

4. Hou G., Cheng B., Cao Y., Yao M., Li B., Zhang C., Weng Q., Wang X., Bando Y., Golberg D., Yuan F. "Scalable production of 3D plum-pudding-like Si/C spheres: Towards practical application in Li-ion batteries". *Nano Energy* 24, 111-120(2016);

2015

5. Zhang C., Xu Z., Tian W., Wang X., Bando Y., Fukata N., Golberg D. "*In situ* fabrication and optoelectronic analysis of axial CdS/p-Si nanowire heterojunctions in a high-resolution transmission electron microscope".*Nanotechnology* 26, 154001-8(2015);

6. Xu Z., Zhang C., Bando Y., Bai X.D., Golberg D. "Lateral piezopotential-gated field-effect transistor of ZnO nanowires". *Nano Energy* 13, 233-239(2015);

7. Weng Q.H., Wang X., Zhang C., Jiang X., Bando Y., Golberg D. "Supercapacitive energy storage performance of molybdenum disulfide nanosheets wrapped with micoporous carbons". *Journal of Material Chemistry A* 3, 3097-3102(2015);

8. Wang. X, Liu D., Weng Q., Liu J., Liang X., Zhang C. "Cu/Li4Ti5O12 scaffold as superior anode for lithium-ion batteries". *NPG Asia Materials* 7, 171(2015);

9. Zhang C., Xu Z., Golberg D. " Opto-mechano-electrical tripling in ZnO nanowires probed by photocurrent spectroscopy in a high-resolution transmission electron microscope ". *Applied Physics Letters* 107, 091103(2015);

10. Xue Y., Jiang B., Bourgeois B., Dai P., Mitome M., Zhang C., Yamaguchi M., Matveev A., Tang C., Bando Y., Tsuchiya K., Golberg D. "Aluminum matrix composites reinforced with multi-walled boron nitride nanotubes fabricated by a high-pressure torsion technique". *Materials & Design* 88, 451-460(2015);

11. Weng Q., Ide Y., Wang X.B., Wang X., Zhang C., Jiang X., Xue Y., Dai P., Komaguchi K., Bando Y., Golberg D. "Design of BN porous sheets with richly exposed (002) plane edges and their application as TiO2 visible light sensitizer". *Nano Energy* 16, 19-27(2015);

12. Dai P., Xue Y., Wang X., Weng Q., Zhang C., Jiang X., Tang D., Wang X., Kawamoto N., Ide Y., Mitome M., Golberg D., Bando Y. "Pollutant capturing SERS substrate: porous boron nitride microfibers with uniform silver nanoparticle decoration". *Nanoscale* 7(45), 18992-18997(2015);

2014

13. Zhang C., Tian W., Xu Z., Liu J., Li S., Tang D.M., Cai X., Wang X.,Weng Q., Liao M., Kawamoto N., Bando Y., Golberg D. "Photosensing performance of branched CdS/ZnO heterostructures as revealed by in situ TEM and photodetector tests", *Nanoscale* 6, 8084-8090(2014);

14. Golberg D., Zhang C., Xu Z. "Cubic lattice nanosheets: Thickness-driven light emission", *ACS Nano* 8(7), 6516-6519(2014);

15. Tian W., Zhang C., Zhai T., Li S.L., Wang X., Liu J., Jie X., Liu D., Lioa M., Koide Y., Golberg D., Bando Y. "Flexible ultraviolet photodetectors with broad photoresponse based on branched ZnS-ZnO heterostructure nanofilms". *Advanced Materials* 26, 3088-3093(2014);

16. Wang X., Weng Q.H., Liu X., Wang X.B., Tang D.M., Tian W., Zhang C., Yi W., Liu D., Bando Y., Golberg D. "Atomistic origins of high rate capability and capacity of N-doped graphene for Lithium storage". *Nano Letters* 14, 1164-1171(2014);

17. Wang X., Chen Z., Liu D., Tian W., Wang Q., Zhang C., Liu J.W., Han L., Bando Y., Golberg D. "Tripled-yolked ZnO-CdS hollow spheres for semiconductor-sensitized solar cells", *Particle & Particle Systems Characterization* 31(7), 757-762(2014);

Previously

18. Tian W., Zhang C., Wang X., Golberg D., Bando Y. "Flexible SnO2 hollow nanosphere film based high-performance ultraviolet photodetector". *Chemical Communications* 49(36), 3739-3741(2013);

19. Tian W., Zhang C., Wang X., Golberg D., Bando Y. "Flexible ultraviolet photodetectors with broad photoresponse based on branched ZnS-ZnO heterostructure nanofilms". *Advanced Materials* 26(19), 3088–3093(2013);

20. Tian W. Wang X., Zhi C., Zhai T., Liu D., Zhang C., Golberg D., Bando Y. "Ni (OH)2 nanosheet@ Fe2O3 nanowire hybrid composite arrays for high-performance supercapacitor electrodes". *Nano Energy* 2(5), 754-763(2013).

21. Zhang C., Huang H., Liang B., Wang X.F., Lan X., Xiang Q., Liu B., Chen D. "Patterned growth of In2O3 spheres organized by radially-aligned In2O3 nanobelts". *Journal of Nanoengineering and Nanomanufacturing* 2(2), 166-170(2012);

22. Wang X.F., Huang H., Liu B., Liang B., Zhang C., Ji Q., Chen D., Shen G. "Shape evolution and

applications in water purification: the case of CVD-grown Zn2SiO4 straw-bundles". *Journal of Material Chemistry* 22(12), 5330-5335(2012).

Oral presentations

1. *Nanowire deformations and axial junction constructions in tandem with photocurrent measurements inside a transmission electron microscope*, MRS Spring 2016, Phoenix, USA(2016);

2. *Optoelectronic properties of nanostructured materials as revealed by laser-compatible in situ Transmission Electron Microscopy*, 23rd Australian Conference on Microscopy and Microanalysis, Adelaide, Australia(2014).

Poster presentations

1. *Amorphous P@Graphene paper for ultrastable sodium-ion batteries*, AsiaNano 2016, Sapporo, Japan(2016);

2. *In situ fabrication and photocurrent analysis of axial CdS/p-Si nanowire junctions by high-resolution TEM*, Japanese Society of Microscopy Kanto-branch meeting, Tokyo, Japan(2015).

Colophon

Should you have any questions, please feel free to contact me by e-mail
zhang.chao@nims.go.jp (until March 2017)
zcelysium@gmail.com (after March 2017)

This is the end of the dissertation.

Last updated: February 15, 2017 • My Google scholar • Codes on Github